A study of negatively charged hadrons in Pb-Pb collisions in the NA57 experiment at the CERN SPS

Paul Bacon

Thesis

Heavy Ion Physics Group,
School of Physics and Astronomy,
University of Birmingham.

November 8, 2005

To Mum and Dad

A Quote for each of the three main things I have spent my time doing during my PhD:

"Programming today is a race between software engineers striving to build bigger and better idiot-proof programs, and the Universe trying to produce bigger and better idiots. So far, the Universe is winning."

Rich Cook.

"Some people think football is a matter of life and death. I assure you, it's much more serious than that."

Bill Shankly.

"You're not drunk if you can lie on the floor without holding on."

Joe E Lewis.

Abstract

Using data taken by the NA57 Collaboration at the CERN SPS, for Pb-Pb collisions at both 158 GeV/c and 40 GeV/c energies, results have been obtained for yields per unit of rapidity and inverse slope measurements. A thorough investigation has been performed on the stability of the acceptance region used in the analysis of both beam energies and a detailed explanation of the analysis methods used is given. Furthermore a study has been completed to determine R_{CP} in the three data sets which were considered. These results can be used in future analysis by the NA57 collaboration as part of a signature of the Quark Gluon Plasma (QGP).

An Overview of QGP physics as well as several signatures which can be used to detect the formation of a QGP state are given. The results found in this analysis are compared to those found by the STAR collaboration and to theoretical models for R_{CP}.

Author's Contribution

The work presented in this thesis is based on data taken by the NA57 collaboration over a period of 3 years (1998-2000). It has primarily involved the analysis of negatively charged particles in order to calculate yields which can be used to determine enhancements. Furthermore, I have continued the analysis to determine R_{CP} in all 3 data sets and have provided a high statistics R_{CP} result which has now been published by the collaboration.

Throughout the analysis I have made use of well established software which has been produced both within the collaboration and from the physics world in general. I have adapted the software specifically to analyse the 3 data sets I have worked on and to look at the negatively charged particles in question.

Acknowledgements

I would like to thank Dr. Roman Lietava for his continuing support and help throughout my PhD as well as his input into my work. I would also like to thank Dr. David Evans for his help with my work and for making my trips to CERN as entertaining as possible with his guided tours through the underground tunnels and his rather dangerous but fun trips skiing. I would also like to thank the rest of the NA57 collaboration for allowing me to work on the experiment and especially the Birmingham group.

The former and current students at Birmingham have also been a great help to me, namely Dr. Paul Bell, Dr. Rory Clarke, Dr. Stephen Bull, Mr Richard Platt and Mr Daniel Tapia Takaki for sharing an office with me and putting up with my large collection of F.H.M. that sits in our office, Ms Tamsin Moye, Mr Matthew Barrett, Mr Matthew Gardner and Mr Alistair Hart who spent hours and hours playing pool with me in staff house and accompanying me on so many drinking nights I can not remember. I would also like to thank them for keeping me sane for my entire time at the university, for the Playstation they got me in my first year, which is still keeping me entertained to this day, and keeping my pint forever full whenever my wallet was not in a similar state. I would also like to thank the members of the Astro football team for letting me play despite not being an astro-physicist and especially to Dr Ian M Robinson for being a good friend through out my time in Birmingham.

From outside the university I would like to thank my family, namely my mum and dad for all their support both financially and for keeping my room at home so I could regularly bring back my washing for them to do. I would like to thank my brother, Gary Bacon, for keeping me entertained when I was away from university. I would also like to thank Ms Victoria Mills, my girlfriend, for all the help she has given me throughout my time in Birmingham. Including helping me with marking, presentations and for all the meals she cooked for me, without which I would almost certainly have bankrupted myself through take-away dinners. I would also like to thank her and her family for the wonderful summer I spent with them down in Devon where I was taught to ride a horse, and thanks to Sally, the horse, for not throwing me off. I would also like to thank my friends, Mr David Oates, Mr Matthew Foley, Ms Julie Carr and many many others who have been great friends whenever I have seen them.

I would also like to thank some of my old school teachers who inspired me to continue on through education and find out just how far I could go. From Jacksdale Primary school Mrs MacManus and Mr Hutchinson, from Matthew Holland Secondary School Mr Underwood and Mr Barker and from High Pavement Sixth form college Mr Armstrong and Mr Milbourn were all superb teachers. I would also like to thank the Physics Department from Nottingham Trent University for all their help in my degree and to Dr. Bill Neil for his help with my dissertation.

Contents

List of Figures

List of Tables

Chapter 1

The Quark Gluon Plasma

1.1 Introduction

One of the most fundamental questions that man has been able to ask is, "what makes up the basic building blocks of matter and what laws of nature control the matter that makes up the universe we live in?" Over time man has come to understand that the matter we see in everyday life is made up of atoms, which in turn are made up of a dense positively charged nucleus and negatively charged electrons orbiting around this nucleus. Further experimentation revealed a substructure to this nucleus, showing it to be made up of protons and neutrons. These three particles were, for a while, thought to be the basic building blocks of matter. However, beginning in the 1950s scientists have found that below this structure lies another substructure. Whilst electrons are still considered basic particles that have no substructure, they have been placed in a group with other similar particles called leptons. The protons and neutrons have been shown, indirectly by many high-energy experiments, to be made up of point-like [1] objects called quarks. These quarks are currently thought to have no substructure and so are fundamental particles.

[1] The current limit placed on the size of quarks is $< 10^{-19}$ m

Over time the model of this new structure of matter has evolved into what we now call the Standard Model. This basically consists of 6 quarks and 6 leptons (and their anti-particles) as the building blocks of matter and 5 gauge bosons, which are the particles that carry 3 of the fundamental forces, the electromagnetic force, the weak force and the strong nuclear force. The fourth force, gravity, is still not covered by the standard model. Properties of the quarks, leptons and gauge bosons are shown in Tables 1.1 and 1.2 below.

Table 1.1: Table of Leptons and Quarks with some of their Properties

Leptons, spin=$\frac{1}{2}$			Quarks, spin=$\frac{1}{2}$		
Flavour	Mass GeV/c^2	Electric Charge	Flavour	Mass GeV/c^2	Electric Charge
ν_e Electron Neutrino	<1 x 10^{-6}	0	**u** up	0.003	$\frac{2}{3}$
e Electron	0.000511	-1	**d** down	0.006	$-\frac{1}{3}$
ν_μ Muon Neutrino	<0.0002	0	**c** charm	1.3	$\frac{2}{3}$
μ Muon	0.106	-1	**s** strange	0.1	$-\frac{1}{3}$
ν_τ Tau Neutrino	<0.02	0	**t** top	175	$\frac{2}{3}$
τ Tau	1.7771	-1	**b** bottom	4.3	$-\frac{1}{3}$

The quarks are confined, and form baryons, which are states of 3 quarks or anti-quarks, or mesons, which are quark anti-quark pairs. The force which confines the quarks in these states is called the strong nuclear force (or colour force) and is governed by the theory of Quantum Chromo Dynamics (QCD) [1]. It consists of 3 colour charges: red, green and blue and their anti-charges. The mechanism by which it works is analogous to the electromagnetic force, Quantum Electro Dynamics (QED) [2], which governs how particles interact, due to their electromagnetic charge, but with some differences. The first difference is that the gluon (which carries the

Table 1.2: Table of Gauge Bosons and some of their properties

Gauge Bosons			
Flavour	Approx. Mass GeV/c^2	Electric Charge	Interaction
Photon, γ	0	0	Electromagnetic
W^+	80.4	+1	Weak
W^-	80.4	-1	
Z^0	91.187	0	
Gluon, g	0	0	Strong

strong force) actually has colour itself, unlike the photon which does not carry any electric charge. This leads to the second and more significant difference: since the photon does not carry any charge, any virtual photon emitted by the charge will not make any difference to the charge itself; however, any virtual electron positron pair it becomes will mask the initial charge. The effect of these differences is shown in Figures 1.1 and 1.2. Figure 1.1 shows how virtual photons are emitted by an electron and how they can become e^+e^- pairs. These virtual e^+e^- pairs and the virtual photons form a "*cloud*" around the inital electron and so mask its charge from any test charge around it. This effect is called screening. Overall this means that the further away from the inital charge you get, the less a test charge can feel the initial charge of the electron. This is shown in the plot at the bottom of Figure 1.1. Figure 1.2 shows the same thing but for a colour charge. The virtual gluons it emits can become virtual q $\overline{q}$ pairs or gluon gluon pairs. This leads to the "*cloud*" surrounding the initial charge adding even more colour charge, therefore if a test charge was to be taken further away from the initial charge it would see a stronger and stronger charge. This is what leads to quark confinement in particles. The plot at the bottom of Figure 1.2 shows how a test charge would see the charge of a bare quark as it was moved further and further away from the initial charge. This effect is called anti-screening.

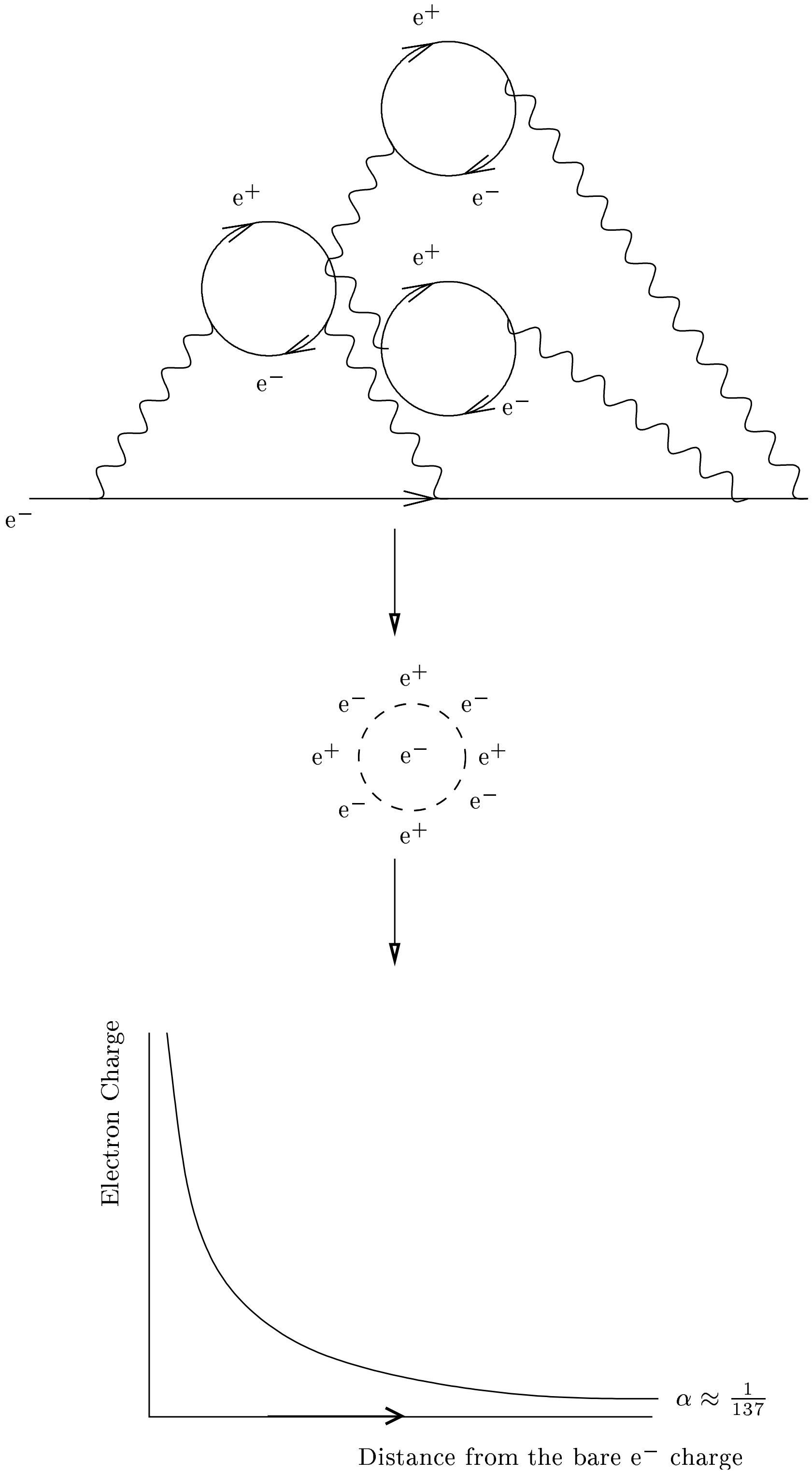

Figure 1.1: Screening of electric charge in quantum field theory

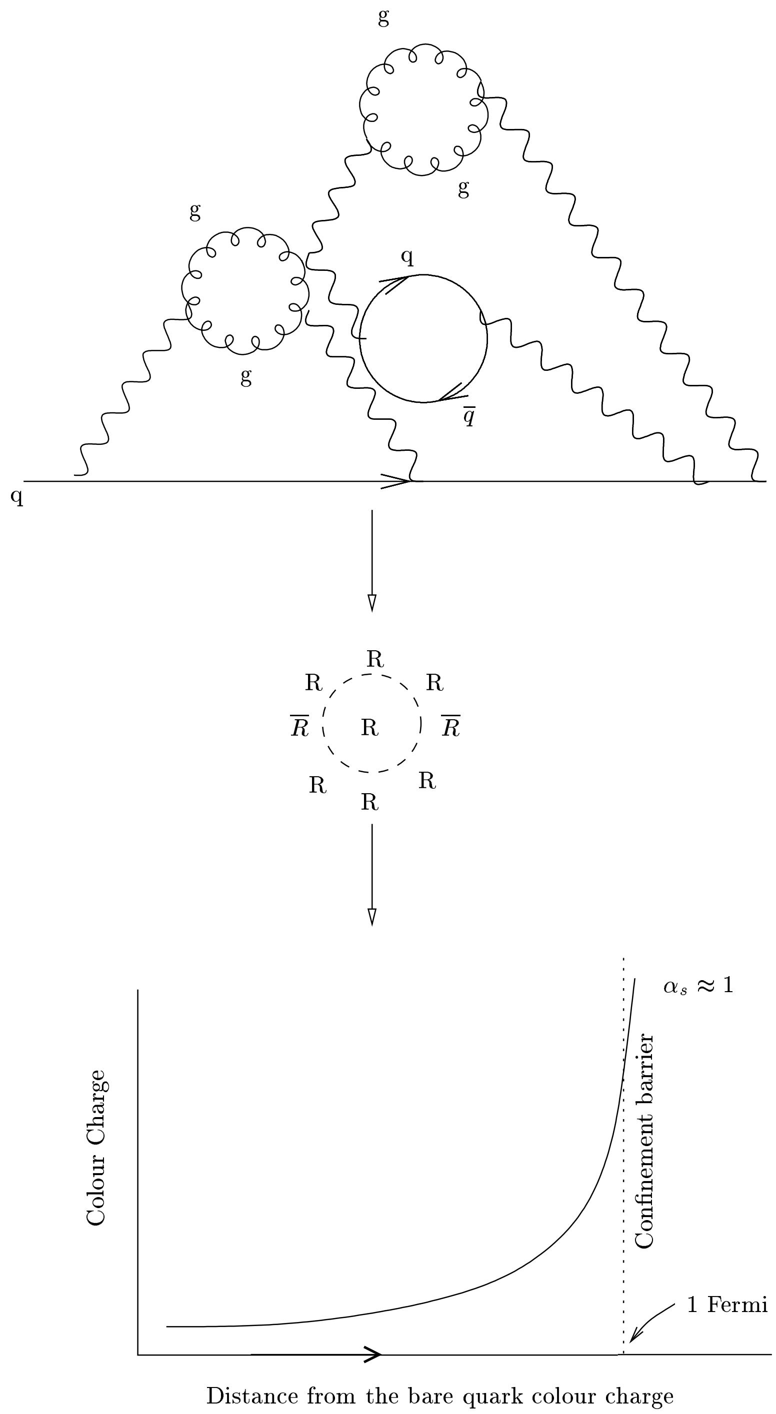

Figure 1.2: Screening of colour charge in quantum field theory

If two quarks were separated from each other to a point where the potential energy between them is enough to create a quark anti-quark pair, then this will generally happen and this results in two or more mesons that will move away from the initial quark position as jets. This is shown in Figure 1.3. Experimentally, no evidence of a free quark has ever been found and it is thought that all baryons and mesons are colour neutral.

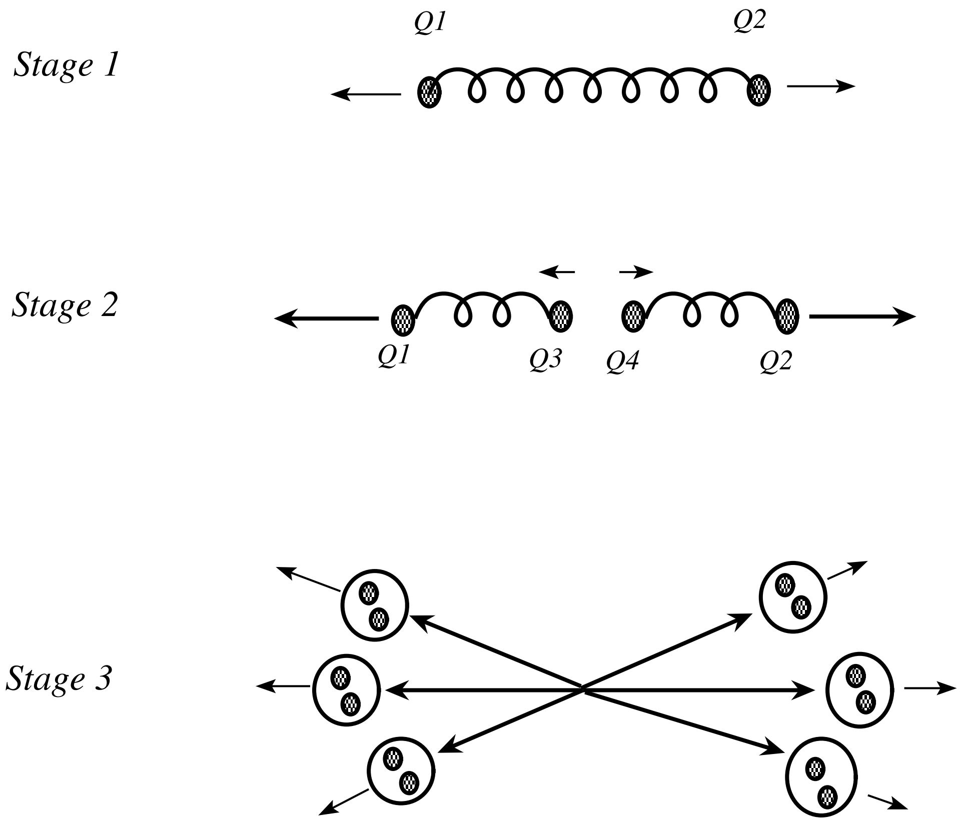

Figure 1.3: Jet production from a quark anti-quark pair

In Figure 1.3 stage 1, Q1 and Q2 are a quark anti-quark pair that are moving apart. Once the distance between them is large enough for the potential energy to create another quark anti-quark pair, Q3 and Q4 are created, this is stage 2. Q1 and Q3 (a quark and anti-quark) continue to move off in the same direction but with different momenta. This again causes a build up in potential energy and so the bond between them breaks. The same process happens between Q2 and Q4. In stage 3 this continues to happen until the potential energy between the two quarks is small enough for them to create a meson. The created mesons move away from the initial quark anti-quark pair's position as two jets of mesons moving in opposite directions so as to conserve momentum. The process is not confined to creating jets of mesons; the created jets can also contain baryons. However, the diagram only shows mesons for simplicity.

1.2 Asymptotic Freedom

Asymptotic freedom is a description of how quarks behave as the coupling constant α_s approaches 0. The anti-screening effect, described previously, is due to the gluon carrying colour charge itself. This fact means that α_s is described by the following formula as a function of Q^2 [3] as shown in Figure 1.2.

$$\alpha_s(Q^2) = \frac{12\pi}{(33-2n_f)log\frac{Q^2}{\Lambda^2}}.$$

The number of quark flavours is represented by n_f and Λ^2 is a scale parameter for renormalisation. Λ is found experimentally to be approximately 200 MeV. By considering high Q^2 values which can represent small distances between the initial charge and test charge it can be seen that α_s approaches zero when the two quarks are brought close together. It also shows that the maximum separation of two quarks is of order 1 fm as shown in Figure 1.2. When α_s approaches zero the quarks act as independent particles.

The mass of a quark is made up of two parts. The first is its current mass which it will always have. This is sometimes called the bare mass and is the mass that the quark would have if it was not bound in a particle. The second is the dynamic mass, sometimes called the constituent mass. This is the mass of the quark due to the gluons that are bound to it [4]. During quark gluon plasma formation (described in section 1.3) the quarks become packed together in a very dense region. This in turn means that α_s reduces as described above and the contribution of the constituent mass of the quark drops off leaving only the bare mass. For u and d quarks this is a drop to approximately 3 MeV or 7 MeV respectively from about 350 Mev [5]. This significant drop means that the quarks in a plasma act as almost massless particles when compared to confined quarks.

The bare mass of the strange quark(s), however, is not as close to zero as it is for the up and down quarks. The effect is however still significant, as the mass of a strange quark drops from 550 MeV to 150 MeV[6]. This means that it is easier to create s $\bar{s}$ pairs. This is one of the reasons that there should be an enhancement in the number of strange particles produced within a QGP.

1.3 Quark Gluon Plasma Formation

As the temperature and/or pressure of nuclear matter is increased, phase changes within the matter will occur. The phase changes involved in moving from a gas to a liquid and then to a solid are well understood as is the next phase transition to an ionic plasma. With further increases in pressure and/or temperature all of the electrons can be stripped from the nucleus and therefore a sea of electrons and nuclei are left. If this is taken to an even further extreme and the energies are again increased it is possible to break the bonds that hold the nucleus together. This would leave a gas of nucleons (protons and neutrons) and electrons all behaving as free particles. The next stage is to increase the energy to break these down. At this point the quarks become effectively free particles, as do the gluons that hold them together in the nucleus, and a sea of quarks and gluons acting effectively independently of each other is produced [7]. This phase transistion is shown in Figure 1.4. It is however, extremely difficult to achieve this state of matter due to the conditions that are required, although it is thought that when a neutron star is formed the centre of the star can reach this phase. As you move through the phase transitions described above, the density of the material decreases with every change. This is because the constituents of the material become more energetic and spread out. However in the QGP state the density increases significantly. This is because the strong nuclear force is now being broken down and so the particles can be packed together tightly to continue to overcome this force.

Figure 1.4 shows the phase diagram for a Quark Gluon Plasma. The Baryo-chemical potential is basically a measure of the net baryon number. Therefore as atomic matter is made up of only baryons (3 quarks and no anti quarks) it has a baryo-chemical potential of 1.

1.4 Experiments

The only current way to create a QGP in the laboratory is to use particle accelerators to take heavy nuclei to high energies and then collide them. This is because a large energy density is required to create the extreme conditions involved. The Super Proton Synchrotron (SPS) at CERN can accelerate lead ions to a point where they will reach a momentum of 158 GeV/c per nucleon and collide with a fixed target. This means they will be travelling at 99.998% of the speed of light. The conditions of the system produced in the resulting collision resemble the state of the universe around 10^{-5} to 10^{-6} seconds after the Big Bang. This interaction of the colliding lead ions could allow enough of the initial energy of the system to be converted into thermal energy and so could interact long enough to allow the system to reach equilibrium where the temperature would be around 250 MeV. Under these conditions it is predicted that matter undergoes a phase transition to an exotic new

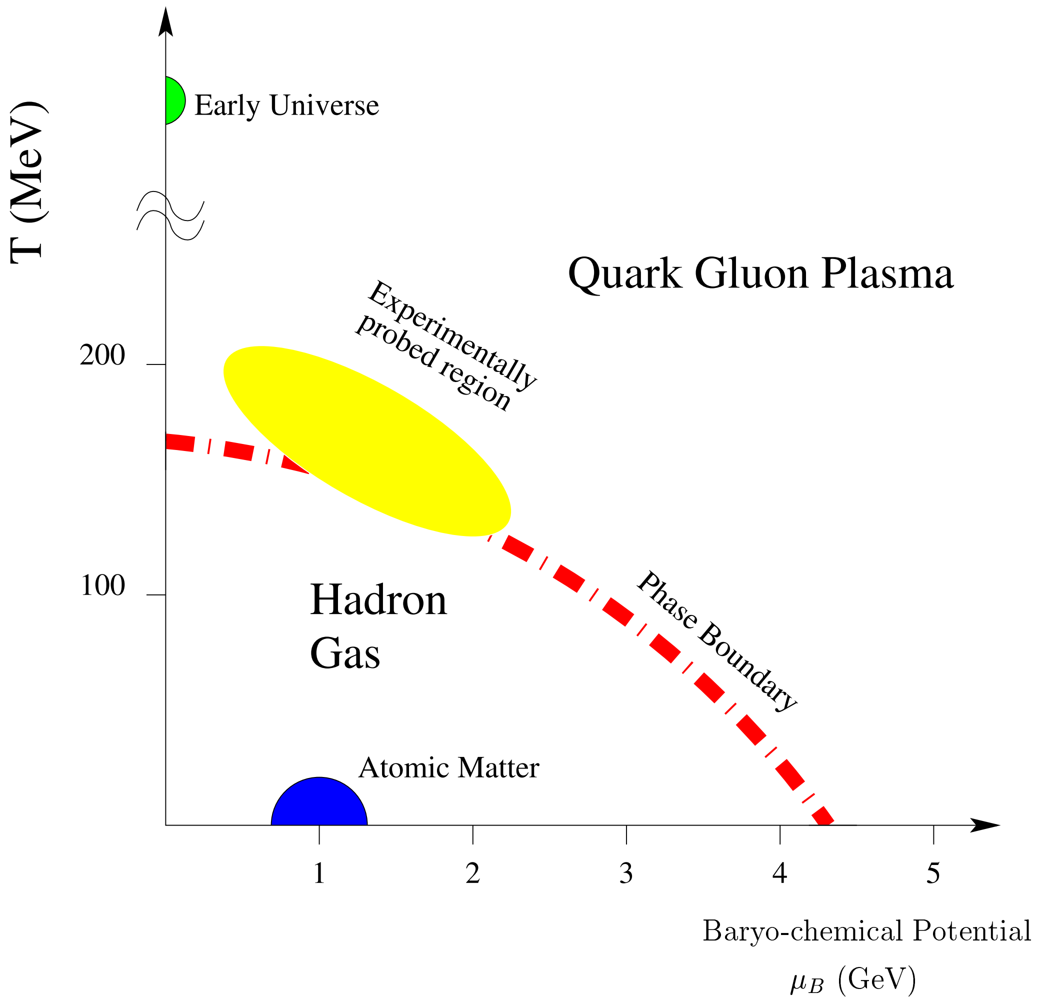

Figure 1.4: Phase diagram showing the transition from a hadronic gas to a Quark gluon plasma as a function of temperature and baryo-chemical potential

state of matter, where quarks and gluons are effectively free and no longer confined to colour neutral combinations, this is known as the Quark Gluon Plasma (QGP)[8].

1.5 Signatures

After the collision of the heavy ions a system of partons is created. These will reach thermal equilibrium, and create a Quark Gluon Plasma state. This is expected to take approximately 10^{-23} seconds for 158 GeV/c collisions as the fireball is roughly 3 fermi in diameter. The QGP will then expand and cool before forming hadrons. This hadron gas will further expand until all interactions stop. These hadrons will then fly off in all directions and be detected in any detectors present, allowing the various signatures of the QGP formation to be observed. In the rest of this section the main signatures of the QGP which have been considered experimentally are described.

1.5.1 Strangeness Enhancement

The WA97 experiment, which was based at CERN, found an enhancement of strange particles in Pb-Pb collisions, where formation of a QGP is expected, compared to p-Be collisions, where no QGP formation is expected. An enhancement is defined using the formula:

$$Enhancement = \frac{\frac{Yield_{interaction}}{N_{Wint}}}{\frac{Yield_{p-Be}}{N_{Wp-Be}}} \tag{1.1}$$

In the above equation N_W is the number of wounded nucleons in either the interaction (N_{Wint}) or the reference data (N_{Wp-Be}). The reference data used by the WA97 experiment was from proton - Beryllium collisons. The number of wounded nucleons is a measure of the number of nucleons which take part in the collision and is estimated from the multiplicity of the collision. Multiplicity is discussed further in chapter 2. The yield is the number of particles created by the interaction per unit of rapidity. Therefore, the enhancement is the yield per wounded nucleon in the Pb-Pb interaction normalised with the yield per wounded nucleon in the p-Be interaction. The data used for the normalisation were taken using a proton beam on a beryllium target.

The enhancement itself is caused because of the reduction in mass of the strange quark to its bare mass, thus making it easier to create $s\bar{s}$ pairs within the plasma as the temperature of the fireball is approximately 200-250 MeV. Therefore the thermal energy of the gluons will be 200-250 MeV allowing the process of gg $\longrightarrow$ s$\overline{\text{s}}$ to take place. This is one of two reasons that the number of strange particles and anti-particles within the plasma will rise when compared to normal matter. The other reason is simply Pauli blocking. The original matter involved in the collision contains only up and down quarks. This means that there will be an excess of them in the QGP and so some of the available up and down states are already filled. This will disfavour further u$\overline{\text{u}}$ and d$\overline{\text{d}}$ production, to some extent, and hence favour s$\overline{\text{s}}$ production.

The enhancement is seen by looking for the production of strange hadrons that come from the collision. These are the Λ, $\overline{\Lambda}$, Ξ^-, $\overline{\Xi}^+$, Ω^- and $\overline{\Omega}^+$ baryons and the K_s^0 short meson. These are not detected directly but rather from their weak decays, some of these decays are listed below.

- $\mathrm{K_s^0} = \frac{1}{\sqrt{2}}((\overline{\mathrm{d}})\mathrm{s} + \mathrm{d}(\overline{\mathrm{s}})) \longrightarrow \pi^+ + \pi^-$,
- $\Lambda = (\mathrm{uds}) \longrightarrow \mathrm{p} + \pi^-$,
- $\overline{\Lambda} \longrightarrow \overline{\mathrm{p}} + \pi^+$,
- $\Xi^- = (\mathrm{dss}) \longrightarrow \Lambda + \pi^-$,
- $\Omega^- = (\mathrm{sss}) \longrightarrow \Lambda + \mathrm{K}^-(\overline{\mathrm{u}}s)$.

Enhancements of these particles have been observed by the WA97 collaboration[9] and are shown in Figure 1.5 [10] below where $<\mathrm{N}_{part}>$ is the same as number of wounded nucleons.

The NA57 collaboration[11], has also found enhancements in strange particles as shown in Figure 1.6.

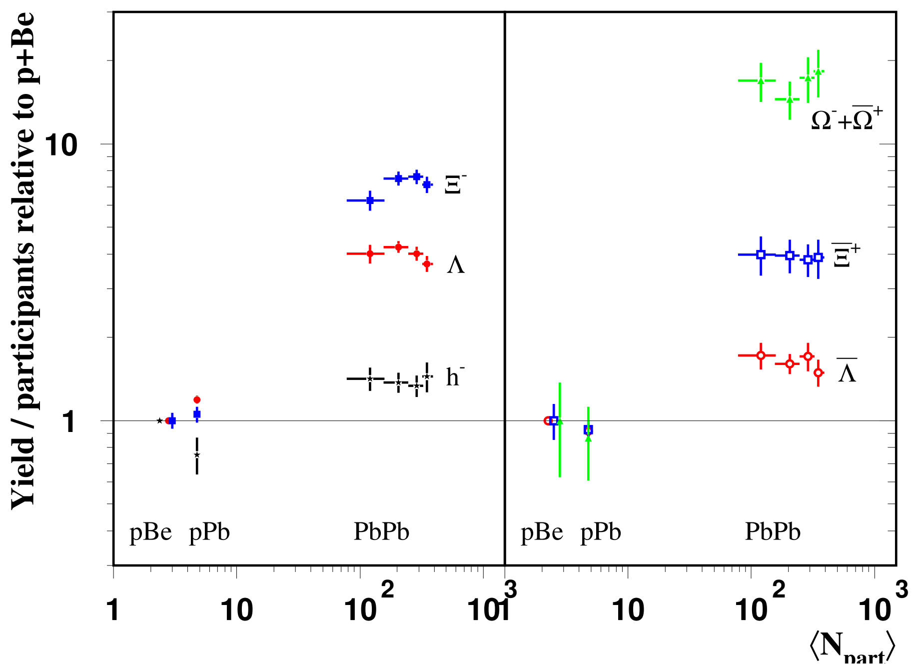

Figure 1.5: Mid-rapidity particle yields per wounded nucleon normalised to p-Be yield in Pb-Pb collisions at 158 GeV/nucleon. (WA97 collaboration)

Figures 1.5 and 1.6 show enhancements with respect to proton beryllium (p-Be) collisions for various species of strange particles. The y-axis shows the yield normalised to that found in the p-Be collisions. The x-axis shows the average number of particles involved in the collisions ($<N_{Wound}>$), for the lead-lead (Pb-Pb) collisions there are several points which represent how central the collision was. The definition of centrality is discussed in the next chapter. The figure itself shows the points for p-Be collisions sitting at 1, this is because they are normalised to themselves, the proton-lead (p-Pb) collision points are also at values close to 1, which shows that these two collisions produce similar states where no QGP is formed. The various Pb-Pb collisions points however, correspond to larger values and so show an enhancement for the strange particles considered. The size of the enhancement is different for the different particle species but it is evident that the higher the strangeness content of the particle the larger the enhancement. An enhancement of negative particles is also measured but is found to be smaller than that of strange

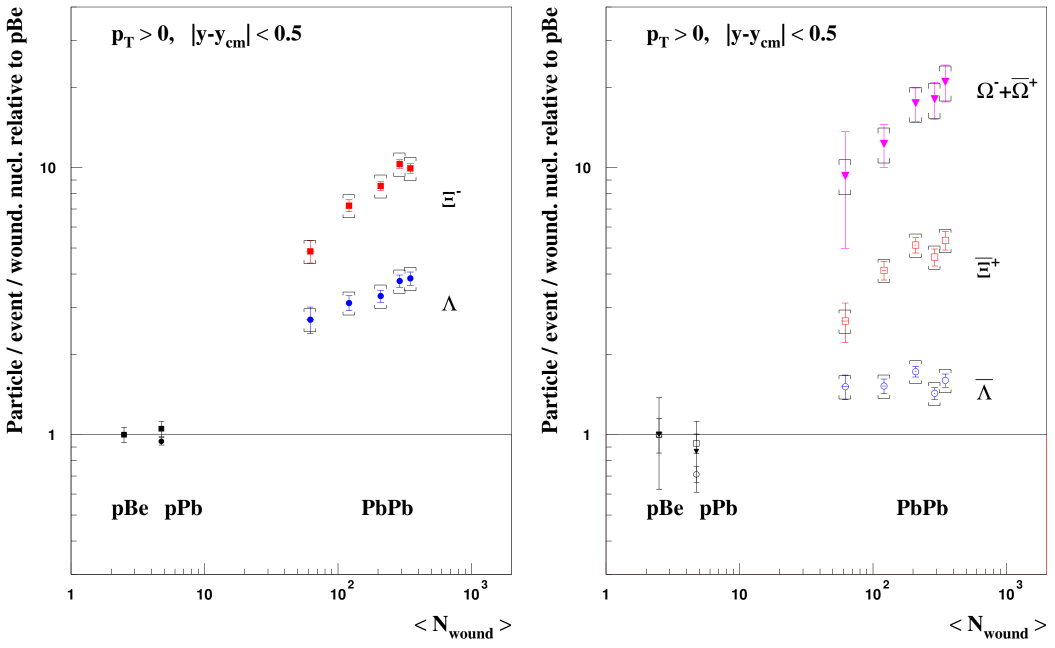

Figure 1.6: Mid-rapidity particle yields per wounded nucleon normalised to p-Be yield in Pb-Pb collisions at 40 GeV/nucleon. (NA97 collaboration)

particles. This enhancement is caused mainly by an increase in entropy of the system which is carried by the production of pions and the contamination of K^- mesons. The measurement of negative particles is important as it provides a baseline for the strangeness enhancement measurement.

The phase transition to the QGP from a hadronic gas can also be investigated at lower energies. By accelerating the incoming lead beam to a momentum of 40 GeV/c per nucleon they would be travelling at 99.97 % the speed of light. At this energy it has been predicted that the resultant fireball would reach an equilibrium temperature of 160 MeV [7]. Collisions at 40 GeV/c are expected to create the conditions closer to the phase transition boundary. The NA57 experiment, which is the successor to the WA97 experiment, is looking at data taken at 40 GeV/c in an attempt to look at the region close to the phase boundary. The NA57 experiment is also working with data taken at 158 GeV/c but looking at a larger collision centrality region. Centrality is defined in section 2.3.1

1.5.2 Direct Photon Production

When considering signals of QGP formation, photons arise as a possible candidate. This is because the photons themselves are not subject to the strong force and so any formed in the QGP will survive the hadronisation process to reach the detector, therefore giving a possible signal of the formation and information on the early stages of the collision. They are primarily formed, in the QGP, by the processes:

$$\mathrm{q}\overline{\mathrm{q}} \longrightarrow g\gamma$$

$$g\mathrm{q} \longrightarrow \gamma\mathrm{q}$$

However, this method of QGP detection is hampered by the background that swamps the signal. Due to the high energy density of the collision there are a very large number of particles created such as π^0 and η mesons which undergo the electromagnetic decays [7]

$$\pi^0 \longrightarrow \gamma\gamma$$

$$\eta \longrightarrow \gamma\gamma$$

At all the energies, currently being probed, this background has swamped any signal of direct photons coming from the QGP. However, in the range of $1 \leq P_T \leq 3$ GeV/c [12] the signal-to-background ratio is at its best and so in any future experiments, which create large temperatures the signal could become strong enough to be detected and, therefore, used as a signal for, and study of, QGP formation.

1.5.3 Dilepton Pairs

Like direct photons, leptons do not undergo strong interactions and so are another potentially good source for QGP signatures. Looking for single leptons in all the particles is practically impossible as there is a large background of these. However pairs of leptons are produced by the decays of various hadrons, with those with an invariant mass of less than 1 GeV being the main interesting source. Although there are three dominant decays it is the ρ meson which is of most interest as its lifetime is less than that of the QGP. This gives a signal of QGP formation because whilst in the QGP the ρ will have a reduced mass due to the asymptotic freedom discussed in section 1.2. Therefore, by decaying in the QGP its reconstructed mass will also be lower. This means that one would expect to see an enhancement in the reconstructed mass of the dileptons in the region corresponding to a reduced mass ρ.

The CERES experiment[13] found an enhancement in the masses of e^+e^- pairs when looking at Pb-Au collisions which are expected to form a QGP state. The reference data, when QGP formation was not expected to be formed, was taken using p-Be and p-Au collisions and the yields found for this data followed the expected trends of all the hadronic decays. The enhancement was found in the mass range of approximately $0.3 < M_{e^+e^-} < 0.7$ GeV and was measured as a factor of 2.6 as shown in Figure 1.7[14].

1.5.4 J/Ψ Suppression

Another signal of a QGP formation is the suppression of J/Ψ. J/Ψ mesons are formed in the initial collision. The J/Ψ travels through the QGP where it is no longer bound together. This is because the size of the J/Ψ bound state is approximately 0.5 fermi which is larger than the calculated colour screening radius within the QGP. The $c\bar{c}$ quarks that make up the J/Ψ state drift apart due to momentum and due to the expansion of the fireball. As the fireball hadronises they bond with other quarks and form D-mesons. If a QGP was not formed then the J/Ψ states would remain bound. At SPS energies, no further charm quarks are created within the QGP fireball because the temperature is approximately 200 MeV/c which is

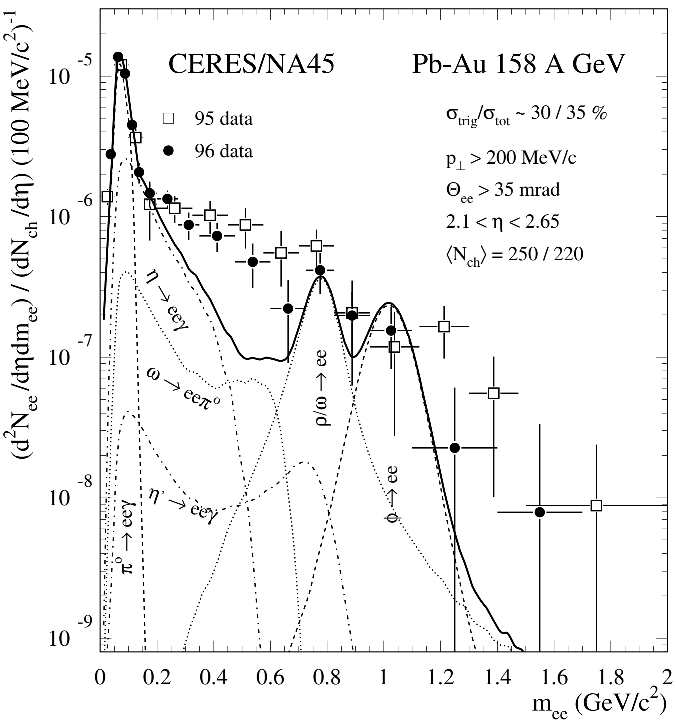

Figure 1.7: Mass spectra of e^+e^- pairs found at the CERES experiment. Expected trend for hadron gas shown as solid black line. Data points of Pb-Au collisions show clear enhancment between 0.3 and 0.7 GeV giving evidence of QGP formation

significantly less than the mass of the charm quark. Therefore a suppression of the J/Ψ bound states should be observed as a signature of QGP formation at SPS experiments. At other experiments such as those at RHIC[15] and the upcoming LHC[16] experiment, ALICE[17] the temperature of the fireball is higher. In collisions at these experiments the J/Ψ state is expected to be suppressed (in non central collisions), which still form a QGP, but in the most central collisions charm quarks are created within the fireball as well as in the initial collision; the result is that the suppression will not be as marked and may even become an enhancement [18][19]. A definition of central collisions is given in the next chapter.

This suppression has been observed by the NA50 collaboration [20] and was found to be approximately a factor 2 suppression. These results, which are shown in Figure 1.8[21], agree with the predictions made for the QGP. In Figure 1.8 the results are normalised to the expected yield which takes into account the absorption of the J/Ψ which is expected to take place due to hadron gas (*i.e.* $J/\Psi + \pi \longrightarrow D\,\overline{D}\,X$) [22]. However, this absorption is still being looked into by the NA50 collaboration.

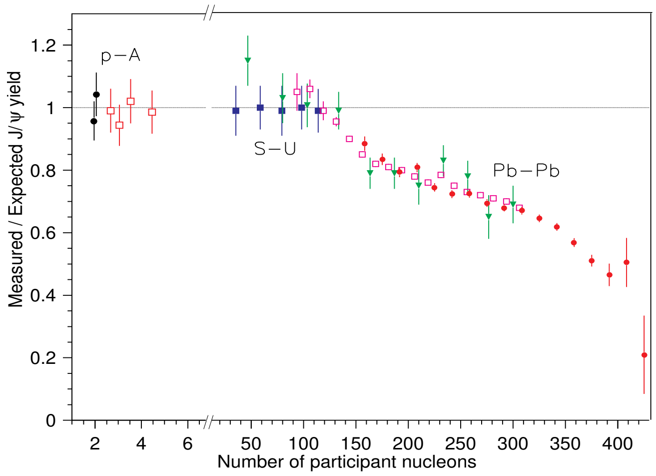

Figure 1.8: J/Ψ supression found at the NA50 experiment in Pb-Pb collisions at 158GeV/c. The black line shows the normalised position as determined by reference data taken using P-A collisions

1.5.5 Jet Quenching

Jet production is the mechanism in which a quark antiquark pair moving away from each other with a high potential energy, convert this energy into other bound hadron states to create colour singlet particles. The process is described in section 1.1 and results in two, back-to-back, jets of particles with high transverse momentum. If one of these jets were to pass through a dense medium it would be absorbed by the medium. This is because it would lose momentum as it transversed the medium by mechanisms such as bremsstrahlung. Therefore the suppression of jet production can be used as a signature of QGP formation.

If a quark on the edge of the fireball separates from an antiquark the potential energy between them will cause jet production, the first quark's jet will move away from the QGP region and will be observed in any detector it reaches. However, the second jet must transverse the highly dense QGP fireball before it can reach the detector and in travelling through the QGP fireball it can lose enough energy to be totally absorbed and so not emerge from the other side. This is shown diagramatically in Figure 1.9.

The RHIC experiment at Brookhaven has high enough beam energies and suitable detectors to measure these jet quenching effects. In p-p collisions and d-Au collisions, where a QGP state is not formed, jet production readily occurs. Results showed that jets were observed back to back in the detector, i.e. with a separation of 180°, for both sets of collisions where a QGP state is not formed. However, in central Au-Au collisions where a QGP is formed only one jet was seen in the detector, there was no jet observed at $\Delta\phi = \pi$ radians from the first jet. This shows QGP formation has occured and the dense matter of the QGP has absorbed the second jet. The results are shown in Figure 1.10[23], the top plot (a) shows the d-Au data and the solid line in plot b shows the p-p collsions. The data were taken by triggering on a detected jet and then looking for a second jet. The Au-Au data was also taken in the same way and so shows results where at least 1 jet was detected. It is possible that both jets are absorbed by the QGP; however it is not possible to trigger on these events as there is nothing to be detected.

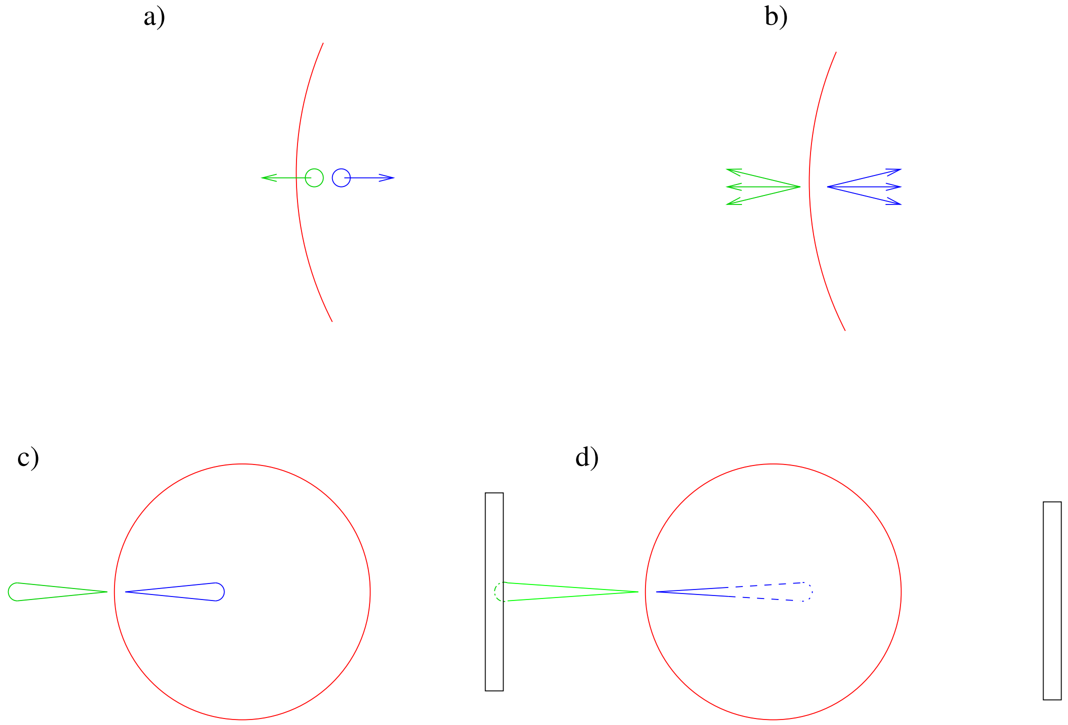

Figure 1.9: a) A quark pair on the edge of the fireball begins to separate and the potential energy between them increases. b) the potential energy between the quark pair results in jet formation and the two jets move away from each other back to back. c) one jet moves away from the fireball towards the detector, the other transverses the fireball losing energy as it does. d) the first jet reaches the detector and is observed. However, the second jet is absorbed by the fireball and so never reaches the detector and is therefore not observed.

1.5.6 High P_T suppression, R_{AB}

High P_T particles that transverse the dense fireball of the QGP state are expected to lose energy in a similar way to jets as described in section 1.4.5. Therefore a suppression of these high P_T tracks is expected when a QGP is formed. This can be seen by looking at the P_T spectra from interactions where QGP formation is expected, normalised to the P_T spectra of a non QGP formation collision and the number of collisions in each event. A formal definition for this ratio of P_T spectra

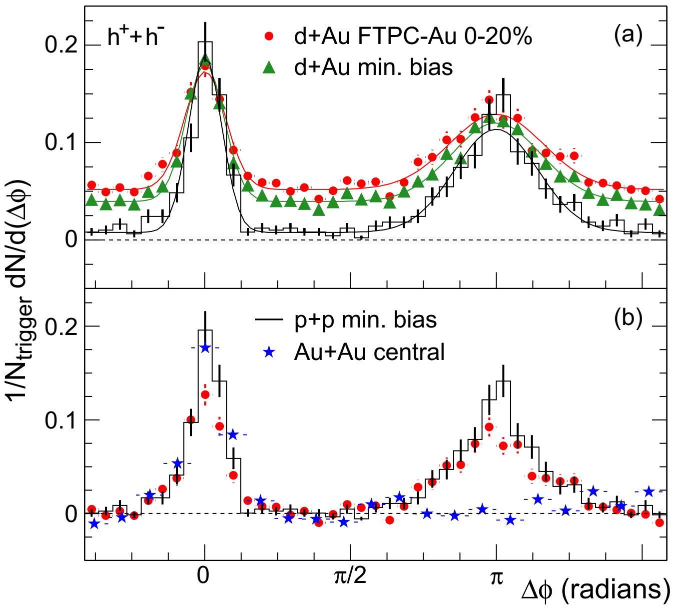

Figure 1.10: Jet quenching results from the STAR experiment at RHIC, Brookhaven. Evidence of QGP formation is shown by the absorption of jets in Au-Au collisions, but with no corresponding absorption in p-p or d-Au collisions

was made by the RHIC collaborations and is given the name R_{AB} as it is the ratio between two types of collisions using different nuclei (equation 1.2).

$$R_{AB}(p_t) = \frac{1}{N_{\mathrm{coll\,A}}} \times \frac{\mathrm{d}^2 N_{\mathrm{AA}}/\mathrm{d}p_t \mathrm{d}y}{\mathrm{d}^2 N_{\mathrm{pp}}/\mathrm{d}p_t \mathrm{d}y} \tag{1.2}$$

Where N_{collA} is the number of particles involved in the collision Using this definition STAR[27] found a suppression of tracks with $P_T > 3$ GeV/c. This suppression is shown in Figure 1.11. The shape of the d+Au points is caused by the Cronin effect[24], however due to the absorption in the dense QGP region the Au-Au points are suppressed to be below 1[25].

High P_T suppression studies are not limited to heavy nuclei versus p-p or lighter nu-

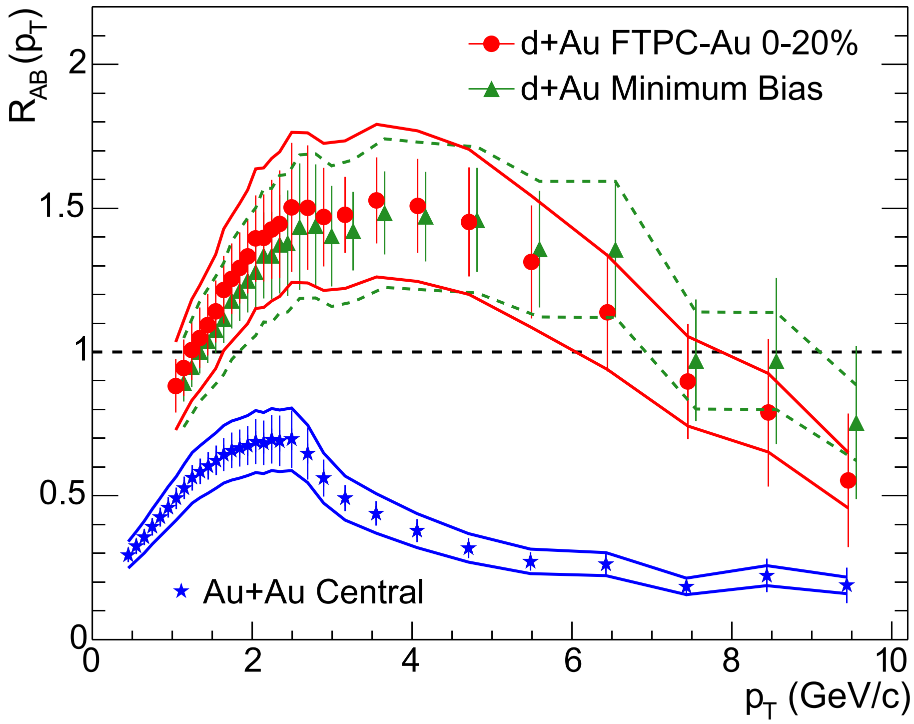

Figure 1.11: High P_T suppression found by the STAR experiment at RHIC, Brookhaven, Shown using R_{AB} nuclear modification factor

clei collisions. Looking at the ratios of central to peripheral collisions can also show interesting results. A definition of central and peripheral collisions is given in the next chapter and studies of this quantity are done within this thesis. Past studies of the central to peripheral ratio (R_{cp}) have been done by the WA98 experiment[26] and at RHIC by the STAR experiment.

1.5.7 Negatives

In order to model and understand any system all aspects of it must be incorporated into the model. Therefore, any model of the QGP must incorporate everything that comes out of it as it hadronises. By looking at non-strange particles that come from the impact a baseline for strange particle production and other signals can be established. As the initial charge of the nucleus is positive any signal of positive charges would reflect this and so not give an unbiased signal. Therefore only negative tracks are considered as these will have been created in the initial collision. There are several things that need to be looked at when considering negatives, such as the dependence on energy and impact parameter. The results will provide information on the system evolution. In addition, when a plasma is formed the entropy of the system is increased so when it hadronises this entropy should not be lost. The easiest way of doing this is to create more pions. Although pions are not the only negatively charged particles which originate from the initial collision they are expected to make up the majority of the particles. As there is no particle recognition system within the NA57 experiment all the negative tracks which are analysed are considered to be pions. This increase in entropy of the system will show up as a small enhancement in negatives when a QGP state of matter is created. Recent studies seem to support this and show that entropy is only weakly affected by freeze-out (i.e. hadronisation) [28]. Another reason that there may be an enhancement in negatives is the fact that not all of them are pions. Although the vast majority will be pions some of them will be kaons which are strange particles. These particles will be enhanced as stated previously, therefore a small enhancement is expected due to this. These two effects together are expected to cause an enhancement that is predicted to be approximately 30% when a QGP is formed [7]. The NA57 experiment is looking to repeat the analysis of the WA97 experiment to measure enhancements for negative particles. The majority of this thesis is aimed at finding yields of negative particles which will allow enhancements to be calculated.

Chapter 2

The NA57 Experiment

2.1 The Super Proton Synchrotron

The NA57 experiment is based at CERN in Switzerland and uses the Super Proton Synchrotron (SPS). The SPS ring is the fourth stage in acceleration and produces a beam of high energy protons, or heavy ions. The process begins in the LINAC part of the accelerator which accelerates the particles to various energies. For protons this is approximately 50 MeV/c, for electrons 500 MeV/c and for lead ions 4.2 MeV/c per nucleon[29]. These particles are then fed into the Booster Synchrotron (PSB) ring where they can be boosted to higher energies, reaching 1 GeV/c for electrons. This then feeds into CERN's original accelerator ring, the proton synchrotron (PS). The PS now acts as a feeder ring for the ISR (Intersecting Storage Rings) which, in turn, feeds into the SPS. In the SPS, protons can reach energies of 450 GeV/c[30] and the lead ions can reach energies of 170 GeV/c per nucleon[29]. The SPS has also been used to collide two beams of particles (protons and anti-protons) moving in opposite directions around the ring (where the W and Z particles were first discovered in 1983), and as a feeder ring for the Large Electron-Positron storage ring (LEP). For the purposes of the NA57 experiment, its most important function is to supply a beam of either protons or lead ions to the north area of CERN (or the west area for the previous experiment WA97). This beam is then used to collide with a fixed target and allow us to study the Quark-Gluon Plasma and the phase change to this state of matter. The overall layout of the SPS is shown in Figure 2.1[29]

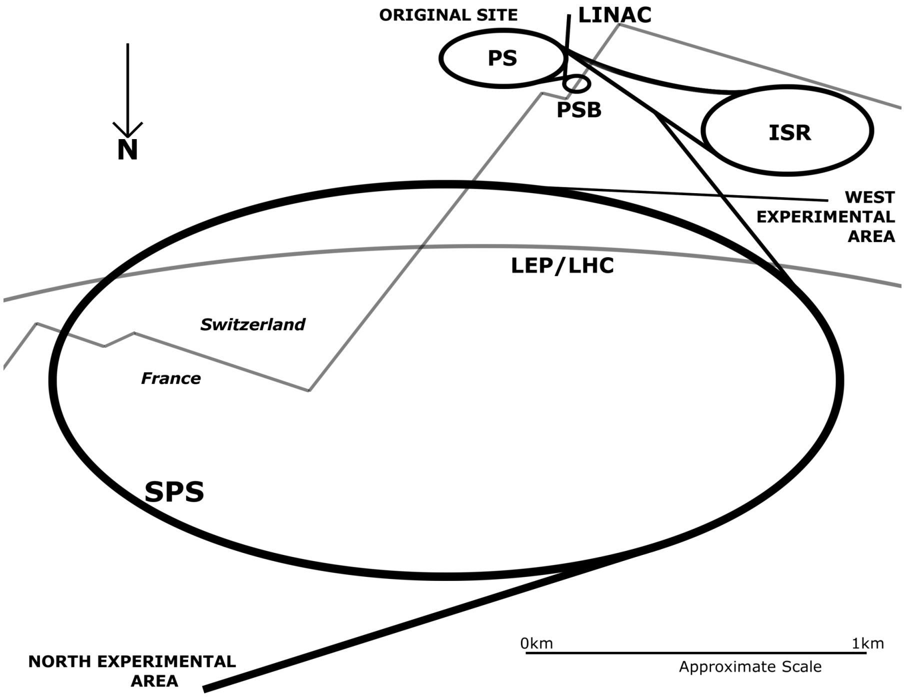

Figure 2.1: Layout of the SPS at CERN, Switzerland

2.2 Motivation

As mentioned previously, the NA57 experiment is a fixed target experiment that has been run at energies of 158 GeV/c per nucleon and 40 GeV/c per nucleon in the laboratory frame. It involves colliding a lead ion beam onto a lead target. The main aim of the NA57 experiment is to look for strangeness enhancement as a signal of QGP formation. To do this, the data from the Pb-Pb collisions, in which a QGP is expected to be formed, are compared with data taken from a proton beryllium interaction, which is used as a control. No QGP is expected to be formed in a p-Be interaction. Beryllium is used as it is a very small nucleus that is easy to use. Hydrogen and helium are not used as they have too low a density even in liquid form. Lithium oxidizes with air very quickly and so is not a particularly good target to use. In addition, it does not have equal number of protons and neutrons and so would provide uncertainty in the results when compared to p-Pb or Pb-Pb events. Beryllium is the next lightest element and its stability makes it the best choice as a target in the control runs. As described in section 1.5.1 the WA97 experiment found an enhancement of strangeness that was greater than expected for pure hadronic gas interactions. There was an enhancement of a factor of five going from p-ion interactions to Pb-Pb interactions for Ξ and an enhancement of more than an order of magnitude for Ω. This was an important factor which led to the announcement by CERN in February 2000 that a signal had been found for a new state of matter.

The NA57 experiment extends the results of the WA97 experiment in two ways. Firstly the centrality range over which data can be taken was increased and so was able to look at data going down to 50 wounded nucleons, whereas WA97 could only go down to 100 wounded nucleons. The second improvement is to look at a beam energy of 40 GeV/c per nucleon which is expected to sit on or be very close to the phase boundary.

2.3 Definitions

Throughout the analysis of the various data series that are looked at in this thesis various terms are used to desribe the conditions of the experiment. Some of these terms are well known but are defined in this section for clarity.

2.3.1 Centrality

Centrality is a measure of how "head-on" the collision between the colliding particles is. When two Lorentz contracted particles collide they can hit each other head-on or hit with a more glancing blow. The centrality of the collision is done by looking at the charge multiplicity of each event. This is discussed later in the section about multiplicity strips. A collision that is not head-on is called a peripheral collision. The basic premise of the centrality of a collision is shown in Figure 2.2 below:

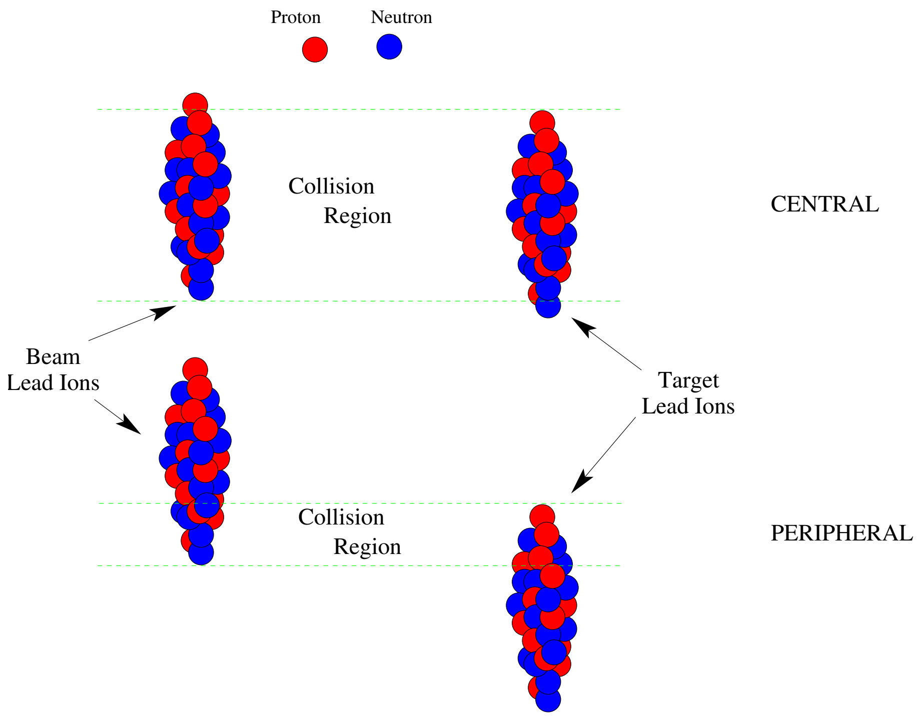

Figure 2.2: Diagramatical representation of a central and peripheral collision of lead ions

2.3.2 Acceptance Window

Because the detector used in NA57 only covers a portion of phase space not all particles created pass through it. This means that some particles will pass through the edges of the detector and possibly not the whole thing. In an attempt to remove any edge effects of the telescope an acceptance window is defined in a Rapidity-P_t plane with limits put on both minimum and maximum values of the Rapidity and P_t. The edges of the telescope are also defined using angles to link these minimum and maximum values. The edges of this window are defined using these angles by using the following formulae:

$$\text{Upper Edge} = \frac{M^*}{\sqrt{(1.0 - (\theta * \sinh(Ylab))^2)}}$$

$$\text{Lower Edge} = \frac{M^*}{\sqrt{(1.0 - (\phi * \sinh(Ylab))^2)}}$$

The M^* value is a variable similar to the mass of the particle being analysed, i.e. for lambda particles this value is 1.116 (expressed in GeV/ for consistency with P_t) and Ylab is the rapidity in the laboratory frame of reference. However, the analysis of this thesis is based around negatively charged hadrons and so the variable is not an exact mass as there is more than one particle species involved. The actual value used is decided upon in the analysis of the data sets.

The concept of the acceptance window becomes clearer when it is shown on a Rapidity P_t plot. By applying the values in Table 2.1 a plot can be drawn of the acceptance window as shown in Figure 2.3. During analysis this window is defined using values appropriate for the data and represents the region of acceptance within the detector. Its exact position is determined so that it removes all particles with a *weight* 10 times greater than the smallest *weight*. An explanation of weights and how they are calculated is given in the next chapter.

Table 2.1: Table of Variables used to define acceptance window in Figure 2.4

P_t		Ylab		θ	ϕ	M* variable
Min	Max	Min	Max			
0.22	2.5	2.5	3.75	0.045	0.15	0.2

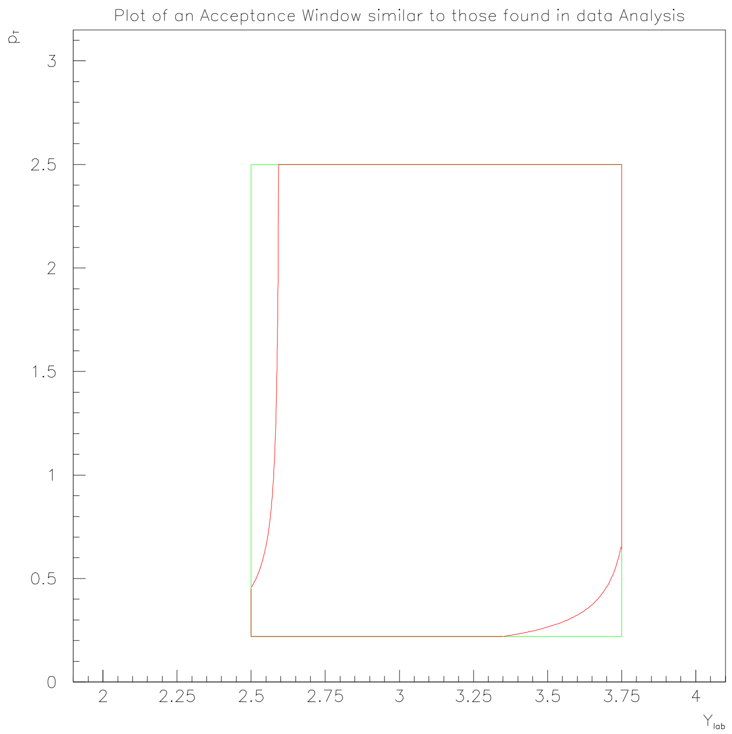

Figure 2.3: Acceptance window as defined by values in Table 2.1. This is used as a representation of the detector to define the region of phase space it covers. Values are fitted to data sets individually.

2.3.3 Yields, Slopes and Background Correction

Once the weighting chain has been completed for all tracks sampled and weights have been calculated for them the next step is to calculate the particle yields, inverse slopes and background corrections. The calculation of the yields is a fairly straightforward calculation, however it must include the background correction factors. The slope is slightly more difficult to calculate and is done using a fitting program. The basics of how it calculates the slope is discussed later in this section.

The inverse slope is, in essence, a measure of the temperature of the fireball at freeze out. It is estimated by a fitting program from the weighted data. In past analysis of strange particles the rapidity distribution was assumed to be flat, however for negative particles this may not be the case and it will be considered in later chapters. The slope is extracted using this fit within the formula:

$$\frac{d^2N}{dm_T dy} = m_T\, f(y) e^{-\, m_T/T}$$

where *f(y)* is the rapidity distribution function. A maximum likelihood fit method is used to obtain T. This is shown in Appendix C. It can also be calculated by plotting $ln\left(\frac{1}{m_T}\frac{dN}{dm_T}\right)$ against m_T.

The background correction is done by considering data taken with no target present. These data, referred to as *empty target data*, were taken in a few runs for all data sets and allow us to get an idea for what fraction of reconstructed tracks do not originate from the interaction in the target. This correction is added to the basic formula used to calculate the yield of particles. This formula is shown below:

$$Yield = \frac{\sum \text{Weights}}{N_{samp}} \times \text{ Extrapolation factor } \times \text{ Background correction}$$

The background correction is done in two stages, first the correction to the number of sampled events. This is simply the number of events found in the background files normalised to the number of beam interactions divided by the number of events in the data set normalised to the number of beam interactions. This number is then subtracted from 1 so that if there is no background correction then there is no change to the number. The second stage is the correction to the sum of weights, as if there are background events in the sample these will have been weighted as well. This is done in a similar way to the first correction but with the number of tracks being considered rather than the number of events. This makes the background correction:

$$N_{samp}\ \text{Correction}\ = 1 - \frac{\frac{M^E_{ET}}{CB\overline{DT}_{ET}}}{\frac{N^E_{full}}{CB\overline{DT}_{full}}}$$

$$\sum\ \text{Weights Correction}\ = 1 - \frac{\frac{m^T_{ET}}{CB\overline{DT}_{ET}}}{\frac{n^T_{full}}{CB\overline{DT}_{full}}}$$

Where CB.$\overline{DT}$ is the normalization factor for the number of beam interactions where the experiment could have recorded an event, M^E_{ET} is the number of events in the empty target data, N^E_{full} is the number of events in the data set being corrected for, m^T_{ET} is the number of tracks in the empty target data within the cuts defined and n^T_{full} is the number of tracks in the data set being corrected for within the cuts defined.

The Extrapolation factor is used to extrapolate the data to a range of 1 unit in rapidity. This is done to reduce the effect of choosing the acceptance window. It consists of integrating the data within a rectangular region with a width of one unit of rapidity centred on mid-rapidity and a P_T range of $0 < P_T < 20$ GeV/c (or M_T range of $M < M_T <$ 20 GeV/c) which is essentially the same as doing the full P_T range. This is the divided by the integral over the acceptance window.

$$Extrapolation\ Factor = \frac{\int_{CM-0.5}^{CM+0.5} f(y)\, dy.\ \int_{M}^{20} M_t e^{-\frac{M_t}{T}}\, dM_t.}{\iint_{window} \frac{d^2N}{dm_T dy}\, dy.\, dM_t.}$$

2.4 Data Collection

The NA57 experiment took data over the course of several different years. This data was collected at the two energies described previously, 158 GeV/c and 40 GeV/c. Table 2.2 shows all the data sets taken by the NA57 experiment, the date when they were taken, the number of events recorded, the energy of the collisions and the

Table 2.2: Data collected by NA57.

System	Beam momentum	Sample size	Collected
Pb-Pb	158 A GeV/c	230 M events	November 1998
p-Be	40 GeV/c	60 M events	July 1999
Pb-Pb	40 A GeV/c	290 M events	November 1999
Pb-Pb	158 A GeV/c	230 M events	October 2000
p-Be	40 GeV/c	110 M events	September 2001

nuclei collided.

For the 158 GeV/c data sets the WA97 158 GeV/c p-Be results were used as reference data. For the purposes of this thesis the 3 Pb-Pb data sets will be considered. Further details of these data sets are given throughout the rest of this thesis.

2.5 Set-up

The experimental apparatus itself is made up of several key parts. These include the target and beam, scintillators which are connected to the trigger, the multiplicity detectors (MSD) which provide a measure of the centrality of the collision, the telescope which consists of several silicon planes, and the Goliath magnet. There are also trigger and data acquisition systems which decide if an event is of interest and keep a record of it and all its information if it is selected. Different years of data taking had small changes to the configuration. Some of these changes were made to take into account the energy and particle species of the beam, others were made in later data taking years after experience was gained in the early years. These changes were mainly in the telescope set up, the configuration and position. However, the basic make-up of the experiment remained the same. The set-up for the 1998 Pb-Pb run at 158 GeV/c is shown in Figure 2.4

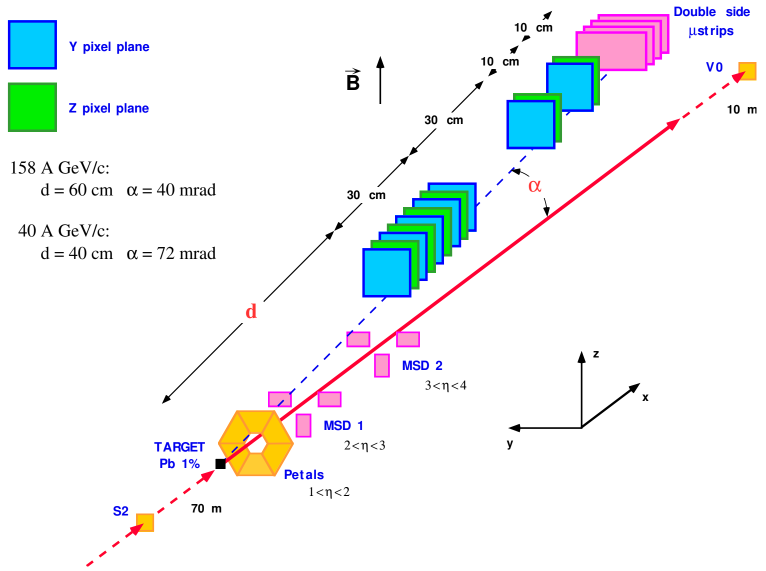

Figure 2.4: The NA57 Experimental layout

2.5.1 The Goliath Magnet

With the exception of the S2 quartz Cerenkov counter which was 70 metres upstream, the layout in Figure 2.4 was all fixed to an optical bench which was placed inside the Goliath magnet. The co-ordinate system of the apparatus was made such that the beam travelled along the X-axis (before any interaction) and the magnetic field went approximately along the Z-axis. This meant that any charged tracks would bend in the X-Y plane and so the charge and momentum on any particle travelling through the telescope would be easily detectable. A detailed map of the field was also taken to reduce tracking errors.

In addition to the Goliath magnet, there was a smaller compensating magnet called

David which runs at about 1500A, about half the current used in Goliath [31]. Together they produced a magnet field of approximately 1.4 Tesla. Half way through any set of runs the polarity of the magnet was changed so half the final data was with the field up and half with the field down. This was done to minimise systematic errors due to the magnetic field.

2.5.2 Multiplicity detectors

To measure the centrality of the collision, a system of microstrip detectors (MSD) was used to measure the multiplicity of the collision. This was done over the pseudorapidity range $2 < \eta < 4$. The Glauber model [32] was used to estimate the number of participating nucleons from the multiplicity. It assumes that the average multiplicity of a collision is proportional to the number of nucleons that were involved in at least 1 inelastic collison with another nucleon (a "primary" collision)[33]. This number is often referred to as the number of wounded nucleons.

2.5.3 Telescope

The telescope itself was an array of pixel planes positioned on an optical bench. There were two different types of planes, the Omega2 and Omega3 planes. Both are silicon detectors which are split into pixels and they both have read out chips bonded to them; this arrangement is called a ladder. The Omega2 ladder had pixel sizes of 75μm by 500μm and contained 1006 sensitive cells per chip[33]. The Omega3 ladder had a pixel size of 50μm by 500μm and contained 2032 sensitive cells per chip[33]. For Omega2 planes 6 ladders were then put together to form an array and then 2 arrays were placed back to back and slightly staggered to form a plane with a sensitive area of about 5 by 5 cm^2. The same was done for the Omega3 ladders but only 4 were used to make an array. The average thickness seen by a particle going through a plane is 1.7 % of a radiation length [34]. A schematic diagram of one of the planes is shown in Figure 2.6[35]

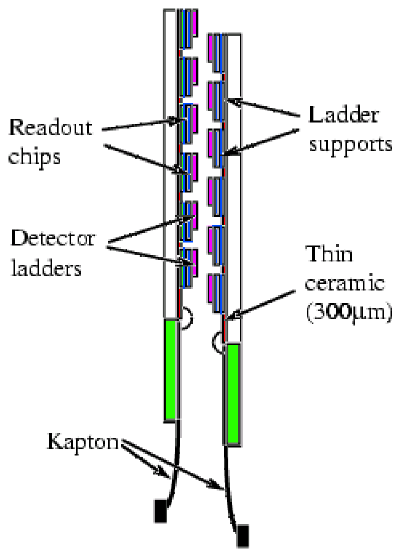

Figure 2.5: Schematic diagram of a pixel plane

The three data sets analysed in this thesis all have slightly different set-ups for the telescope. In the 40 GeV Pb-Pb data set taken in 1999 there were 10 planes used in the compact part of the telescope, each made of the double planes described previously. In the 158 GeV Pb-Pb data set taken in 2000 the compact part of the telescope had 11 planes. However for analysis purposes the 10th plane was used as the definition of the last plane. This was so that any cuts made using the last plane between data sets were kept as similar as possible. The 1998 data taken at 158 GeV/c for Pb-Pb had 9 planes in the compact part of the telescope. This set up is that shown in Figure 2.6. It also has 4 extra planes that were placed further away from the compact part of the telescope(2 an extra 30cms away and 2 an extra 40 cm away); This allowed high momentum tracks, to be tracked over a longer distance, so that their curvature could be measured better. They were moved into the compact part of the telescope for 2000 data taking as the efficiency of the planes deteriorated over time.

The final difference between the data sets is in the angle at which the telescope is positioned and the distance from the target. In both the 158 GeV/c data sets (1998 and 2000) the telescope was positioned at an angle of 40 mrads and a distance of 60 cm from the target. In the 1999 40 GeV/c data set the angle was 72 mrads and the distance was 40 cm. These angles were chosen so that the telescope was positioned to accept tracks emitted around 90^o in the centre of mass frame.

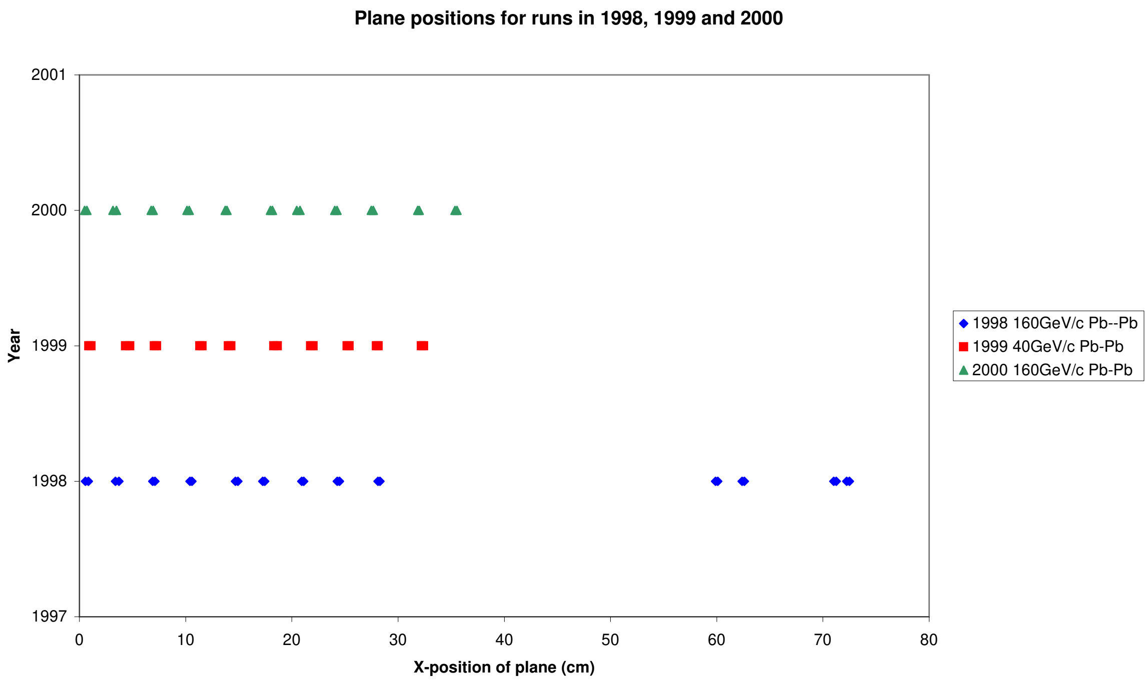

Figure 2.6: Layout of the compact telescope planes for data sets taken in 1998, 1999 and 2000, X-position in this plot is defined as position along the x-axis before the telescope is inclined

As with most electronic systems, data cannot be taken all the time, there is a period of dead time after each event is selected when data are written to tape. This time is called "dead time", and is taken into account by the triggering system for the experiment. A counter was set up that measured the number of beam particles while the experiment was active, i.e. not in dead time mode. This counter is essentially recording the number of possible events that could be taken by the experiment during running. For the purposes of this analysis it is called CB.$\overline{DT}$ where the CB stands for clean beam. CB.$\overline{DT}$ is a number which will be used in background corrections later in this thesis.

Chapter 3

Analysis Techniques

3.1 Negatives Analysis

The analysis of the three different data sets described in Section 2.4 is very similar. However, there are, some subtle differences that must be taken into consideration such as the set-up of the apparatus. In the following chapter the analysis used on the data sets will be described together with some of the investigations carried out into the data. The differences between data sets will be highlighted and fully explained. The main goal of the analysis is to produce yields for the data that can be used in future analysis to define any enhancements, to produce inverse slope values for all the data sets as a measure of the temperature of the fireball and to produce R_{cp} results for all 3 data sets. These results will be shown in later chapters along with comparisons of the results and any error studies carried out.

3.2 Real Data

3.2.1 Processing

Over the course of a data taking period, millions of tracks are recorded. A large proportion of these tracks originate from the collision region and just under half of these are negatively charged. Only a representative sample of the negative tracks need to be analysed in order for the statistical error to be much less than the systematic error. Therefore for the purposes of the majority of the analysis in this thesis the 'background data' is used. Background data is a sample of all the data taken from a particular year. It is roughly $1/100^{th}$ of the total data taken, although the exact amount varies from year to year. This background data is sampled so that background studies can be carried out, and so that it can be mixed with Monte Carlo data in analysis. This background data is then split into several files so that the file sizes do not become unmanageable. A summary of the number of files and the number of tracks within the background files is given in Table 3.1

Table 3.1: Number of events and tracks within the background files and the number of files each year is split into.

Year and Energy	Number of Background Files	Number of events	Number of tracks
1998 - 158 GeV/c	17	1,068,265	10,593,873
1999 - 40 GeV/c	14	1,162,946	4,703,945
2000 - 158 GeV/c	24	1,132,462	12,181,314

During data taking, the recorded data is split up into segments called *runs*. Taking the data in different runs means that if a problem occurred during a particular period of data taking then the corresponding run could be disregarded and not used in any analysis. It also meant that between runs the experimental set up could be checked to spot any problems and a record of any problems or changes could be made. For example, knowing the run number when the field polarity was changed means that the data can be easily looked at in either set-up.

The data taken was recorded in a "*raw*" format. This is basically a record of the hits within the planes of the pixel telescope, the hits recorded in the multiplicity detectors and any other detectors used, and the run and event number. To analyse the raw data it must first pass through a program called ORHION, which is a standard piece of code used within the NA57 collaboration. This takes all the available information from the run and combines it with information about the run which is stored in a database. This information includes details such as the beam position in x, y and z directions, the angle and set up of the telescope and any details that may change between runs. It traces the tracks through the hits made and reconstructs them, finally producing a DST output file with information on each track it could reconstruct. The information on the tracks includes momentum components in the x, y and z directions, the impact parameters on the target for y and z directions, the multiplicity of the event, the event number and run number.

Although the ORHION DST output has all the track information, it has to be run through another program which converts it into a readable format. This program is called DSTLOOK. DSTLOOK is a standard piece of analysis code used within the NA57 collabortion which was modified slightly for the analysis of negative particles. As well as producing an ntuple which can be analysed, DSTLOOK also defines a few things such as the last plane of the telescope which can be used to define cuts on the data.

PAW (Physics Analysis Workstation)[36] is then used to analyse the ntuple and define various cuts on the data and look at the variables associated with the tracks. PAW is used throughout the analysis of this thesis. Selection cuts are defined to isolate negative tracks produced in the initial interactions, the main one of these is a cut on the impact parameters to make sure the tracks come from the target region. These selected tracks within the defined cuts are then used to generate Monte Carlo data and run through a weighting chain. They are then used to extract the yields and inverse slopes of the data.

3.2.2 Impact Parameter Selection Cut

One of the main features of the negative tracks that are to be analysed is that they come from the target. A simple plot of BY and BZ (the y and z axis impact parameters relative to the target) at the nominal x position of the target, which was set to 0cm in the co-ordinate system used, allows an idea of the sort of cut involved to be gained. This is plotted in Figure 3.1 for the 1998 158 GeV/c data and in Figure 3.2 for the 1999 40 GeV/c data overleaf. The 2000 158 GeV/c data shows the same features as the 1998 158 GeV/c data. To make the plots clearer only one of the background files has been used for each of the plots.

The plots show two distinct features, a concentration of impacts at the beam position and a smaller concentration approximately 1 cm above the beam position. This suggests that there are some interactions happening, in the beam line, up stream of the target. The only detector before the target is the S2 scintillator which is used by the trigger to detect the beam. This is located 70m upstream of the target and so any interaction in it would have dispersed by the time it reaches the telescope as there are magnets between it and the telescope. Figure 3.2 shows that in the 1999 data set the second interaction region is more clearly defined. It is in this data set that the secondary interaction region is separated from the target interaction region

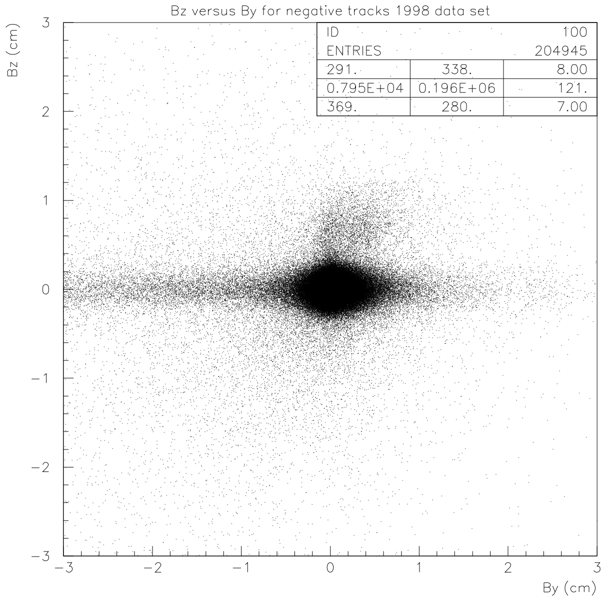

Figure 3.1: BZ impact parameter vs BY impact parameter at X=0cm position for the 1998 158 GeV/c data set, negatively charged tracks.

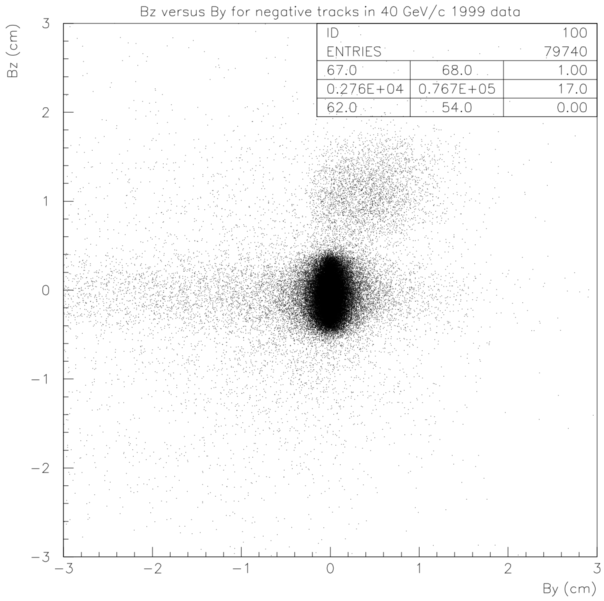

Figure 3.2: BZ impact parameter vs BY impact parameter at X=0cm position for the 1999 40 GeV/c data set, negatively charged tracks

more clearly and the background surrounding the two regions is smaller. Therefore, by using this set up, it will be easier to understand the origin of this unknown interaction. By considering the position of the telescope and the position the interaction traces back to at X=0cm an equation for the path of the track can be set up. This can then be traced back to the Z=0 position, i.e. where the track intersects with the beam path and so originates from. This set up is shown in Figure 3.3 along with the calculation to estimate the origin of the extra tracks.

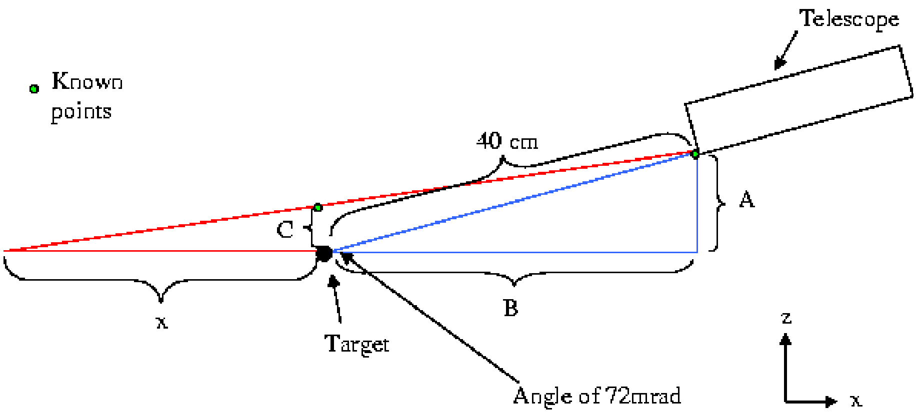

$A = [Sin(72 \times 10^{-3}).40]$

$B = \sqrt{40^2 - A^2}$

C = 1

2 known points of the unknown track are (0 , 1) and (B , A). From this the gradient of the line can be found as can the intercept at X=0. These can then be traced back to find the X position at Z=0.

$A \approx 2.88cm$

$B \approx 39.9cm$

$Gradient \approx 0.047$

$X\ at\ Z(0) \approx -21.25cm$

Figure 3.3: Secondary interaction tracing for the 1999 data at 40 GeV/c.

By doing this it can be seen that the second peak comes from an interaction at approximately -21 cm ± 5cm, i.e. 20cm before the target. This value is only approximate though as even a small change in the Z co-ordinate can mean a big change in the X co-ordinate due to the very small angles involved. The error has been calculated with this in mind by varying the z position of the secondary interaction as 1 cm $\pm$ 1mm. By performing the same analysis on the 1998 158 GeV data the second bump can also be traced to -20 $\pm$ 8cm, roughly the same as the 1999 40 GeV data, this suggests that the cause of the secondary interaction is the same in both cases. A BZ position of 0.6 cm was used for the 1998 data set.

This means that any cut made in BZ must remove the tracks that come from this bump. The origin of the bump cannot be the S2 scintillator as this is simply too far away. The beam pipe however does not simply run through the experiment. The pipe ends approximately 20cm from the target and the end of this is covered with a very thin layer of MYLAR to maintain the vacuum within it. This piece of foil is positioned at about the right distance from the target to explain the bump. The fact that the bump is also only a small fraction the size of the main peak in BZ suggests that the target is thicker and/or more dense than the material causing the second bump. This is the case with the foil that covers the end of the beam pipe as it is made of 10 μm of MYLAR which is 15% Carbon and 85% Hydrogen.

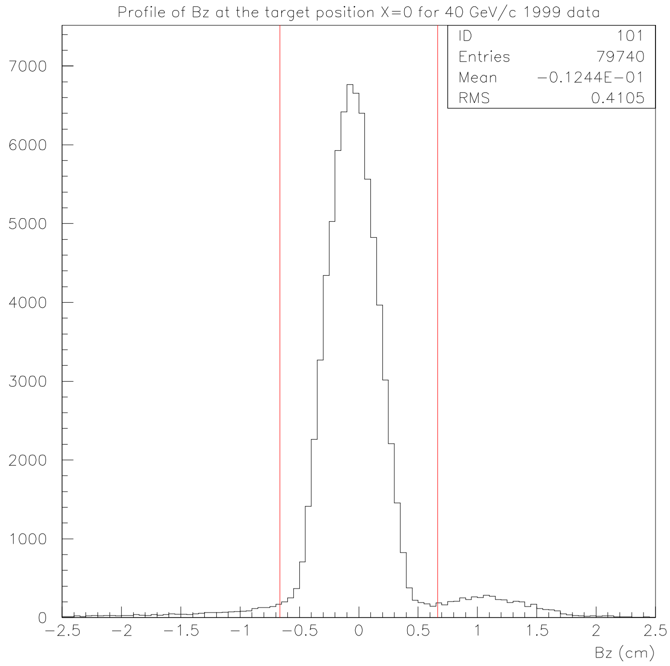

Figure 3.4: Profile of BZ at target position X=0 for the 1999 data at 40 GeV/c negatively charged tracks.

Figure 3.4 shows where the BZ cut has been defined in relation to this second bump for the 1999 data. The actual value of this cut is 0.67 cm. This is because the exact beam position varied slightly from run to run which means that all runs need to be considered and not just the ones in the background file used in the plots.

In the 158 GeV data sets the secondary interactions were not as intense. By looking at Figure 3.5 of the 1998 data the bump is hardly visible at all. This means that the BZ impact parameter for the 158 GeV data sets can be made momentum dependent if needed as it is not restricted by the secondary interaction.

To see if a momentum dependent cut is necessary plots of BZ in various slices of momentum can be considered. This is shown in Figure 3.6 for 1998 and 3.7 for 2000. The cuts that were defined on them are shown on the plots and are identical

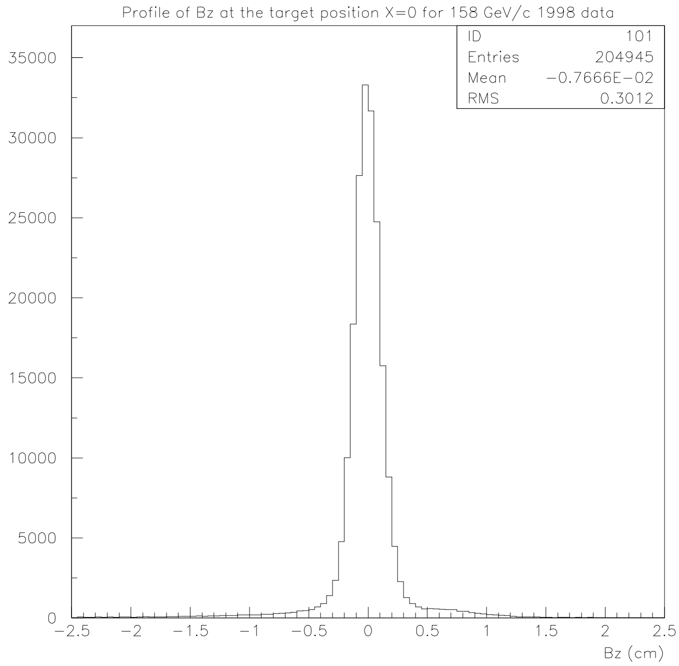

Figure 3.5: Profile of BZ at target position X=0 for the 1998 data at 158 GeV/c negatively charged tracks.

in both cases. A summary is given in Table 3.5 after the discussion of the BY impact parameter. In the 1998 data set the final cut on the high momentum tracks is a little tighter than the others, this is due to the 2000 data set cuts being defined previously and the decision to be consistent with the cuts between the data sets. Although it is a very tight cut it still retains the majority of the data.

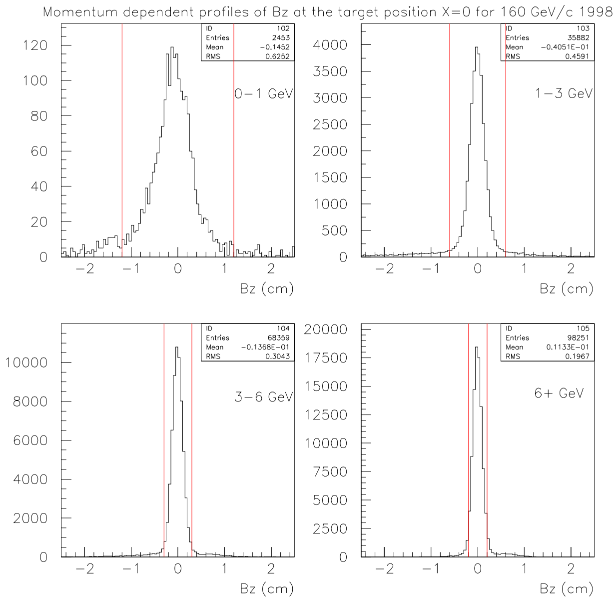

Figure 3.6: Momentum Dependent profiles of BZ at target position X=0 for the 1998 data at 158 GeV/c negatively charged tracks.

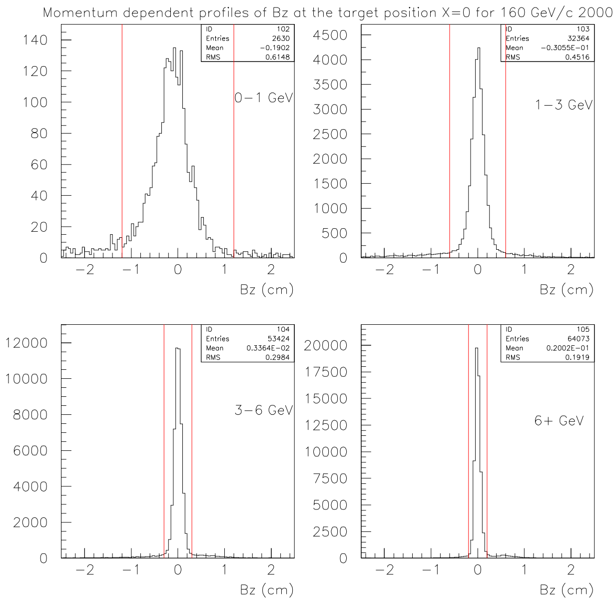

Figure 3.7: Momentum Dependent profiles of BZ at target position X=0 for the 2000 data at 158 GeV/c negatively charged tracks.

The BY impact parameter can be looked at in a similar way as the BZ impact parameter. A look at the profile shows a simple peak which allows a cut to be defined around it. The profile of the 1999 data is shown in Figure 3.8; again it is shown for the smallest of the background files. Figure 3.9 shows the same profile for the 2000 data (again just one background file), the 1998 data set shows a similar profile to the 2000 data.

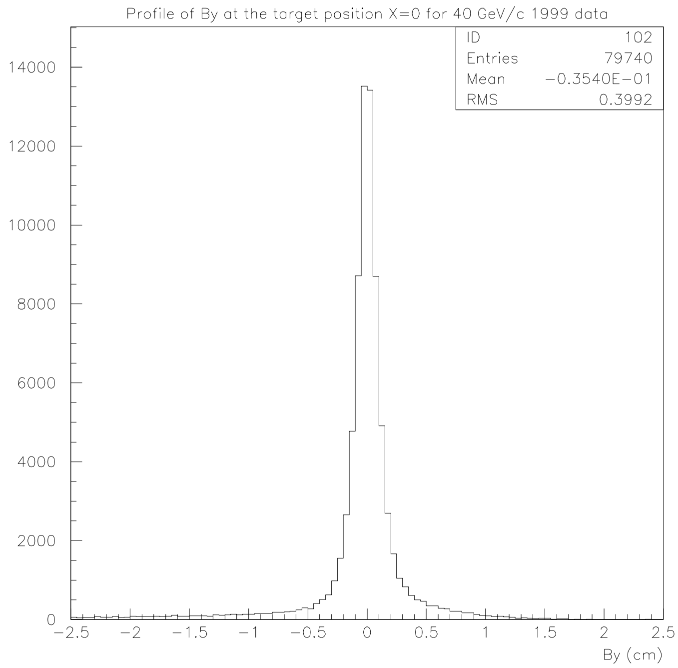

Figure 3.8: Profile of BY at target position X=0 for the 1999 data at 40 GeV/c negatively charged tracks.

However, simply looking at the profiles does not show the full story with regards

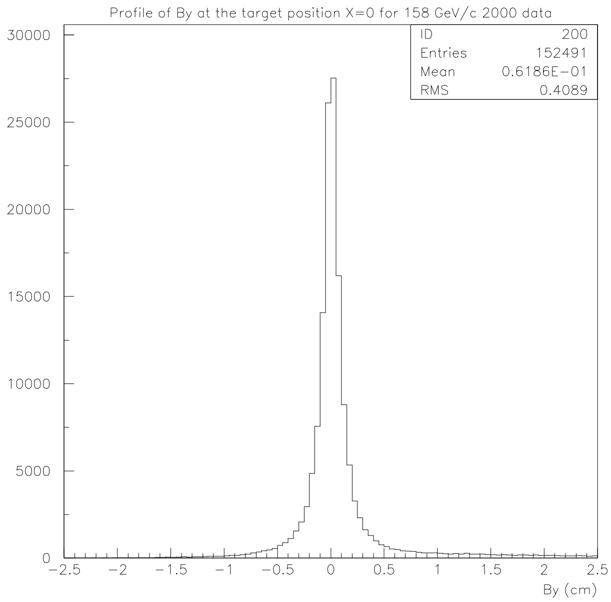

Figure 3.9: Profile of BY at target position X=0 for the 2000 data at 158 GeV/c negatively charged tracks.

to the BY impact parameter. By looking at the impact parameter as a function of momentum another feature is revealed. Along with the central column of tracks, which trace back to the target, there is another set of tracks which have a momentum dependent impact parameter. At low momentum these tracks are a good distance from the target, however at higher momentum they get closer and closer to tracing back to the target region. Therefore, a cut on the BY impact parameter is used to remove as many of these tracks as possible and an explanation of the origins of these tracks is needed. The momentum dependent profiles of the 1999 and 2000 data are shown in Figures 3.10 and 3.11 respectively to illustrate this *"wing"* effect. The wings appear on opposite sides in the two figures due to the magentic field being in opposite directions in the two figures. A study of the momentum dependence of the BZ impact parameter does not show any similar effects. This suggests that whatever causes this effect in BY comes from the target. A momentum dependent plot for BZ is shown in Figure 3.12 using the 1999 data set.

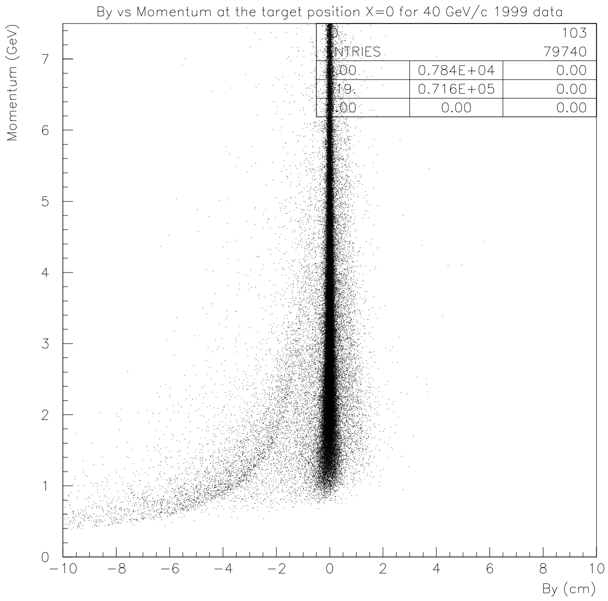

Figure 3.10: Momentum dependent profile of BY at target position X=0 for negatively charged tracks in the 1999 data set at 40 GeV/c.

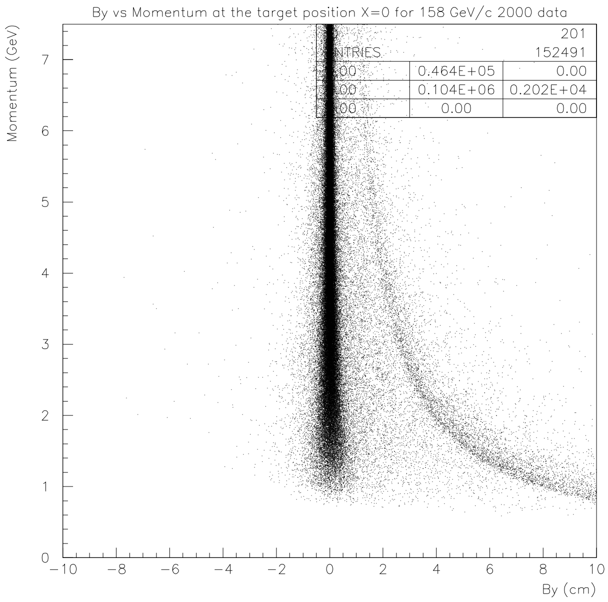

Figure 3.11: Momentum dependent profile of BY at target position X=0 for negatively charged tracks in the 2000 data set at 158 GeV/c.

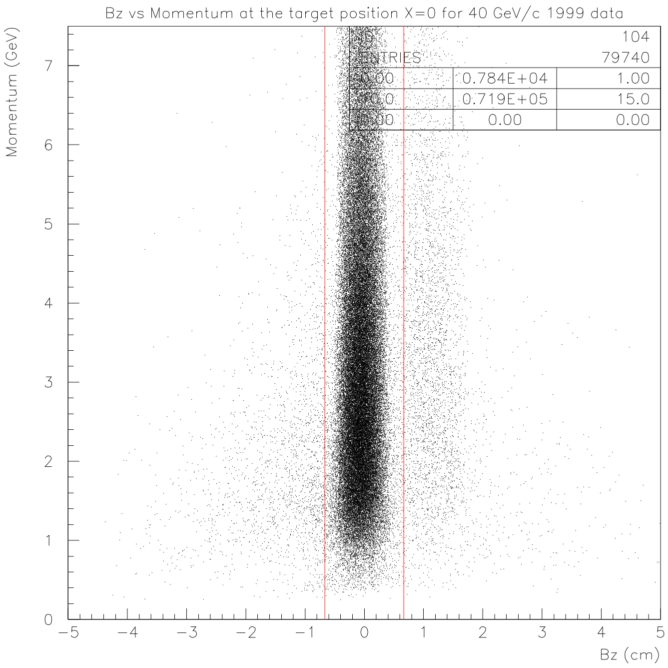

Figure 3.12: Momentum dependent profile of BZ at target position X=0 for the 1999 data at 40 GeV/c negatively charged tracks.

3.2.3 e^+e^- pairs from the first plane

The analysis of negative particles generally assumes all negative tracks are π^- tracks, however, there are roughly an equal number of π^+s and π^0s created as well. The excess of positive charge already in the nucleus before the collision means that using π^+ particles would make any results biased. The π^0 particles are not used as they do not produce a hit in the detector as they have no charge. However, the π^0 particles can decay into 2γs, and each γ can, in-turn, produce an e^+ e^- pair when it interacts with the first plane of the telescope. When the γ hits a plane it can also knock out an electron from the atoms that make up the telescope. These will still trace back to the target and so cannot be removed from the other negatives with a cut in BY or BZ. This explanation for the wings can only be valid if a π^0 decays into two γ's before it reaches the telescope. This can be shown to be true by considering the decay time of the π^0 in its centre of mass frame. Then using this and the boost at its maximum momentum it can be shown that over 66.7% of the π^0s will decay within 0.7μm of the target for the 1999 40 GeV data and 0.9μm for the 158 GeV data. It is therefore, reasonable to assume that all of the π^0s will decay before the telescope. This is shown below:

$$E = \gamma M, \tag{a}$$

$$\gamma = \frac{E}{M} \simeq \frac{P}{M} \text{ if } (P >> M), \tag{b}$$

$$x' = \gamma c\tau, \tag{c}$$

For the 1999 40 GeV data, the observed π^- momentum is about 4 GeV in the telescope, and the π^0 mass is 135 MeV [6] which can then be put into (b) to give a Lorentz boost, γ, of approximately 100. This can then be substituted into (c) along with the decay length within the centre of mass frame, $c\tau$, which is 25.1nm[6]. This gives a decay length of approximately 0.75μm. For the 158 GeV data set the mean momentum of a track in the telescope is 7 GeV, therefore giving a decay length of 0.9μm. As stated previously because the telescope is 40 or 60cm from the target, depending on which data set is being considered, it can be assumed that all the π^0s will decay before they reach it. 98.8% of π^0 decays are $\pi^0 \longrightarrow 2\gamma$[6].

Although this shows that the $\pi^0 \longrightarrow 2\gamma \longrightarrow e^+e^-$ is valid it does not show that this is what is happening. One of the ways to do this is to go back to the momentum distribution in BY and consider the minimum momentum that a track from the target can have compared to a track that is created on the first plane of the telescope.

Any track moving through a uniform magnetic field will follow a circular path if its velocity stays constant. Due to the fact that it has to travel less than one metre this is a fair approximation as energy loss can be ignored. If there is a constraint that the particle must pass through the first and last planes of the telescope, three equations can be set up for the track path. The first is the target which is at the origin. It can be said that the minimum momentum is when the track path taken has the smallest radius, therefore the track must pass through the top of the first plane and the bottom of the final plane. For the 1998 and 2000 data sets this means the co-ordinate points that it must pass through are X=60cm, Y=2.5cm and X=90cm and Y=-2.5cm. By putting these three X,Y points into the equation of a circle all three equations can be solved simultaneously to find the radius of the path,

$$R^2 = (x - a)^2 + (y - b)^2$$

This is shown in Figure 3.13 along with the calculation which shows a, which is the x co-ordinate of the centre of the circle, is 39.04cm, and b, the y co-ordinate, is -215.71cm. In this case with the track coming from the target the radius is found to be 219.21cm. This can then be used to find the momentum of the track by using the formula:

$$P = 0.3BR, \tag{e}$$

where B is the magnetic field strength, 1.4 Tesla, and R is the radius, 2.1921m. The value of 0.3 is a conversion factor that will mean the momentum, P, will be in GeV rather than in kg.m.s^{-1}. When all of this is calulated it can be shown that the minimum momentum for a track originating at the target and passing through the first and last planes of the telescope is 0.92 GeV for the 158 GeV data sets. In Figure 3.13 the co-ordinate system used has the target based at the origin, this is not the true position of the target in the NA57 co-ordinate system but it has been used to make the calculation simpler. A similar calculation can be done for the 40 GeV data set to show that the minimum momentum is 0.65 GeV.

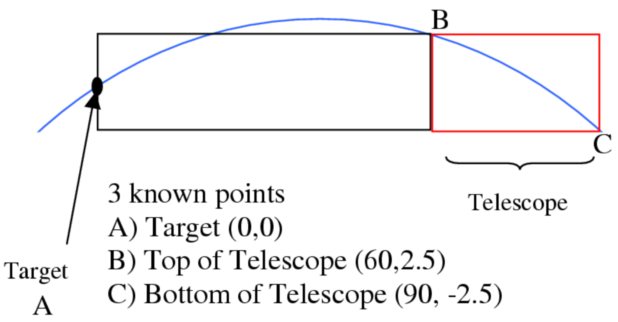

3 equations are:

- $(-a)^2 + (-b)^2 = R^2$
- $(60-a)^2 + (2.5-b)^2 = R^2$
- $(90-a)^2 + (-2.5-b)^2 = R^2$

Can be solved simultaneously to give:
a = 39.04cm
b = -215.71cm
R = 219.21cm

Momentum can be found from the radius by using:
P = 0.3 B R
P = 0.3 * 1.4 * 2.1921
P = 0.920682 GeV = 0.92 Gev

Figure 3.13: Minimum momentum of tracks from the target

When considering a track that does not come from the target a different approach needs to be used since there is less information about the track. If it is assumed that the track must pass through the first and last planes of the telescope then two points are known which it must pass through, X=40cm or 60cm, Y=2.5cm and X=70cm or 90cm and Y=-2.5cm. The easiest way to solve this is to assume that the γ hits the first plane of the telescope at an angle of 90 degrees. This means that it will be travelling at a tangent to the circular path of the e^- (and e^+) that it creates. This means that a triangle can be set up with sides of length 'radius - 5cm' and, 30cm and a hypotenuse of length the same as the radius of the circle. Pythagoras theorem can then be used to find the radius and then, as before, this can be used to find the momentum. The radius in this case is found to be 92.5 cm and the momentum is, therefore, approximately 0.39 GeV. Figure 3.13 shows the calculation and set-up for tracks coming from the first plane of the telescope. The value of 0.39 GeV for the minimum momentum is valid for all the data sets as the calculation only relies on the length of the telescope. When these values are put onto the plot of BY and

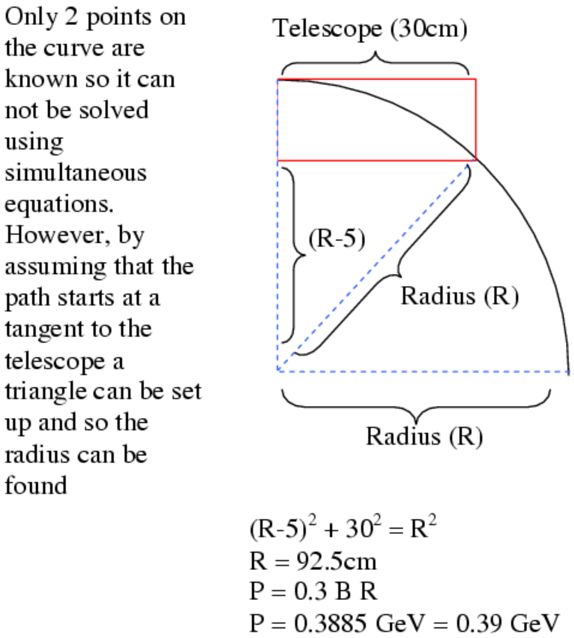

Figure 3.14: Minimum momentum of tracks from the first plane

momentum it can be shown that the minimum momentum of the wing(s) is just above the minimum calculated momentum for e^+e^- pairs. This is shown in Figure 3.15 for 1999 40 GeV data (both positive and negative tracks included for more clarity) and Figure 3.16 for 1998 158 GeV data. It further supports the theory that the wings are the result of π^0 decays.

The minimum momentum of tracks coming from the telescope also roughly matches up with those found in PAW. The extra few tracks that trace back to the target but fall below the minimum momentum are possibly due to one of the γ's striking the first plane and knocking an electron straight out instead of becoming an e^+ e^- pair or by the inital π^0 decaying straight into an e^+ e^- rather than into $\gamma\gamma$.

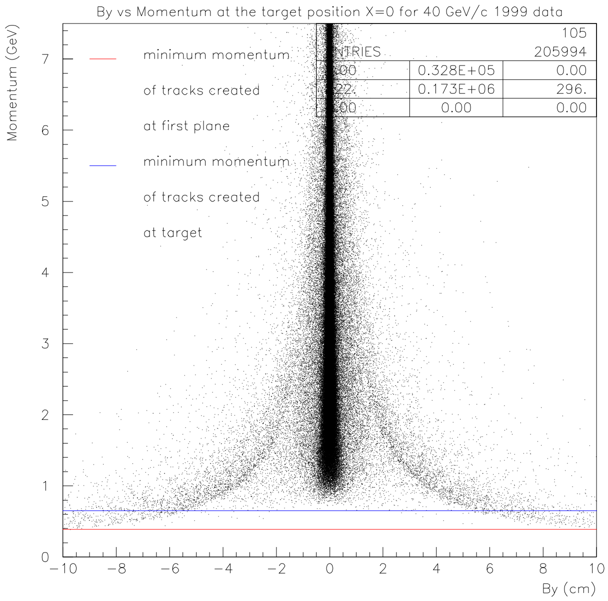

Figure 3.15: Momentum dependent profile of BY at target position X=0 for the 1999 data at 40 GeV/c all charged tracks

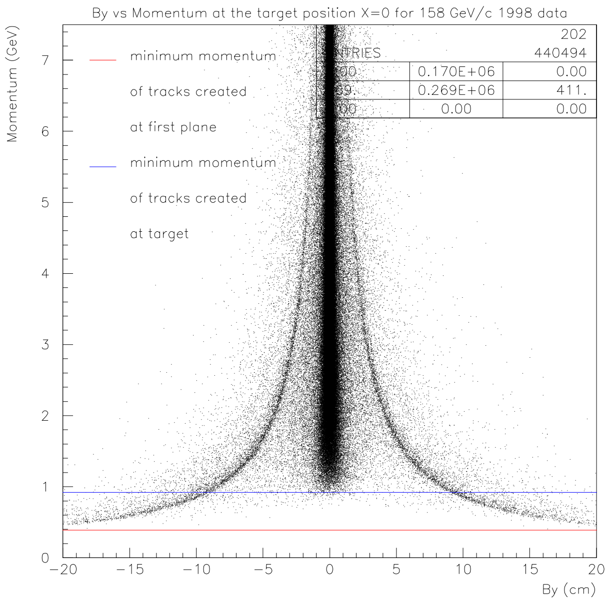

Figure 3.16: Momentum dependent profile of BY at target position X=0 for the 1998 data at 158 GeV/c all charged tracks

Figures 3.15 and 3.16 do not give a clear indication of how the density of tracks tracing back to the target compares to the density of tracks in the *"wings"*. Figure 3.17 shows a lego plot of BY vs momentum for the 1999 data as it has the least number of tracks to illustrate this density much more clearly. It shows that the *"wings"* due to e^+ e^- pairs only form a very small fraction of the total number of tracks (<1%). This means that the *"wings"* are not a huge problem in the analysis, however they still need to be removed by impact parameter cuts.

Another quick check to see if the wings are consistent with being e^+ e^- pairs

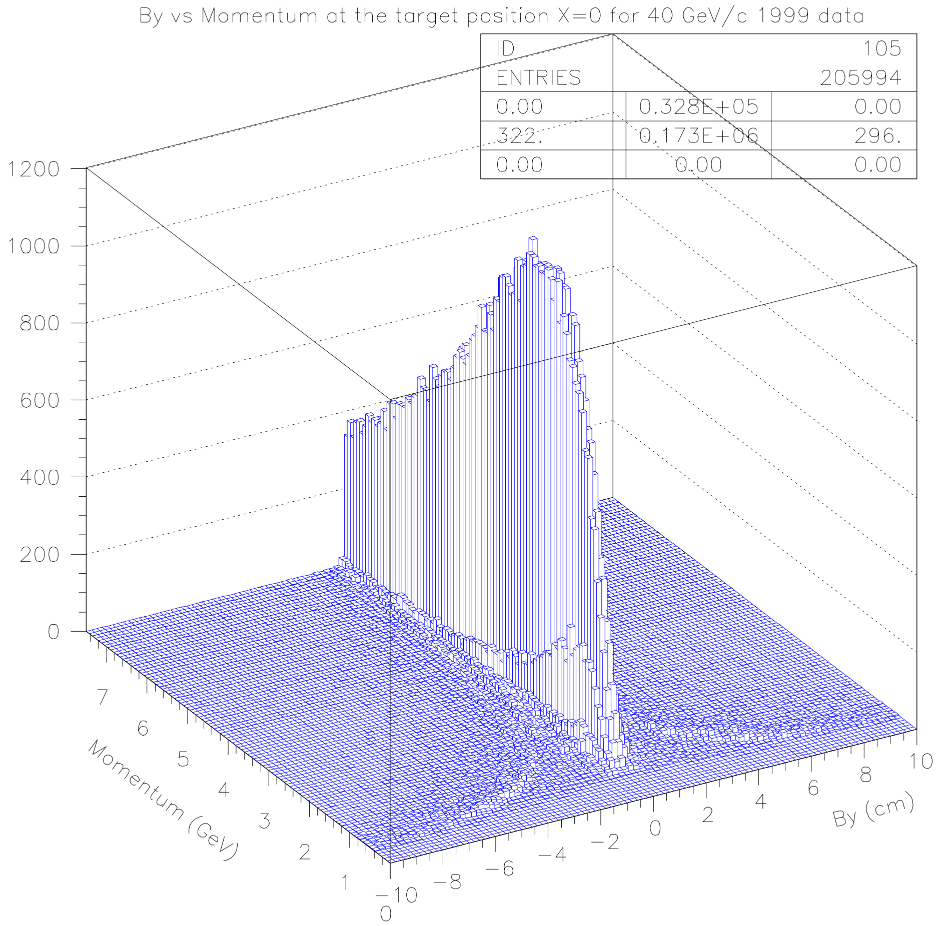

Figure 3.17: BY vs momentum at target position X=0 for the 1999 data at 40 GeV/c all charged tracks lego plot

is to find out where a track created on the first plane would trace back to. This can be done by simply tracing back tracks using the equation of a circle. The centre of the circle is at X=40cm or 60cm as this is the X position of the first plane of the telescope, Y=(R-2.5)cm and the radius is 92.5cm as calculated in Figure 3.14. These can be put into the equation of a circle and solved for X=0 to find the BY intercept. When all the numbers are put in a simple quadratic equation is left.

For the 158 GeV data the final equation is:

$$BY^2 - 180BY + 3143.75 = 0$$

And for the 40 GeV data the final equation is:

$$BY^2 - 180BY + 1143.75 = 0$$

When solved, this shows that a track created on the first plane of the telescope should trace back to a maximum BY position of approximately $\pm$19.6cm for the 158 GeV data and $\pm$6.6cm for the 40 GeV data. Figures 3.18 and 3.19 show that for the 1999 40 GeV data approximately 850 negative tracks and 780 positive tracks fall outside the projected BY position of the minimum momentum tracks, and 500 negative and 430 positive tracks do for the 1998 158 GeV data set. With between 1-3x10^6 tracks falling within these limits for either data set this adds further support that the tracks are e^+ e^- pairs.

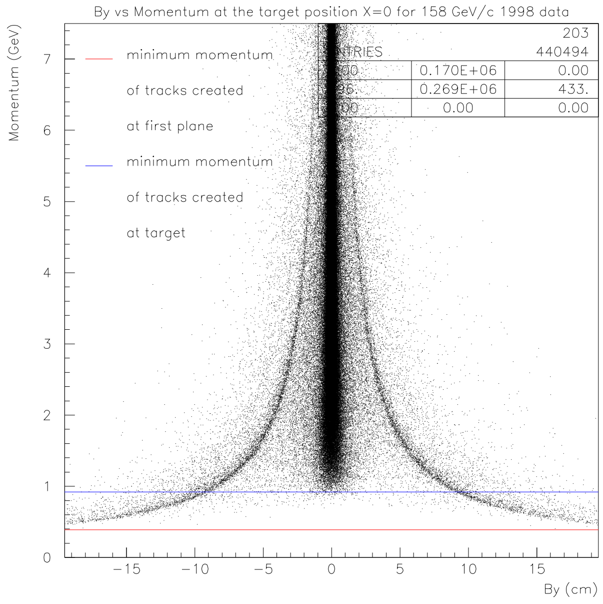

Figure 3.18: BY vs momentum at target position X=0 for the 1998 data at 158 GeV/c all charged tracks

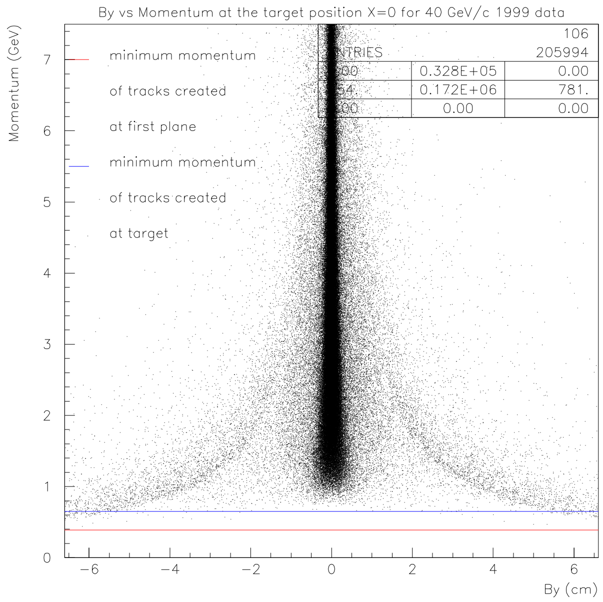

Figure 3.19: BY vs momentum at target position X=0 for the 1999 data at 40 GeV/c all charged tracks

Overall the points which fall outside the calculated BY position of the minimum momentum tracks represent less that 1% of the tracks found for 40 GeV 1999 data and less that 0.25% of those for 1998 158 GeV data. Of these tracks not all are from the *"wings"*, some are just background tracks which may be removed with other cuts. Therefore, these tracks do not represent a worry and the exercise further supports the theory that the *"wings"* are a result of π^0 decays. The tracks that do fall outside the calculated BY position of the minimum momentum tracks may do so because of reconstruction errors. The pixels that make up the telescope are of a finite size and so hits in them can be from anywhere within that pixel. This means that the reconstruction of tracks has an error associated with it. Another source of errors is the multiple scattering that can occur within the telescope and the air between the target and telescope.

3.2.4 Errors

The effect of errors can be seen more clearly in Figure 3.20 of the BY impact parameter as a function of momentum. At lower momentum there is a larger spread of points in BY than at higher momentum. This suggests that the errors in BY are momentum dependent.

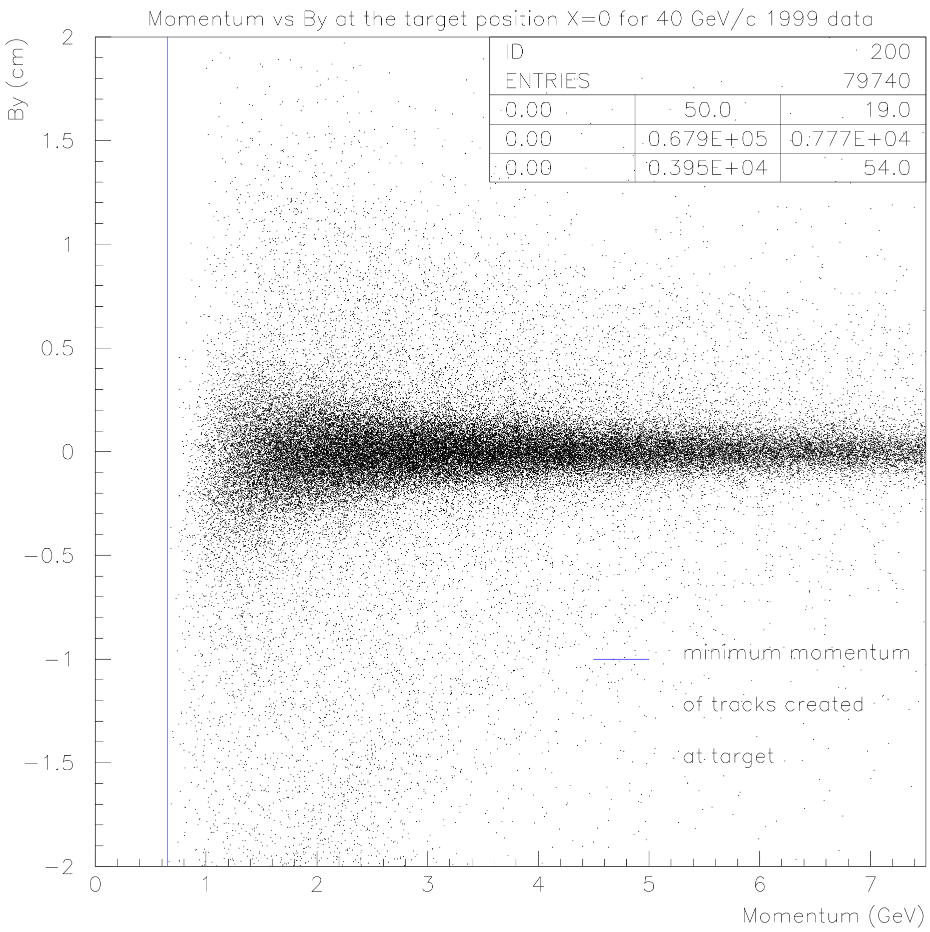

Figure 3.20: Momentum vs BY impact parameter plot for 1999 40 GeV data, negative tracks, showing spread in BY to be momentum dependent.

As stated previously the two sources of errors that will affect the BY impact parameter are the measurement error due to the finite size of the pixels and the multiple scattering error. When considering a simplified version of the telescope, that has only 3 planes, we can come up with an approximate error associated with the tracks. The path can also be approximated to a parabola, as using a circular path is considerably more complex. This leaves the setup shown in Figure 3.21.

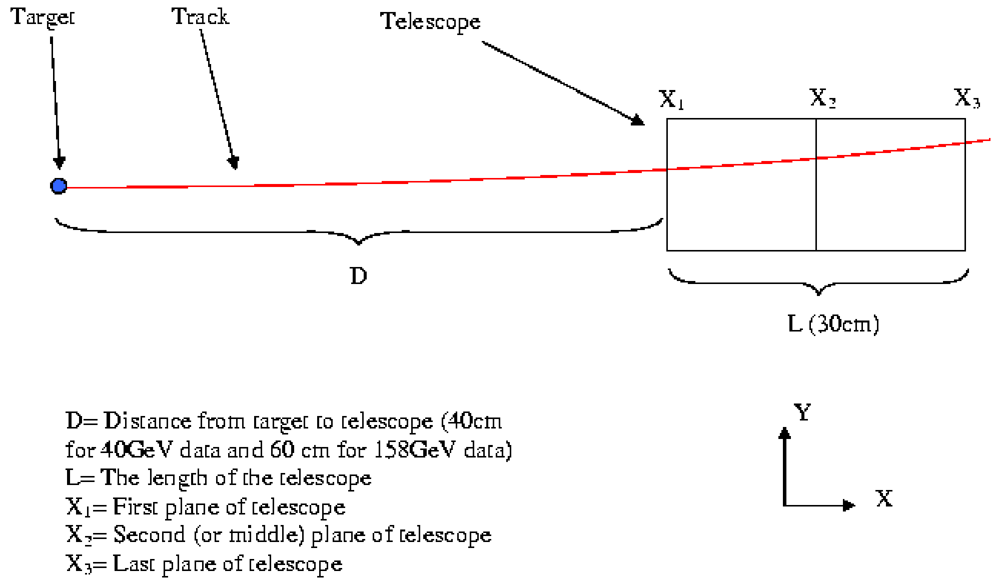

Figure 3.21: Set up of telescope and track path for error calculations

The equation for the path of the track is simply the equation of a parabola.

$$y = Ax^2 + Bx + C$$

The error required is the error in BY which is the impact parameter at the target i.e. x=0. This means that the error in C from the above equation is needed. By considering another form of the equation which is only in terms of the known coordinates we can equate terms to find C [37, 38].

$$y = y_1 \frac{(x - x_2)(x - x_3)}{(x_1 - x_2)(x_1 - x_3)} + y_2 \frac{(x - x_1)(x - x_3)}{(x_2 - x_1)(x_2 - x_3)} + y_3 \frac{(x - x_1)(x - x_2)}{(x_3 - x_1)(x_3 - x_2)}$$

$$C = \frac{y_1 x_2 x_3}{(x_1 - x_2)(x_1 - x_3)} + \frac{y_2 x_1 x_3}{(x_2 - x_1)(x_2 - x_3)} + \frac{y_3 x_1 x_2}{(x_3 - x_1)(x_3 - x_2)}$$

y_1, y_2 and y_3 are the impact points in the 1^{st}, middle and last planes of the telescope respectively, with regards to the y axis. The x points are all well defined and so can be replaced with the equation for C as follows:

$$x_1 = D, \quad x_2 = D + \tfrac{L}{2}, \quad x_3 = D + L$$

$$(x_1 - x_2) = -\frac{L}{2}, \quad (x_1 - x_3) = -L, \quad (x_2 - x_1) = \frac{L}{2},$$

$$(x_2 - x_3) = -\frac{L}{2}, \quad (x_3 - x_1) = L, \quad (x_3 - x_2) = \frac{L}{2}$$

Therefore C can be re-written as:

$$C = \frac{y_1.(D + \frac{L}{2}).(D + L)}{-\frac{L}{2}. - L} + \frac{y_2.D.(D + L)}{\frac{L}{2}. - \frac{L}{2}} + \frac{y_3.D.(D + \frac{L}{2})}{L.\frac{L}{2}}$$

for 158 GeV data:

$$\Longrightarrow C = 15y_1 - 24y_2 + 10y_3$$

for 40 GeV data:

$$\Longrightarrow C = 8.6y_1 - 12.5y_2 + 4.9y_3$$

The variance within BY is the distribution of C which is in turn the average of C^2. This is shown below for 158 GeV data:

$$\begin{aligned} < C^2 > =& 15^2 < y_1^2 > +24^2 < y_2^2 > +10^2 < y_3^2 > \\ & - 720 < y_1 y_2 > +300 < y_1 y_3 > -480 < y_2 y_3 > \end{aligned}$$

and for 40 GeV data:

$$\begin{aligned} < C^2 > \simeq& 8.6^2 < y_1^2 > +12.5^2 < y_2^2 > +4.9^2 < y_3^2 > \\ & - 213 < y_1 y_2 > +84 < y_1 y_3 > -122 < y_2 y_3 > \end{aligned}$$

The rest of this section will deal with the 158 GeV data set as the numbers are easier to work with and follow. The final results will be stated at the end for the 40 GeV data set.

Measurement Error

The measurement errors in y_1, y_2 and y_3 can all be considered the same since the OMEGA2 planes pixels are bigger and, therefore, used since these give the worst resolution. This gives a measurement error of $\varepsilon = 75\text{x}10^{-4}$ cm. The variance of the pixels is not simply their width; it is actually $\frac{\varepsilon^2}{12}$. This is shown in Appendix A. Putting this into the equation for $< C^2 >$ for the 158 GeV data set gives.

$$< C^2 >= 15^2\frac{\varepsilon^2}{12} + 24^2\frac{\varepsilon^2}{12} + 10^2\frac{\varepsilon^2}{12}$$

The measurement errors from any two planes are independent of each other and so the cross terms i.e. $< y_1 y_2 >$, can be ignored as they are zero. By putting a value of ε into this equation and calculating $< C^2 >$ it can be found that the measurement error in the 3-plane approximation is 0.0042 cm. For the 40 GeV data set this error is found to be approximately 0.0005 cm This, however, is a constant error and, by looking at Figure 3.20, it can be seen that another error is needed that is momentum dependent.

Multiple scattering

As the particle travels through the telescope it interacts with the planes and can, therefore, be scattered by them. It can also, in theory, be scattered whilst within the target itself. This means that positions y_1, y_2 and y_3 can be re-written in terms of the scattering angles from the planes in the telescope and the distance the track has travelled. These scattering angles can be represented by θ_T, θ_1, θ_2 and θ_3 for the scattering angle from the target, the first plane, the second plane and the third plane respectively. By considering the 158 GeV data set it can be seen that the distance from the target to the telescope is twice the length of the telescope and so D has been replaced by 2L for the following example of scattering error for the 158

GeV data set:

$$y_1 = 2L\,\theta_T,\;\; y_2 = (2L + \frac{L}{2})\,\theta_T + \frac{L}{2}\,\theta_1 = L\,(\frac{5}{2}\,\theta_T + \frac{1}{2}\,\theta_1);$$

$$y_3 = (2L + L)\,\theta_T + L\,\theta_1 + \frac{L}{2}\,\theta_2 = L\,(3\,\theta_T + \;\theta_1 + \frac{1}{2}\,\theta_2)$$

If the system itself is considered it can be seen that the scatterings between planes are not independent, i.e $< y_1 y_2 >$ does not equal zero. However, the scattering angles between planes are independent so terms like $< \theta_T \theta_1 >$ are equal to zero. All the values for the errors on each plane can therefore be written as:

$$< y_1^2 >= 4L^2 < \theta_T^2 >$$

$$< y_2^2 >= L^2(\frac{5}{2}\,\theta_T + \frac{1}{2}\,\theta_1)^2$$

$$= L^2(\frac{25}{4} \; < \theta_T^2 > + \frac{5}{2} \; < \theta_T\,\theta_1 > + \frac{1}{4} < \theta_1^2 >)$$

$$= L^2(\frac{25}{4} \; < \theta_T^2 > + \frac{1}{4} < \theta_1^2 >)$$

$$< y_3^2 >= L^2(9 \; < \theta_T^2 > + < \theta_1^2 > + \frac{1}{4} \; < \theta_2^2 >)$$

$$< y_1 y_2 >= L^2 5 < \; \theta_T^2 >$$

$$< y_1 y_3 >= L^2 6 < \; \theta_T^2 >$$

$$< y_2 y_3 >= L^2(\frac{15}{2} < \; \theta_T^2 > + \frac{1}{2} < \; \theta_1^2 >)$$

These can all be put back into the equation for $< C^2 >$ giving:

$$\begin{aligned} < C^2 > =& L^2[900 < \; \theta_T^2 > +3600 < \; \theta_T^2 > +900 < \; \theta_T^2 > \\ & - 3600 < \; \theta_T^2 > +1800 < \; \theta_T^2 > -3600 < \; \theta_T^2 > \\ & + 144 < \; \theta_1^2 > +100 < \; \theta_1^2 > -240 < \; \theta_1^2 > \\ & + 25 < \; \theta_2^2 >] \end{aligned}$$

The $< \theta_T^2 >$ parts all cancel out as would be expected as the target is the place of origin for the tracks and so any scattering would not affect where they trace back to. The $< \theta_1^2 >$ terms can also all be collected together into one term, however, since all the planes of the telescope are considered to be identical $< \theta_1 >=< \theta_2 >=< \theta_3 >$ etc. This means that θ_N terms, from all the planes may be grouped into one term, θ. This leaves the multiple scattering error as:

$$< C^2 >= L^2(29 < \theta^2 >)$$

and θ can be found by using the formula [6]:

$$\theta = \frac{0.016}{p\beta}\sqrt{\frac{l}{X_0}}$$

where l is the length of material the track passes through and X_0 is the radiation length of the material. The square root of the ratio of l and X_0 is found to be 0.017 [34]. β is the lorentz boost and is assumed to be 1 and p is the momentum of the particle. All the appropriate numbers can then be put in to show that the error due to multiple scattering off 3-planes is:

$$< C^2 >= \frac{0.1136}{p^2}$$

Although this is only for 3 planes, it can be calculated to 11 planes in the case of the 2000 data set, and 9 planes of the 1998 data set by considering the other planes between these 3 main planes. The scattering off these planes is then taken into account when calculating $< y_1^2 >$, $< y_2^2 >$ etc. This is shown fully in Appendix B and for 2000 data it yields the result of:

$$< C^2 >= \frac{0.305}{p^2},$$

for 1998 data is gives:

$$< C^2 >= \frac{0.232}{p^2}$$

and for 1999 data is gives:

$$< C^2 >= \frac{0.133}{p^2}$$

Overall error

The two results from the measurement error and the multiple scattering error can then be put together to determine the overall error in the impact parameter BY;

$$\Delta BY^2 =< C^2 >_{meas} + < C^2 >_{scat}$$

For the 2000 158 GeV/c data set this gives an error of:

$$\Delta BY = \sqrt{0.0042 + \frac{0.305}{p^2}},$$

the 1998 158 GeV/c data has an error of:

$$\Delta BY = \sqrt{0.0042 + \frac{0.232}{p^2}},$$

and the 1999 40 GeV/c data has an error of:

$$\Delta BY = \sqrt{0.0005 + \frac{0.133}{p^2}}.$$

Figure 3.22 shows that this error is consistent with the data although it is only an approximation. The real telescope has up to 11 planes in total, 7 of these have the resolution used for the measurement error and the other 6 have ε=50x10$^{-6}\mu$m. The measurement error calculated for 3 planes is worse than that for 11 since, by simple statistics, the more information available on the tracks position the better the path of the track can be mapped.

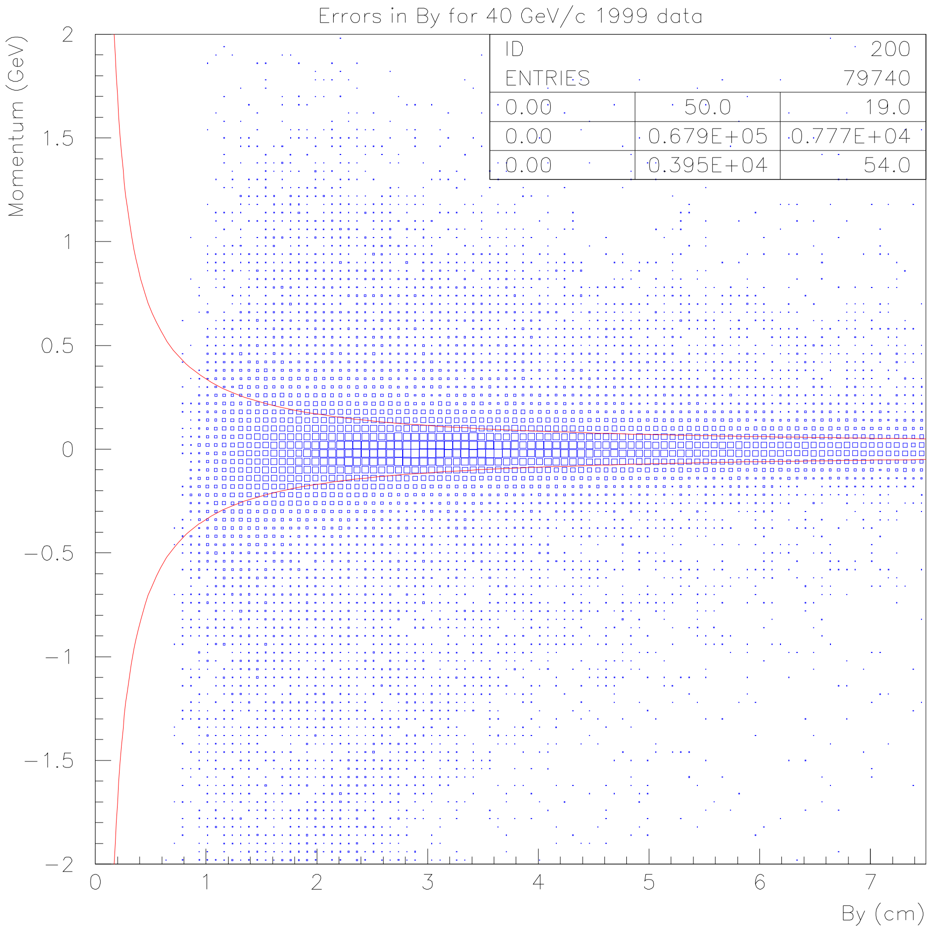

Figure 3.22: Momentum vs BY impact parameter with errors due to the measurement and the multiple scattering for the 1999 40 GeV/c data set

3.3 Monte Carlo Simulations

So far a cut has been defined in the BZ impact parameter as well as cuts removing all positive tracks. In addition, all tracks are required to pass through the first and last plane of the telescope. This requirement eliminates poorly reconstructed tracks. The definition of a BY impact parameter cut is needed together with the BZ cut to define an area on the BY-BZ plot where all tracks from the target trace back to. As stated previously, defining a BY cut will require an understanding of the e^+ e^- pairs created due to γ conversions in the first plane. This can be done by using Monte Carlo simulations generated by GEANT[39]. The purpose of the program is basically to model the behaviour of a particle. By modelling how π^0 particles behave as they come out of the target, travel through the air and then through the telescope it can be seen what effect they are having in the real data. GEANT simulates a particle such as a π^0 using information such as the lifetime of the particle and the branching fractions of its decays. They are generated over a full 4π distribution in phase space. However, some parameters can be inputted, as a range or a specific value, such as the rapidity or the transverse momentum. The program uses information about the experimental set-up as well as information on the efficiency of the planes to decide if a track will pass through the telescope and also be detected. This information is stored in a database along with a record of parameters such as the beam position for each run. This allows a record to be made about of the number of tracks GEANT generated and the number of tracks which pass through the telescope and are detected. Information such as the BY and BZ impact parameters is also recorded for the tracks which are detected in the telescope.

Tracks from Monte Carlo simulations are also used as a comparison to real data. If GEANT data can be modelled so that it matches the real data then it is likely that the simulation is what is actually going on in the process.

The output from GEANT is run through ORHION and DSTLOOK as in the case of real data. This is so that any inefficiencies with ORHION and DSTLOOK will be consistent between real and simulated data. GEANT can also be used to find the probability of one particle being detected compared to another. For example to produce 10,000 π^-s that are detected in the telescope using the 1999 40 GeV set up one needs to generate approximately 85,000 particles whereas one has to create 850,000 π^0s decaying to 2γs that interact with the telescope to generate 10,000 e$^-$s that are detected in the telescope. This shows that it is approximately 10 times more likely that a π^- is found than an electron from a $\pi^0 \longrightarrow 2\gamma \longrightarrow e^+e^-$ interaction.

Figure 3.23 shows the output for 10,000 π^0 Monte Carlo generated particles using the 1999 40 GeV set up. It clearly shows the *"wings"* created by e^+e^- pairs created on the first plane of the telescope that were described previously. However, this is not the only feature of this plot. There is still a central column of tracks that trace back to the target. This can be explained in a similar way to the wings. A γ that comes from the decay of the π^0 can interact with the planes of the telescope and instead of creating an e^+ e^- pair, it can simply knock an electron out of the atoms that make up the telescope and ionise it. These electrons will have a high momentum and will follow roughly the same path as the γ therefore they will trace back to the target. Alternatively the γ can decay straight to an e^+ e^- pair within the target or the π^0 can decay into a γ e^- e^+ in the target, in both these cases the final state electron will trace back to the target although the branching fraction for the decay to γ e^- e^+ is 1.2%[6].

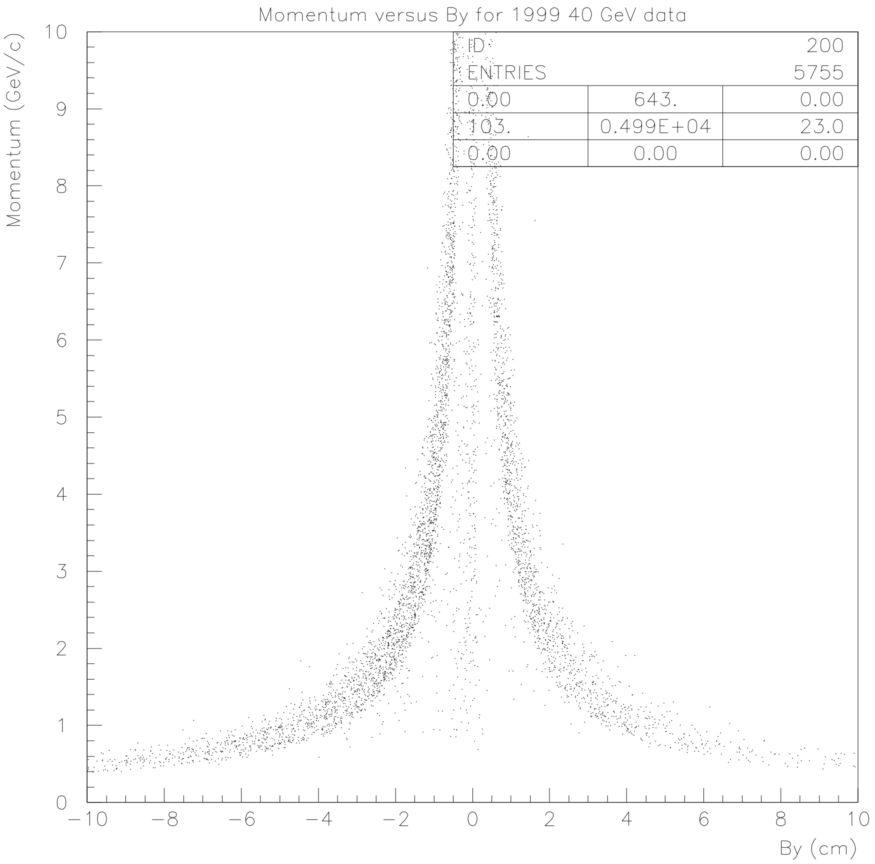

Figure 3.23: BY vs momentum for Monte Carlo π^0s generated using the 1999 40GeV set up.

In generating the π^0s which were used in Figure 3.23, and in subsequent comparisons, a condition was placed in GEANT which required a negatively charged track to be detected in the final state. This is the reason why there are more negatively charged tracks than positive tracks in Figure 3.23. A positive track is only recorded if it is in conicidence with a negatively charged track.

3.3.1 Final Selections

GEANT can be used to help define the final cut in BY along with real data. Due to the nature of the impact parameters for the e^+ e^- pairs, a momentum dependent cut in BY is the most appropriate. This cut can be made either discrete or continous. A continuous cut, similar to the error calculation shown previously, could be implemented as this would remove tracks that definitely do not come from the target. However, the calculation was only an approximation and so would need to be modified before it is used. The other alternative is to use a discrete cut at various values of momentum. This would allow the cut to be changed with much more ease and would also be defined in the same way as other cuts i.e. by eye from plots. For the purposes of consistency and for ease of use a discrete cut is better. However, this cut can then be compared to the error calculation to help justify it.

By plotting the BY impact parameter of the 10000 π^- particles produced in GEANT, with a momentum less than 2 GeV and then superimposing the same impact parameter in the same momentum range for the 10000 π^0, an idea of the best position for the first discrete cut can be found.

The π^- plot in Figure 3.24 has not been rescaled to take into account the probability

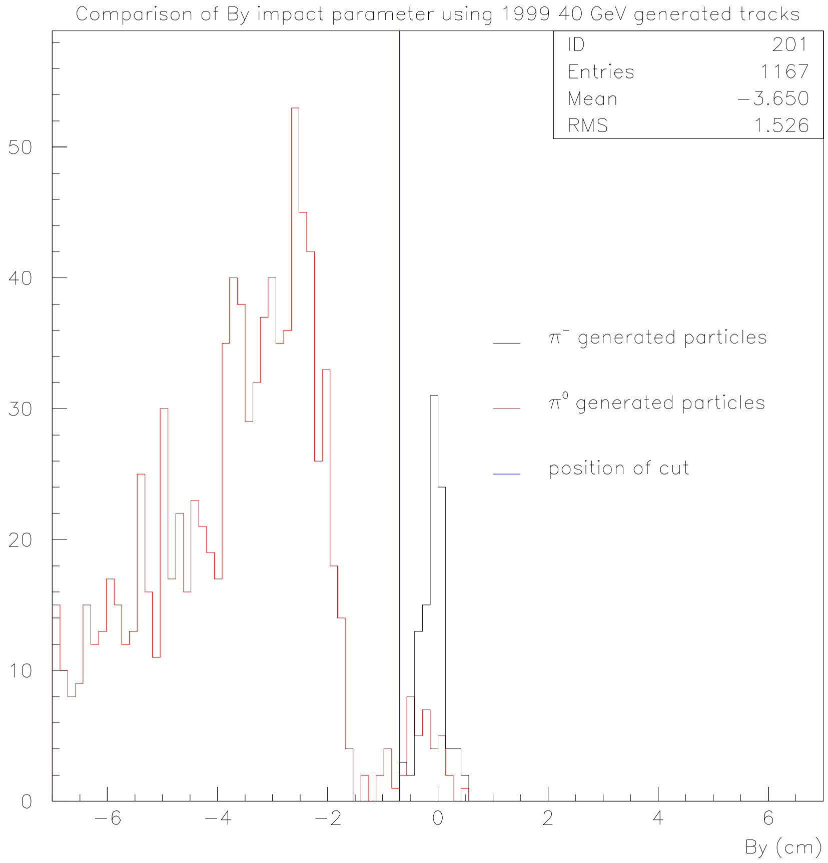

Figure 3.24: BY impact parameter cut defined by comparison of π^0 and π^- Monte Carlo data for momentum of less than 2 GeV using the 1999 40 GeV data set

of their production over the π^0s as this would make it 10 times bigger therefore, making the comparison by eye more difficult. Similar plots can be produced for various ranges of momentum to help define cuts for them as well. As momentum increases the effect of the wings becomes less and less important as the number of π^- particles dominates more and more. Figure 3.25 shows a comparison of Monte Carlo generated π^0 and π^- tracks for the BY impact parameter. All 3 plots have been rescaled, unlike Figure 3.24, to take into account the probablity of detecting the particles. The generated data used is the same as that in Figure 3.24. By using plots such as those in Figure 3.25, for both real data and Monte Carlo generated data, final discrete cuts can be defined for 3 slices of momentum in the 1999 40 GeV data and 4 slices in the 158 GeV data sets. The ratios of π^0 to π^- within the cuts for the 3 plots in Figure 3.25 are: A)3% B)1.9% C)0.5%.

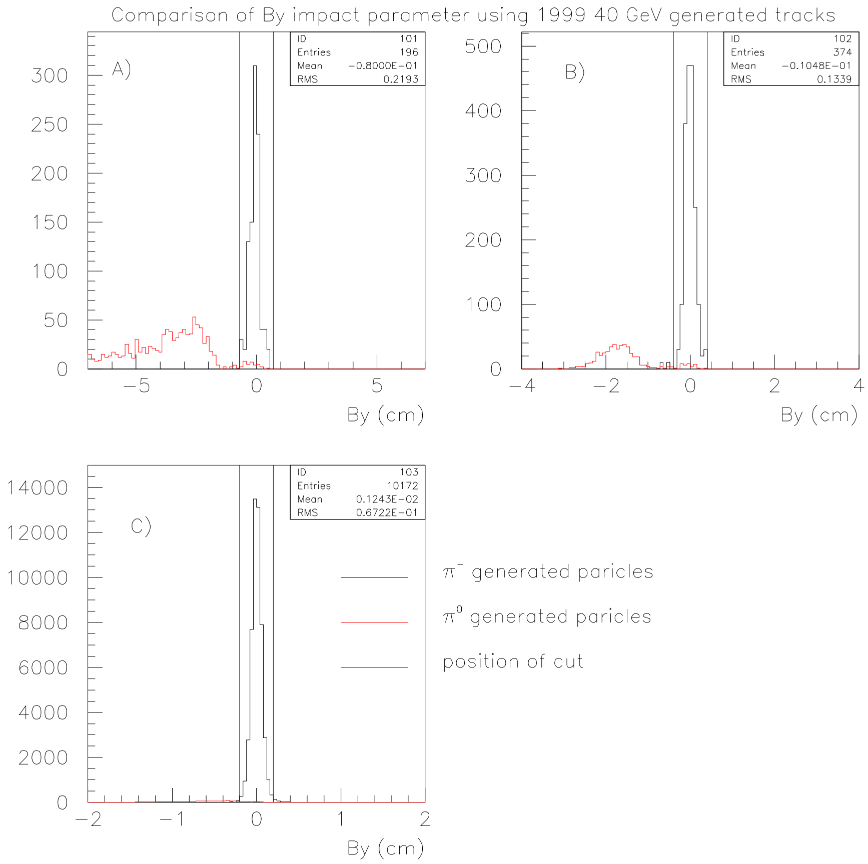

Figure 3.25: BY impact parameter cut defined by comparison of π^0 and π^- Monte Carlo data for momentum slices: A) P<2 GeV, B) 2<P<3 GeV, C) P>3 GeV, using the 1999 40 GeV data set

Table 3.2 summarises the momentum dependent BY cut for the 1999 40 GeV data set, this cut will be combined with the negative tracks, BZ and first and last planes cuts discussed previously.

Table 3.2: BY impact parameter cuts for discrete slices of momentum 1999 40 GeV data

Momentum Slice / GeV	Position of BY cut / cm
$P < 2$	0.7
$2 \leq P < 3$	0.4
$3 \leq P$	0.2

Figure 3.26 shows this discrete cut in BY compared to the calculated error to show how reasonable it is as well as being shown with real data to show it does remove the e^+ e^- pairs created on the first plane of the telescope.

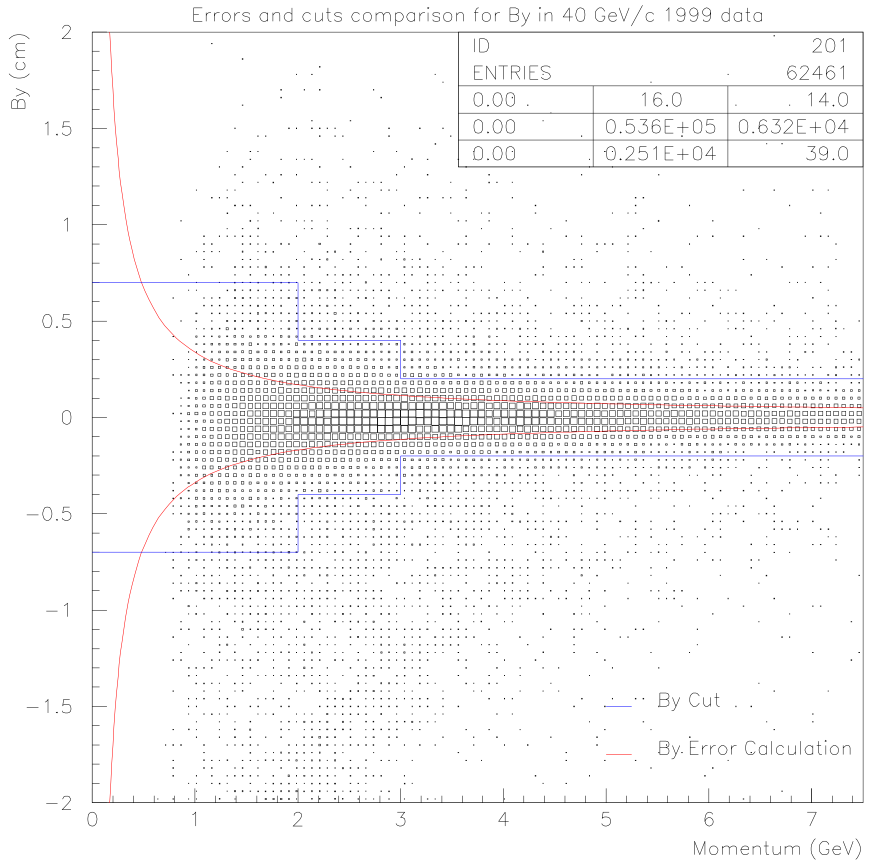

Figure 3.26: BY impact parameter cut compared to real data and to the calculated error due to measurement and multiple scattering for 1999 40 GeV data, including BZ cut, negative track cut and first and last planes cut.

Cuts for the 158 GeV data sets can be defined in the same way using the Monte Carlo generated data. As the two data sets are similar the same cuts can be defined for both. The BY cuts are defined in Table 3.3 and compared to the calculated error in Figure 3.27 for the 2000 data.

Table 3.3: BY impact parameter cuts for discrete slices of momentum 1998 and 2000 158 GeV data

Momentum Slice / GeV	Position of BY cut / cm
$P < 1$	1.2
$1 \leq P < 3$	0.9
$3 \leq P < 6$	0.45
$6 \leq P$	0.3

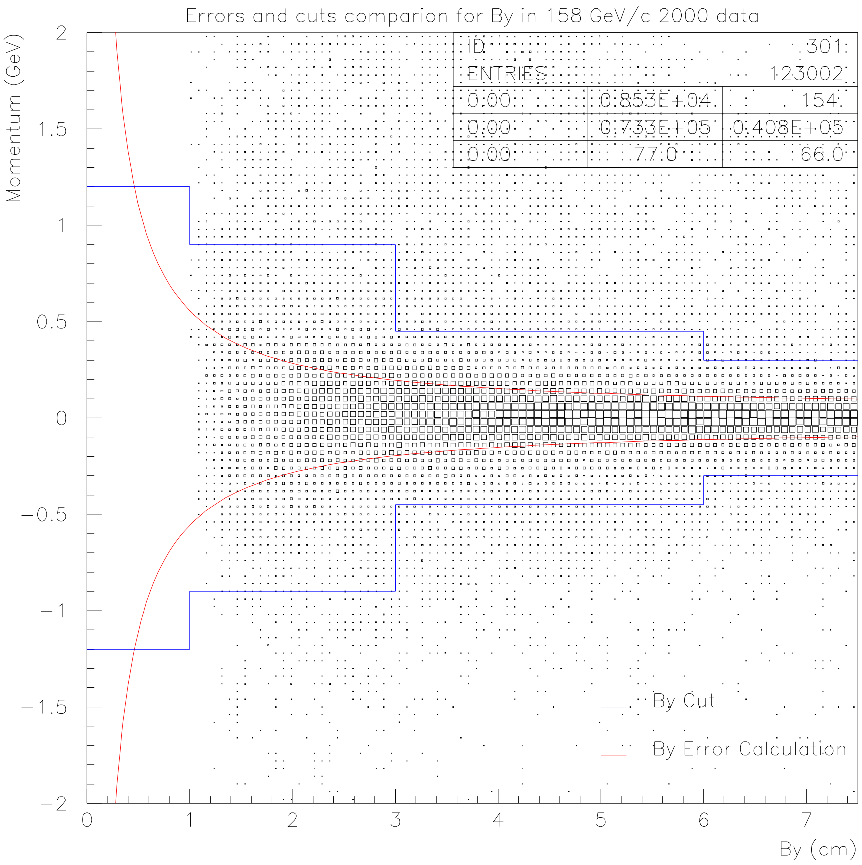

Figure 3.27: BY impact parameter cut compared to real data and to the calculated error due to measurement and multiple scattering for 2000 158 GeV data, including negative track cut and first and last planes cut.

As there was no problem with tracks coming from the end of the beam pipe in these data sets, momentum dependent BZ cuts can also be defined. To do this the BZ profile of the real data is considered. Figure 3.28 shows the BZ profile of the 1998 158 GeV data in the momentum slice 1-3 GeV.

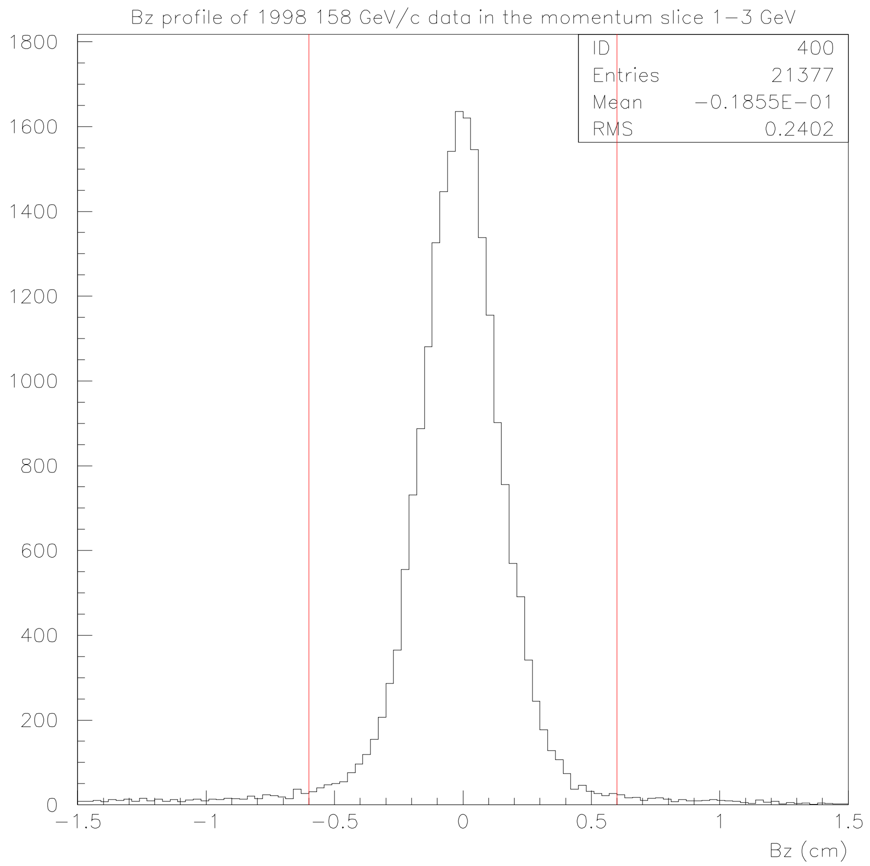

Figure 3.28: BZ profile for 1998 158 GeV/c data in the momentum slice 1-3 GeV/c. Cuts on tracks passing through first and last plane and BY cut in this momentum slice are applied and BZ cut definition is shown.

By using plots such as that shown in Figure 3.28 over, various momentum slices and using both data sets, cuts can be defined over the same four momentum slices as were used in the BY impact parameter cuts. These cuts are defined in Table 3.4 and Figure 3.29 shows the 2000 data in the momentum slice 3-6 GeV and shows that the cuts work for both data sets. Using the same cuts on both the 1998 and 2000 158 GeV data sets allows a comparison of the two to be made in later chapters. As the set-ups were comparable in the two data sets they should give similar results.

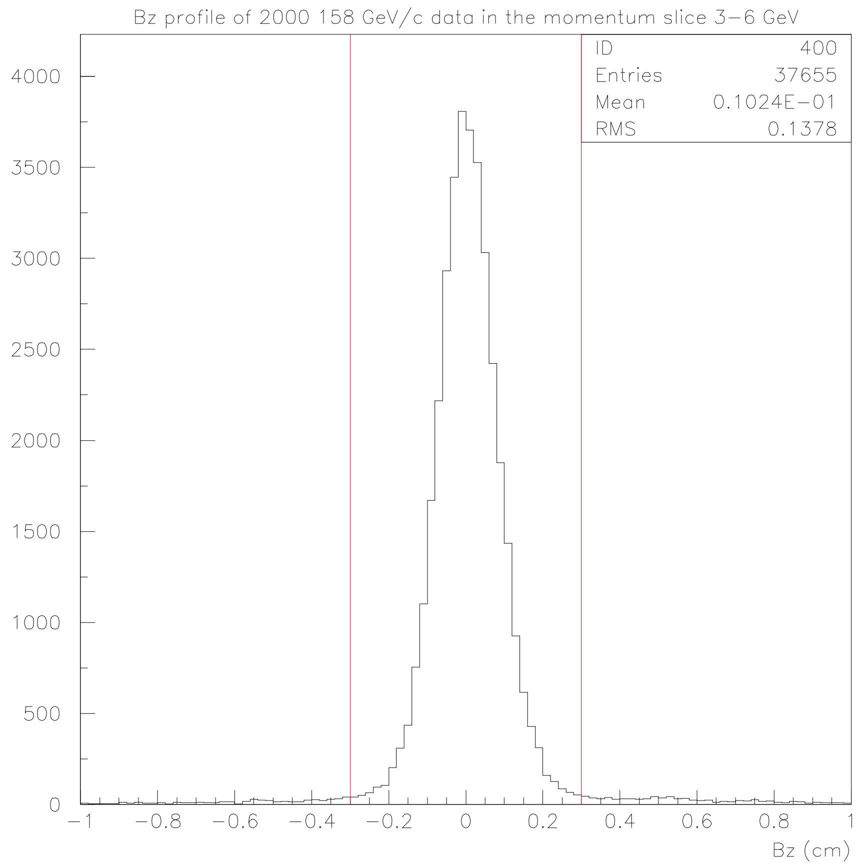

Figure 3.29: BZ profile for 2000 158 GeV/c data in the momentum slice 3-6 GeV/c. Cuts on tracks passing through first and last plane and BY cut in this momentum slice are applied and BZ cut definition is shown.

Now that cuts have been defined for both impact parameters the final task is to implement these cuts. The simple choice is to use square cuts on the data samples at the various momentum slices. However, Figures 3.1 and 3.2 show that the tracks which trace back to the target do not form a square region. Therefore, the best way to implement the impact parameter cuts is to use an elliptical cut centred on the origin.

The final cuts on the 1999 40 GeV real data are summarised in Table 3.4 below.

Table 3.4: Final cuts for 1999 40GeV data

Parameter	Cut	
plane	track must pass through first and last plane of the telescope	
charge	all tracks must be negatively charged	
BZ impact	$0.665cm$	
BY impact Elliptical	momentum dependent	
	$P < 2$ GeV	$0.7cm$
	$2 \leq P < 3$ GeV	$0.4cm$
	$3 \leq P$ GeV	$0.2cm$

The final cuts for the 1998 and 2000 158 GeV/c data sets are summarised in Table 3.5.

Table 3.5: Final cuts for 1998 and 2000 158GeV data

Parameter	Cut		
plane	track must pass through first and last plane of the telescope		
charge	all tracks must be negatively charged		
Impact Parameters	P Range	BY Cut	BZ Cut
BZ and BY:	0-1 GeV	1.2cm	1.2cm
Elliptical	1-3 GeV	0.9cm	0.6cm
	3-6 GeV	0.45cm	0.3cm
	6+ GeV	0.3cm	0.2cm

3.4 Weighting Chain

The telescope used in the NA57 does not give 4π coverage and, like all detectors, is not 100% efficient. Therefore any calculation of the number of particles produced needs to take this into account. The current method of doing this is to set up a weighting chain. First particles from the real data are selected within the cuts defined previously. This means that all selected particles are of the type being looked for, in this case negatives which are mainly pions. Information on these selected particles is then taken and used to generate tracks in a Monte Carlo simulation, GEANT. The information passed to GEANT is the rapidity and P_T of each particle as well as the run and event number of the particle so that conditions such as beam position and polarity are known. GEANT then generates tracks until 5000 are produced, with this Ylab and P_T values specified, until 5000 are found which produce the minimum number of hits in the telescope. The minimum number of hits is defined in the program and a value of 7 was used for all data set. Information on these tracks is then written to disk in a similar format to the raw data. The tracks are then mixed with background events from the experiment to create a file that is again similar to the real data. This is then passed through the ORHION program to reconstruct the tracks in the same way as was done with the real data. Finally, a program called WGTCAL is used to compare the tracks found by ORHION and those produced in GEANT and calculate the reconstruction efficency. It also looks at the number of generated tracks in GEANT (tracks that were generated but did not necessarily have enough hits in the telescope to be recorded) and calculates the weight of the particle by dividing the number of generated tracks by the number of tracks found after reconstruction. These weighted particles can then be used to calculate the number of particles per event, which is also known as the yield, and the inverse slope.

Particle distributions from the Monte Carlo data can then be compared to those from the real data as a test of the Monte Carlo generator and to highlight any inconsistencies with the real data.

3.4.1 Sampling and ffcard generation

There are over 4.5 million tracks in the 1999 40 GeV sample and upwards of 10 million tracks in the 1998 and 2000 158 GeV/c data samples which satisfy the selection criteria. Due to these high numbers it is not practical to weight every track. Therefore a sample has to be taken for weighting. It was decided to weight samples of approximately 10000 tracks which gives a statistical error of about 1% which is less than the systematic error for this analysis. For the 158 GeV data sets the samples were kept together and weighted in one sample so they could be compared after the weighting process. However, as there was only one data set at 40 GeV two separate samples were taken and weighted, this meant a comparison between them could be done at a later stage. The samples were taken by starting from the first event and checking which tracks in that event fell within the cuts defined previously. The number of tracks to be weighted, the number of events sampled (whether they contained a track within the cuts or not) and the sampling fraction are shown in Table 3.6.

Table 3.6: Number of tracks and events sampled in each data set and sampling fractions

Data Set	Sampling Fraction	Number of Events Sampled	Number of Tracks Sampled
1998	1/300	3553	11516
1999 sample 1	1/250	4644	4895
1999 sample 2	1/250	4651	4963
2000	1/300	3766	11662

The transverse momentum and rapidity in the laboratory reference frame are the main parameters taken from these tracks but the run and event number of the track is also noted as is the selection number of the event. These were then used in the filenames of each track being weighted to make it quick and easy to identify the track from the filename. A record is also kept of the overall momentum of the tracks and the multiplicity of the event from which it is selected.

The data collected from the sampling can then be used to create FFCARDS[40] to run the various pieces of software within the weighting chain. FFCARDS are like instructions given to the program telling it things like: what part of the telescope were used, what transverse momentum and rapidity to use, what database to use to determine beam positions etc.

Once all the sampling has been completed and used to create the FFCARDS the weighting chain can be run and weights can be calculated for each track processed. These can then be used to calculate the final yields and inverse slopes or the data sets. These results are shown in the following two chapters as well as the results of the R_{cp} studies although these are mainly focused on the 158 GeV 2000 data set.

Chapter 4

40 GeV/c 1999 data analysis

4.1 Real and Monte Carlo data comparisons

As stated in the previous chapter the 1999 background files were sampled into two separate data sets each comprising of just under 5000 tracks. These two samples should be statistically equivalent as they come from the same initial sample.

These two samples were run through the weighting chain and the majority of tracks completed the chain successfully in both cases. In the first sample all the tracks completed the weighting chain fully and in the second sample one track failed. This failed track was found to be on the edge of the acceptance window which is defined later in this chapter. Before this run was done an initial run was completed to check that the MC generated data within the weighting chain matched the real data from which the tracks were selected. The comparisons done were performed on the parameters used to define cuts in order to check for bad reconstruction. The cuts on the BY and BZ impact parameters are over a range and so a comparison of the spread in both these parameters between the real data and that generated is useful.

The real data used is the background files on which the sampling was performed. However the generated data is run dependent and so using one geant output is not going to be a fair comparison. Different runs have different beam positions and spreads as well as different impact positions on the target. These do vary around an average and so a sufficent number of runs will give a clear indication of the overall quality of the generated data. To do this the ntuples that are produced at the end of the weighting chain by wgtcal are all grouped together and the impact parameters are taken from this group of ntuples. The two histograms also need to be rescaled as there are many more generated tracks than real tracks, they are therefore re-scaled to the same area so as to show a representative shape for the same number of tracks.

Figure 4.1 shows the comparison for the BY impact parameter. The Monte Carlo BY impact parameter shows a good fit to the real data although the real data does appear to have a slightly better resolution than the Monte Carlo data. However Figure 4.2 shows the comparison for the BZ impact parameter which does not show a good agreement between the two data sets. The Monte Carlo data set is shifted by approximately half a millimetre in the positive Z direction. This is possibly due to the secondary interactions which were described previously in section 3.2.2 which is caused by interactions with the end of the beam pipe. A look at both the Monte Carlo and the real data without any cuts shows this more clearly and is shown in Figure 4.3.

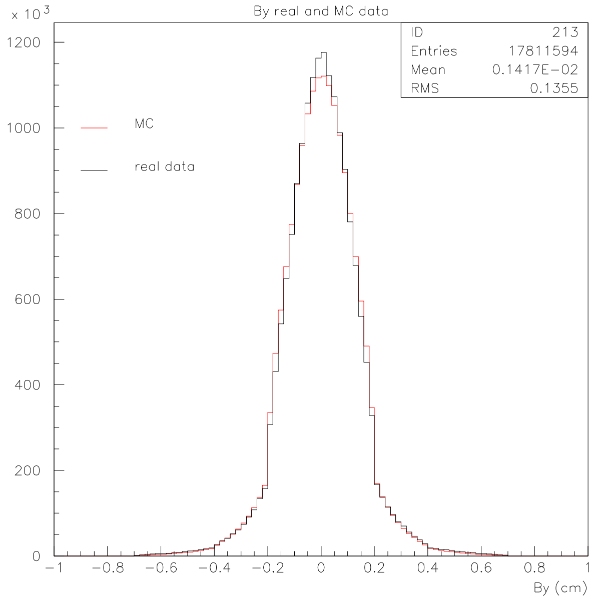

Figure 4.1: Comparison of real and monte carlo data for the impact parameter BY

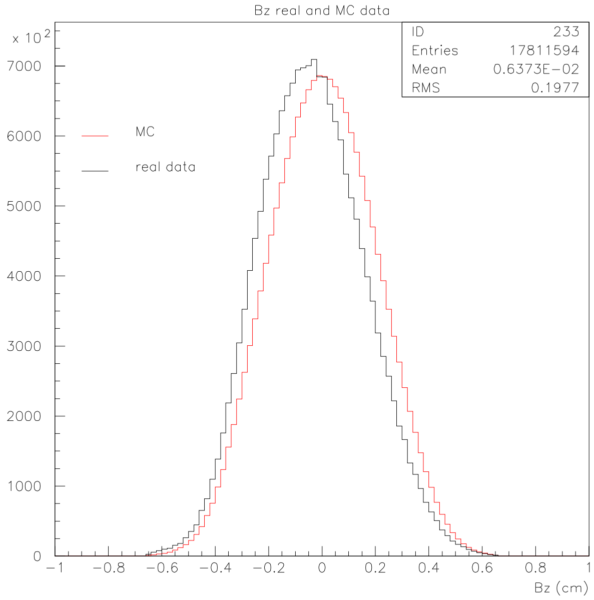

Figure 4.2: Comparison of real and monte carlo data for the impact parameter BZ

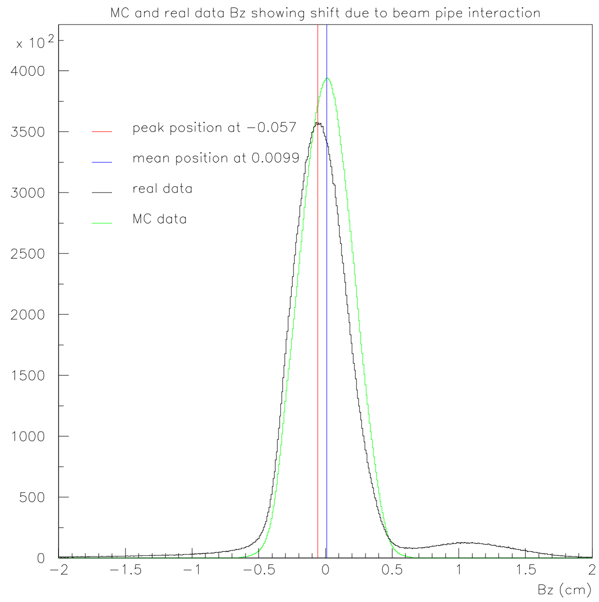

Figure 4.3: Comparison of real and monte carlo data for the impact parameter BZ with no cuts on the data sets

It does seem as if the secondary interaction is the cause of the shift between the real data and the Monte Carlo. In the data processing from the experiment the beam position was set on a run by run basis from all tracks, without BY, BZ cuts. All the tracks within a run were looked at and the average beam position was found for that run and set as the origin for that run's co-ordinate system; this position was not however the peak position and so the Monte Carlo that is produced is set to produce a peak at this incorrect position.

There are two possible solutions to this problem. Firstly the raw data can be re-processed with a cut to remove these tracks that are created by interactions at the end of the beam pipe. Secondly a shift of the primary vertex position can be put into GEANT. GEANT reads the average vertex position on a run by run basis from what is found in the real data. However, as the real data has the interaction with the end of the beam pipe included in any calculation of this value it will be shifted. Therefore shifting the value of the beam position in Z which GEANT uses will remove this shift.

The first option is a long and complicated process that is also dependent on interpretation since it is hard to just cut the tracks from the beam pipe out without removing other tracks as well. The second option is much simpler; however it requires a re-running of all the data. Therefore a test of how much the shift effects the final results needs to be done first. This can be done by taking some tracks and re-running them through the weighting chain to see how much their weight changes with the new cuts compared to the old ones. Should the change be negligible then the shift can be ignored. However if the shift is not negligible then the entire weighting chain would have to be re-run. Table 4.1 shows the original weight and the change in weight due to a shift being placed in GEANT for a sample of the tracks which have been re-weighted using these changes. Results are also shown for a shift in the positive direction and for the cut in BZ being opened up in order to investigate these effects.

Table 4.1: Comparison of the change in final weights when the BZ cut is opened up by ±0.5mm in wgtcal

Test	Original Weight	cut opened to 0.715	SHIFTG -0.05 cut 0.715	SHIFTG +0.05 cut 0.715	SHIFTG -0.05 cut 0.67	SHIFTG +0.05 cut 0.67
i	14	14	14.8	14.19	14.82	14.19
ii	15.28	15.26	14.96	14.36	14.97	14.37
iii	19.55	19.52	21.75	18.86	21.79	18.72
iv	18.76	18.76	19.07	19.13	19.07	19.18
v	16.26	16.24	16.62	16.41	16.63	16.44
vi	115.7	115.5	99.11	126.2	99.30	126.2
vii	27.58	27.43	26.05	27.14	26.21	27.30
viii	17.28	17.26	16.94	17.67	16.94	17.69
ix	23.26	23.20	22.93	22.86	23.00	22.99
x	19.19	19.16	19.8	18.50	19.84	18.53
xi	15.63	15.59	16.09	15.71	16.10	15.73
xii	1028	1027	1876	631.1	1889	632.4
xiii	20.68	20.64	21.31	20.39	21.34	20.46
xiv	1576	1450	1388	1486	1388	1486
xv	16.67	16.65	17.55	16.42	17.55	16.45
xvi	20.00	19.96	19.05	21.46	19.07	21.50
xvii	25.56	25.49	25.35	25.01	25.45	25.13
xviii	1607	1607	1339	2534	1339	2534
xix	17.06	17.03	16.37	16.72	16.40	16.75
xx	28.56	28.51	33.12	24.21	33.14	24.22
Average Weight	232.1	225.7	251.2	254.3	251.9	254.4
Percentage change	n/a	-2.8%	+8.2%	+9.6%	+8.5%	+9.6%

The change in the average weight is an increase of 8-9% when the a shift is introduced to GEANT in the negative direction. Although this shift in the average weight is dominated by the change in the higher weights it does still show a need to re-run the weighting chain. As the change is greater in the higher weights it may cause some of these weights to become less than 10 times the minimum weight, or other smaller weights to become larger than this limit. This would therefore effect the definition of the acceptance window. It would also slightly increase the sum of weights used to calcualte the yield and so distort the final yield. Therefore a complete re-run of the weighting chain must be done. The shift that is put into GEANT is -0.57mm since this is the shift of main peak in the real data from the zero position as shown in Figure 4.3.

Second Processing

Once the weighting chain has been re-run with the shift mentioned previously included in GEANT another comparison of the Monte Carlo data and the real data can be performed. Figures 4.4 and 4.5 show a much better agreement in the BZ impact parameter and a good agreement in the BY impact parameter.

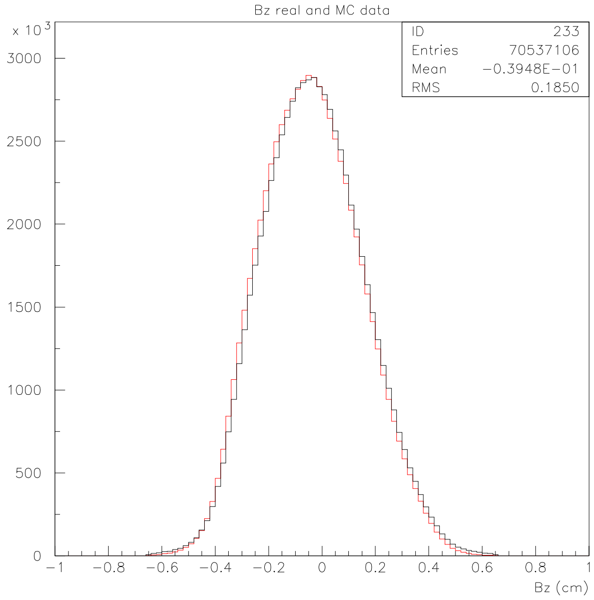

Figure 4.4: Comparison of real and Monte Carlo data for the impact parameter BZ after shift has been put into geant

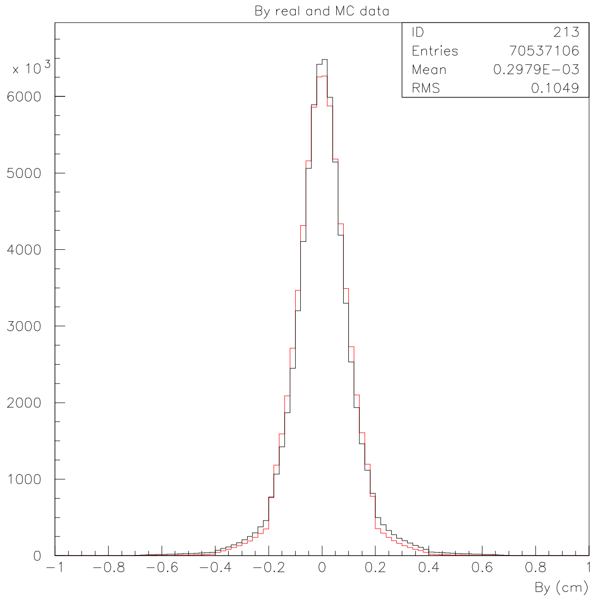

Figure 4.5: Comparison of real and Monte Carlo data for the impact parameter BY after shift has been put into geant

Now that the two samples have been run and 9857 out of the 9858 tracks have successfully completed the weighting chain the two samples can be combined and an acceptance region can be defined. This is done by considering the P_t and rapidity distributions and the number of weights that are 10 or more times greater than the minimum weight. These are defined as *high weights* and represent tracks that are detected on the edge of the telescope and so have a low acceptance.

4.2 Acceptance Region Definition

4.2.1 Transverse momentum and rapidity distribution

A plot of rapidity against transverse momentum shows a distinct shape that defines the acceptance window of the telescope. This plot is shown in Figure 4.6 for both samples combined

The high weights define the edge of the acceptance window of the telescope. This is because tracks passing close to the edge of the telescope are more likely not to pass through it fully and so are more likely to be cut. This means that GEANT has to produce a higher number of tracks to reach the 5000 good tracks that have the minimum number of hits and of those 5000 many are cut in WGTCAL as they do not pass through both the first and last plane of the telescope.

These high weights should be cut from the data sample as they correspond to points on the edges of the telescope and can bias the fit results. Therefore, a region must be defined in which we accept tracks that pass through the telescope. This region is called the acceptance window and was discussed in chapter 2.

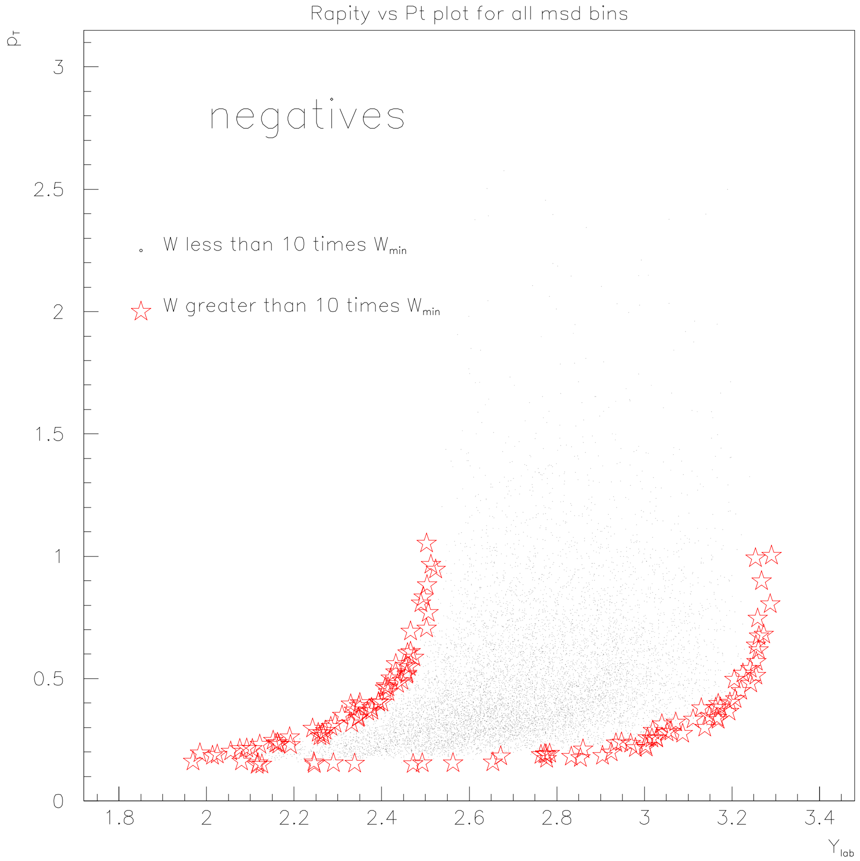

Figure 4.6: Plot of rapidity against transverse momentum with all weights that are at least 10 times larger than the minimum weight highlighted. The plot shows a distinct shape which is representative of the acceptance window of the telescope

4.2.2 Rapidity and acceptance window fitting

The minimum transverse momentum value for the window can be defined by looking at the point in Figure 4.6 where the high weights across the bottom of the acceptance region flatten off. This is approximately 0.18 GeV. The maximum value for the rapidity can also be defined in similar way by looking for the position at which the high weights stop moving across the plot. This is found to be at approximately 3.25.

The minimum value for the rapidity can be defined by the position where the smaller weights begin to mix with the larger weights. The position of this needs to be a clear cut off to stop the larger weights being inside the acceptance window. It is therefore placed at 2.35. The maximum value for the transverse momentum is defined as 2 GeV/c as this is a point above which there are only a few weights left. Its actual position, as with the other values discussed only need to cut out the larger weights and so can be moved slightly to make a reasonable size window.

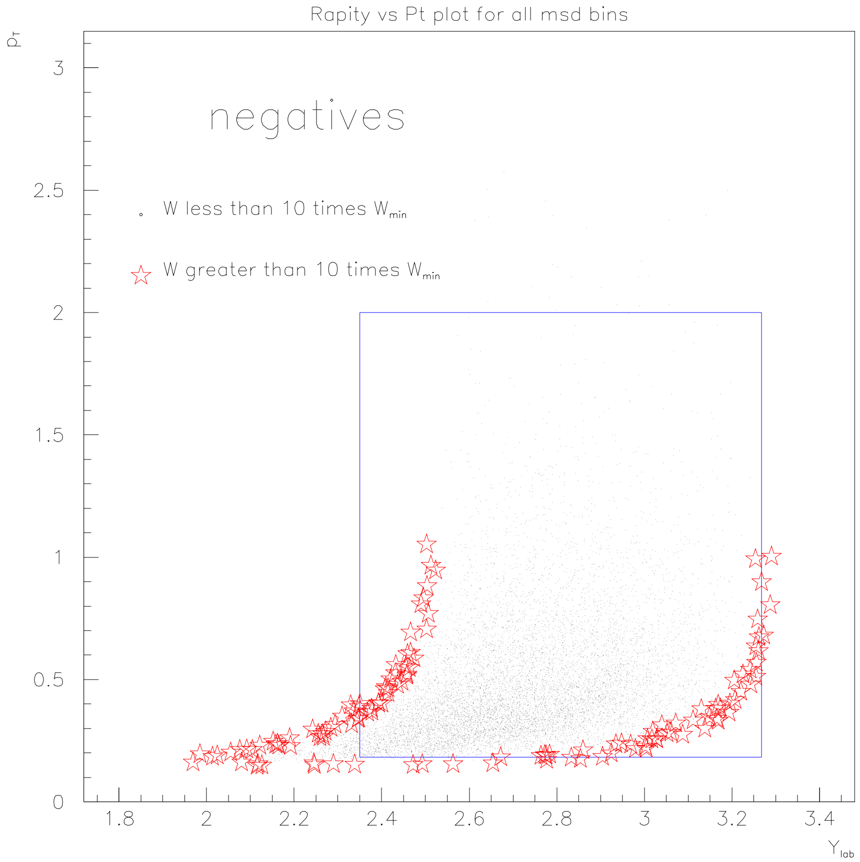

Figure 4.7: Rapidity and transverse momentum limits of the acceptance window shown with both high and small weights

This has left a square acceptance region across the plot (Figure 4.7), however it still contains many high weights and so a function is introduced to add a curve to the sides of the window. The functions used to define these curves were defined in section 2.3.2 and will produce a window similar to that shown in Figure 2.3

However these functions are terms of transverse mass, M_t, and so must be turned into the P_t form by using the formula below, where $F(Y)$ is the original function in terms of M_t and F‘(Y) is the corrected function in terms of P_t.

$$F`(Y) = \sqrt{(F(Y)^2 - M_\pi^2)}$$

In converting to transverse momentum the mass of the pion is used as the pion is assumed to be the main particle being looked for here and it was the pion used to generate the Monte Carlo data by GEANT. The variable M^* is found to be arbitary. This is because the formula is only exact in the case of no magnetic field being present. In the presence of a magnetic field, especially for low P_T, it has to be modified so that M^* is a free parameter. The value used for M^* was 0.21 and was found by a trial and error method. By another trial and error method the two angles for the curves are found to be 0.076 and 0.155. All the parameters are shown in Table 4.2

Table 4.2: Acceptance window parameter definitions

Parameter	value
P_t minimum	0.182
P_t maximum	2.0
Y_{lab} minimum	2.35
Y_{lab} maximum	3.2679
θ	0.076
ψ	0.155

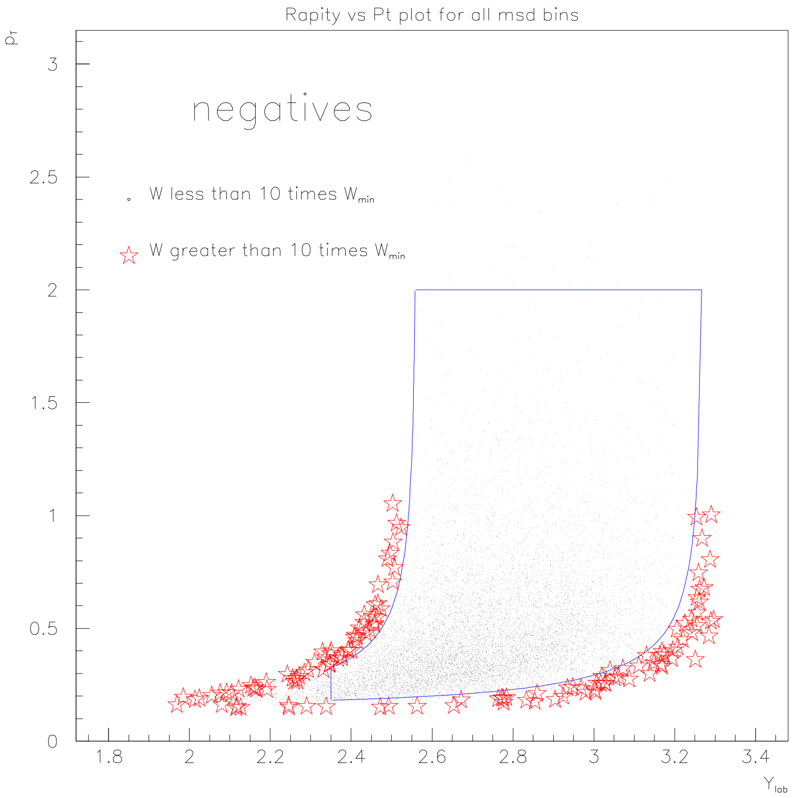

Figure 4.8: Rapidity and transverse momentum with the acceptance window shown with both high and small weights

Although the parameters of the window have been chosen to make it as large as possible without including any high weights, whilst also keeping its upper limit in transverse momentum to a reasonable value, the parameters themselves must not change the final value of the yield. Therefore once the value of the yield has been calculated it must be shown to be stable within the acceptance region. However, the first thing to consider is the inverse slope and to calculate this the fitting program described in section 3.4.2 is used.

In the analysis of strange particles such as Λ, Ξ^- and Ω it is assumed that the the rapidity distribution is flat. However, in negative particle analysis this is not the case. As you move to higher and higher rapidity the number of particle decreases (with particle weights taken into account as well), therefore this needs to be reflected in the fitting program by fitting a Gaussian to the rapidity distribution $f(y)$, described in section 3.4.2. The fitting program can be used to do this by leaving the sigma value of the gaussian as a free parameter and fixing the mean of the gaussian to 2.22 which is the centre of the rapidity distribution for 40 GeV/c collisions. The results of the two samples and the combined sample is shown in Table 4.3 and a plot of the rapidity distribution and the fit for the combined results is shown in Figure 4.9.

Table 4.3: σ values for the Gaussian fit of the rapidity distribution

Sample (event sampled)	MSD range	σ
Sample 1 (4358)	Full	0.749 ± 0.007
Sample 1 (239)	5% most central	0.779 ± 0.019
Sample 2 (4376)	Full	0.813 ± 0.008
Sample 2 (223)	5% most central	0.787 ± 0.020
Combined Samples (8734)	Full	0.779 ± 0.005
Combined Samples (462)	5% most central	0.782 ± 0.014

The fitting program can also be used to determine the extrapolation factor which was also described previously. A yield without background correction can then be determined. The inverse slopes, extrapolation factor and non background corrected yields are shown in Table 4.4

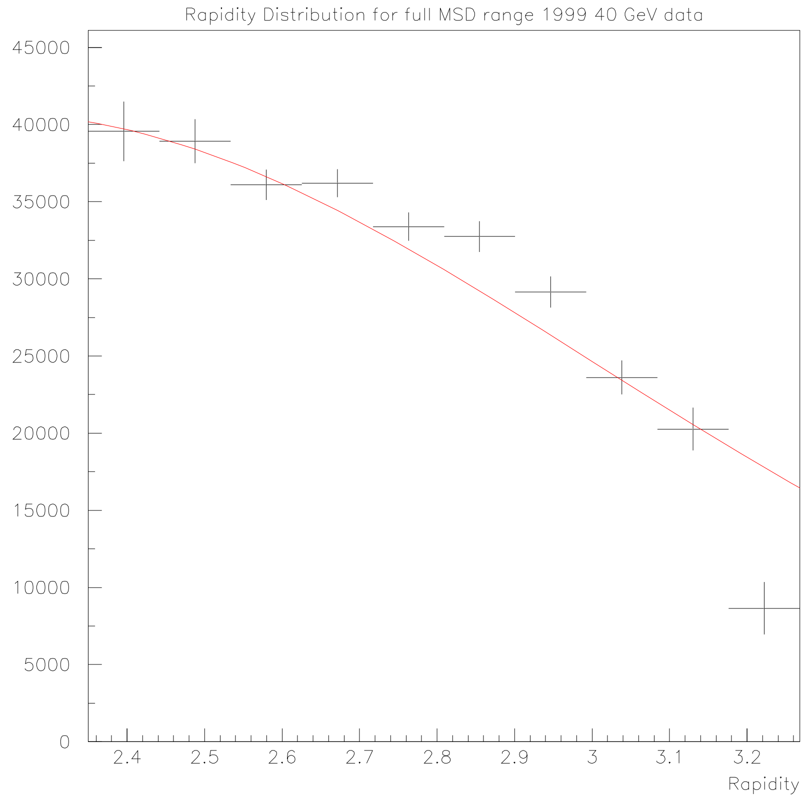

Figure 4.9: Rapidity Distribution and Gaussian fit for 1999 40 GeV weighted data, combined samples

4.3 Yield Corrections and Acceptance Window Tests

4.3.1 Background correction

As stated previously the background correction is calculated in two parts. The number of events sampled needs to be corrected as some background events may have been sampled when an event was triggered upon when there was no interaction with the target. The sum of weights also needs correcting as some sampled and weighted tracks may have been background tracks. This correction is achieved by using the empty target runs as described in section 3.4.2 and gives a percentage of

Table 4.4: Inverse slope, extrapolation factors and uncorrected yields of the individual samples and combined samples with free σ shown in Table 4.5

Sample	MSD range	Extrapolation factor	Inverse slope (MeV)	Uncorrected yield
Sample 1	Full	2.45	188.2 $\pm$2.4	48.4 $\pm$0.8
Sample 1	5% most central	2.45	181.9 $\pm$5.9	132.9 $\pm$5.5
Sample 2	Full	2.40	184.5 $\pm$2.3	49.0 $\pm$0.8
Sample 2	5% most central	2.39	191.7 $\pm$6.5	128.4 $\pm$5.6
Combined Samples	Full	2.43	186.3 $\pm$1.7	48.7 $\pm$0.6
Combined Samples	5% most central	2.42	186.7 $\pm$4.4	130.7 $\pm$3.9

tracks and events that may be in the sample. The background correction factor is found to be;

$$\text{Background Correction} \; = \frac{N_{samp}\text{ Correction}}{\sum \text{ Weights Correction}}$$

And so the final yield can be expressed as;

$$Yield = \frac{\sum \text{ Weights}}{N_{samp}} \times \text{ Extrapolation factor } \times \frac{N_{samp}\text{ Correction}}{\sum \text{ Weights Correction}}$$

Where N_{samp} is the number of events sampled

The correction factors found for each centrality class and the full centrality range are shown in Table 4.5.

These correction factors can now be combined with the extrapolation factors in Table 4.4 to calculate the final yields with a free σ. The σ value is calculated by a standard fitting program used by the NA57 collaboration and is determined using the maximum likelihood method. These final yields are given in Table 4.6. The Classes 0-4 shown in Table 4.5 are difference slices in the multiplicity range, they

Table 4.5: Background correction factors for all centrality classes

Centrality class	Correction to sum of weights	Correction to Number of events sampled	Overall Correction
Class 0	3.2%	32%	1.424
Class 1	0.25%	8.5%	1.090
Class 2	0.001%	0.5%	1.005
Class 3	0%	0.08%	1.0008
Class 4 (5% most central)	0%	0.04%	1.0004
Full	0.3%	13%	1.146

represent various degrees of centrality of collision. The percentage of the centrality is also given, upto the maximum 56% central collision

Table 4.6: Final yields of the individual samples and combined samples with free σ shown in Table 4.3

Sample (events)	MSD range	Final yield
Sample 1 (4358)	Full	54.3 $\pm$0.9
Sample 1 (239)	5% most central	133 $\pm$5.5
Sample 2 (4376)	Full	56.0 $\pm$0.9
Sample 2 (223)	5% most central	128 $\pm$5.6
Combined Samples (8734)	Full	55.7 $\pm$0.6
Combined Samples (462)	5% most central	131 $\pm$3.9

4.3.2 Fixing σ for Rapidity

Although these yields and slopes are the final results, checks must be carried out in order to make sure the choice of the window does not bias the results. The extrapolation factor should balance out any changes to the window and, therefore, keep the yield consistent. However, the σ value found is also variable and so when looking at the slopes and yields over a small rapidity region its effect can be large. Therefore, by fixing a σ value which is determined over the full rapidity range of the window stability tests can be done.

From Table 4.3, a value of 0.8 can be used for σ in a fixed Gaussian.

4.3.3 Acceptance Window Stability

The first test in the stability of the window is to look at how the values of the slope and the yield change if its size is decreased, the changes should be very small and within errors of each other. Any larger variation will indicate a systematic error in the method.

Two new windows were defined using the parameters shown in Table 4.7. Both windows are smaller than the original window, this is because any larger windows would take in the larger weights which would bias the results.

The three windows are all shown with the weights (both large and small) in Figure 4.10.

The yields, with background corrections, and inverse slopes for the two new windows, as well as the original window are summarised in Table 4.8. For the fitting

Table 4.7: Acceptance window parameter definitions for the two smaller windows as well as the original window

Parameter	Original Window	Window 2	Window 3
P_t minimum	0.182	0.3	0.35
P_t maximum	2.0	1.9	1.8
Y_{lab} minimum	2.35	2.45	2.55
Y_{lab} maximum	3.2679	3.215	3.15
θ	0.076	0.08	0.085
ψ	0.155	0.145	0.135

of the other two windows, the rapidity distribution was fitted with a mean of 2.22 (the centre of the rapidity distribution for the 40 GeV data set) and σ of 0.8 and the combined sample of data was used to get the greatest statistical accuracy.

Table 4.8: Inverse slopes and corrected yields for the 3 acceptance windows defined using parameters in Table 4.9 using the combined data samples

Window	MSD range	slope	yield
Full window	Full	185.9 $\pm$1.6	55.3 $\pm$0.6
Full window	5% most central	186.3 $\pm$4.1	129.9 $\pm$3.9
Window 2	Full	186.4 $\pm$1.9	57.3 $\pm$0.7
Window 2	5% most central	189.3 $\pm$5.0	134.8 $\pm$4.5
Window 3	Full	187.9 $\pm$2.3	56.5 $\pm$0.8
Window 3	5% most central	195.4 $\pm$6.3	131.0 $\pm$5.1

The fact that the two new windows are inside the original window does mean that the results are likely to be fairly similar as they are using mainly the same data. However, the results of the smaller windows will highlight any edge effects we have

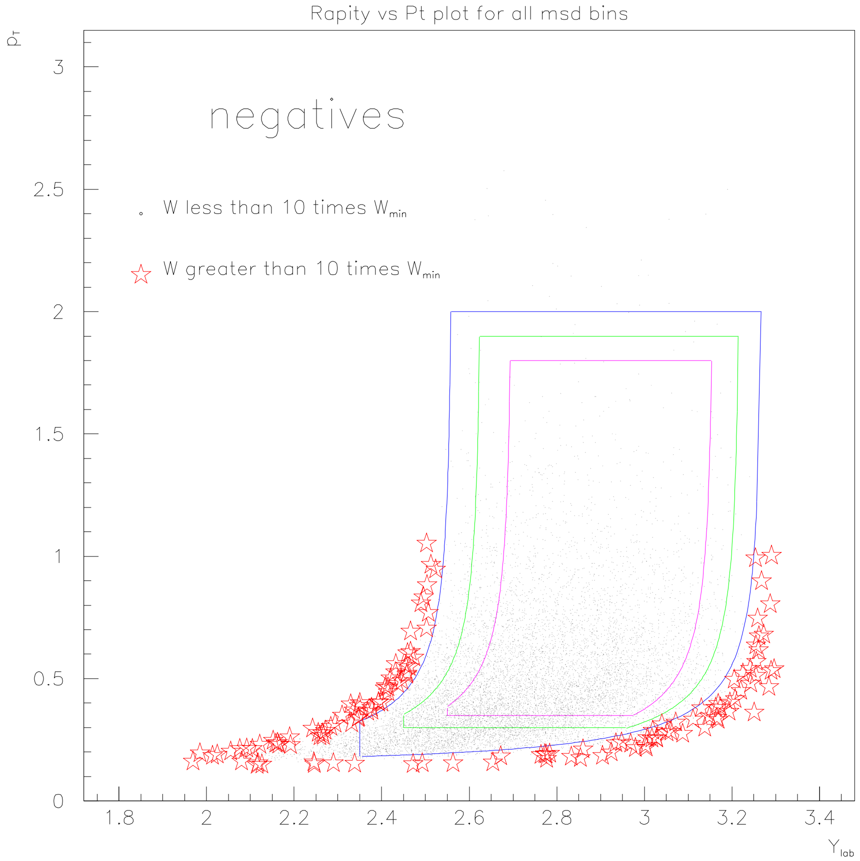

Figure 4.10: Three different sized windows used to investigate the stability of the acceptance window

present that are caused by the edges of the telescope. The removal of the high weights should mean these effects are not present; this test should confirm this.

For the full sample the yields and slopes do not vary much as the window is decreased in size. The most central collisions do show an increase in the slope as the window gets smaller, however this is still within the statistical errors. This combined with the fact that the statistics get lower for the smaller windows, especially in the 5% most central collisions, means that the variation in slope is not worrying. The most central yields help back this up as they do not vary much as the window decreases in size. It is the stability of the yields which is most important as producing a final yield is the main aim of this thesis.

The second check on the window stability is to check how the yields and slopes vary across the window. The simplest way of doing this is to take the window and divide it up into four slices. This will show if the fit to rapidity is accurate and it may show up any other problems within the weighting chain that have so far not been discovered.

A summary of the four windows is shown in Table 4.9 and a plot showing all 4 slices within the original window is shown in Figure 4.11

Table 4.9: Parameter definitions for slices of the acceptance window used in 40 GeV data set.

Parameter	Original Window	slice 1	slice 2	slice 3	slice 4
P_t minimum	0.182	0.182	0.182	0.182	0.182
P_t maximum	2.0	2.0	2.0	2.0	2.0
Y_{lab} minimum	2.35	2.35	2.35	2.35	2.35
Y_{lab} maximum	3.2679	2.6942	2.854	3.0463	3.2679
θ	0.076	0.135	0.115	0.095	0.076
ψ	0.155	0.155	0.135	0.115	0.095

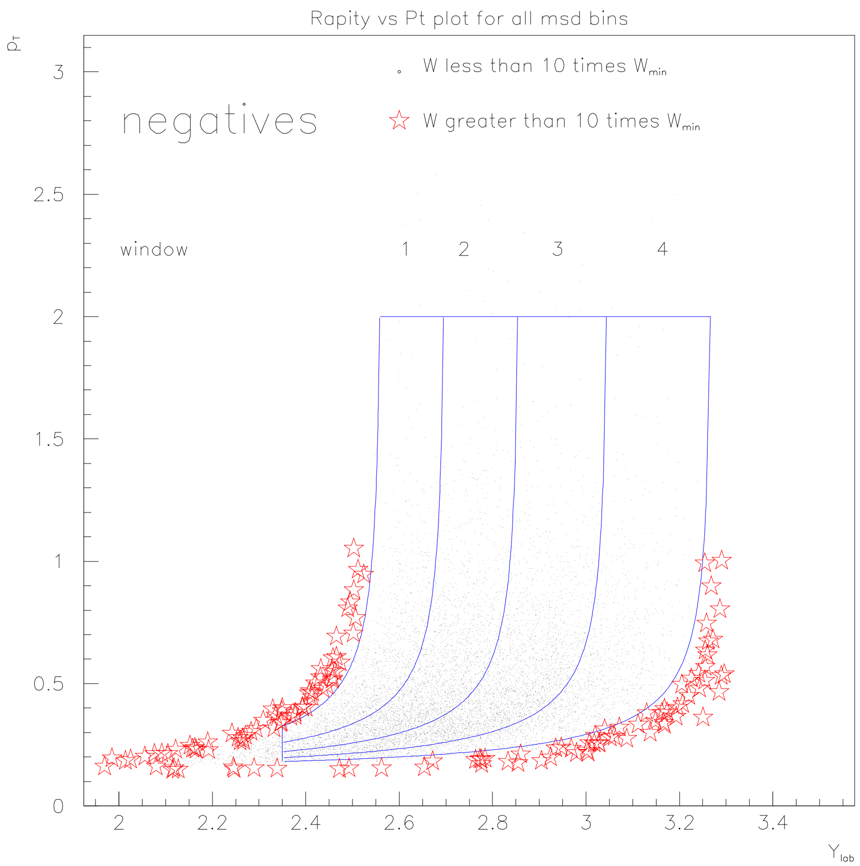

Figure 4.11: Different slices of the main acceptance window used to investigate the stability of the window

As with the windows within the final acceptance window, each of the slices has been analysed using a fixed σ and mean for the gaussian fit. The results for the inverse slope and the final yields of the 4 slices are summarised in Table 4.10 for the full MSD statistics and Table 4.11 for the 5% most central statistics.

The variation around the value of the original window is shown more clearly in plots 4.12-4.15

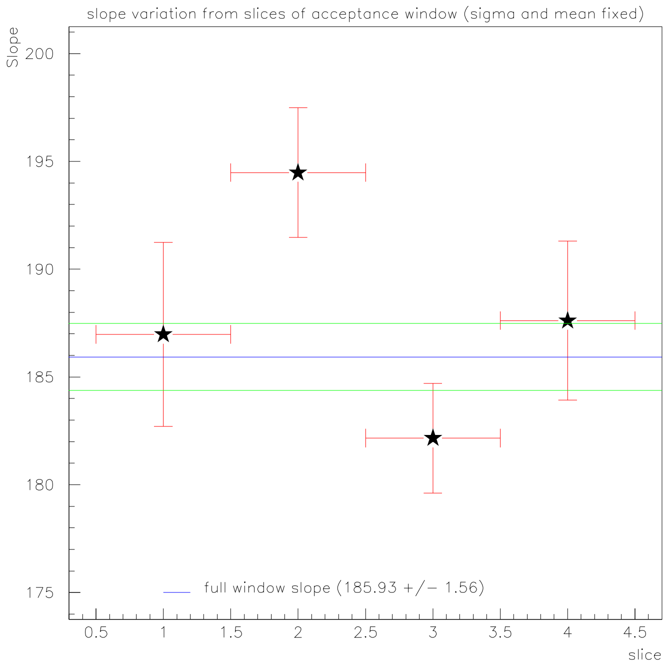

Figure 4.12: Variation in slope through the different slices of the main acceptance window with full MSD statistics

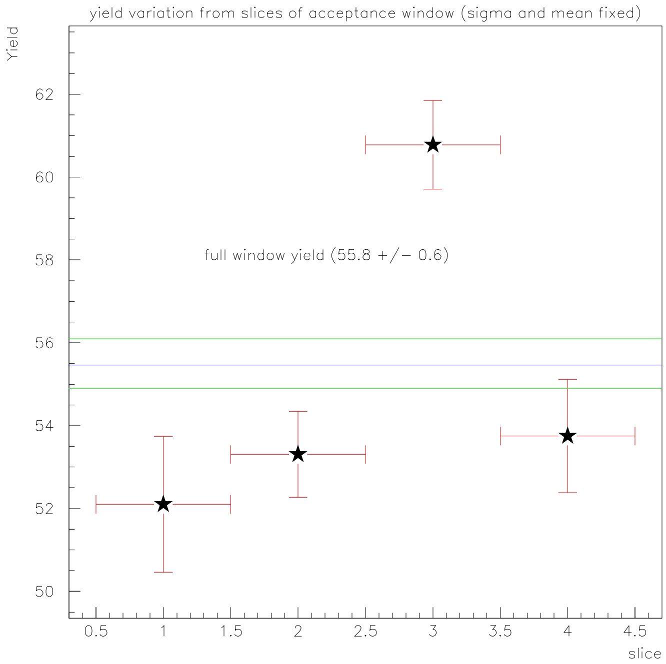

Figure 4.13: Variation in yield through the different slices of the main acceptance window with full MSD statistics

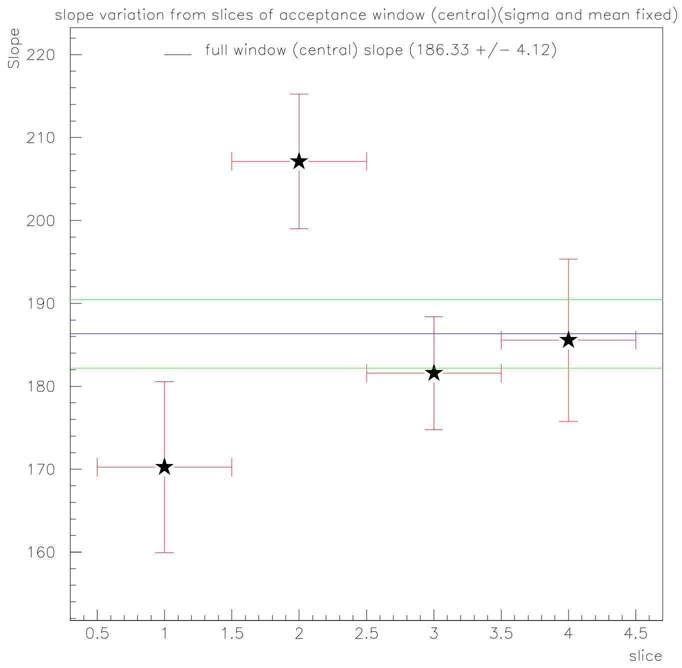

Figure 4.14: Variation in slope through the different slices of the main acceptance window with 5% most central MSD statistics

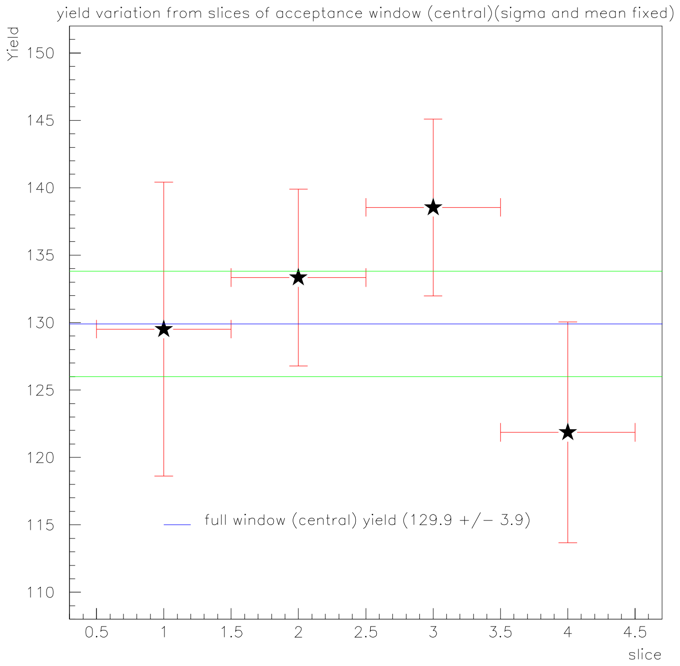

Figure 4.15: Variation in yield through the different slices of the main acceptance window with 5% most central MSD statistics

Table 4.10: Full MSD results of the slices of the acceptance window

Slice	Inverse Slope	Yield
Original Window	185.9 $\pm$1.6	55.4 $\pm$0.6
1	187.0 $\pm$ 4.3	52.1 $\pm$ 1.6
2	194.5 $\pm$ 3.0	53.3 $\pm$ 1.0
3	182.2 $\pm$ 2.5	60.8 $\pm$ 1.0
4	187.6 $\pm$ 3.7	53.8 $\pm$ 1.4

Table 4.11: 5% most central results of the slices of the acceptance window

Slice	Inverse Slope	Yield
Original Window	186.3 $\pm$4.1	129.9 $\pm$3.9
1	170 $\pm$ 10	129.5 $\pm$ 10.9
2	207 $\pm$ 8	133.3 $\pm$ 6.6
3	182 $\pm$ 7	138.5 $\pm$ 6.6
4	186 $\pm$ 10	121.9 $\pm$ 8.2

The variation of the yield in the full sample is the only value which does not vary closely around the value of the full window. In the third slice the yield is higher than the full window value by approximatley 4σ. However this variation is not a worry as the other points sit close to but below the overall average. To show that the Gaussian fit to the rapidity is a fair approximation the rapidity fit to this third slice is shown in Figure 4.16 and shows a good fit.

Overall the test shows no problems with the windows, the yields and slopes do not increase or decrease as you move across the window, they have a variation that does not highlight any problems across the rapidity region therefore giving confi-

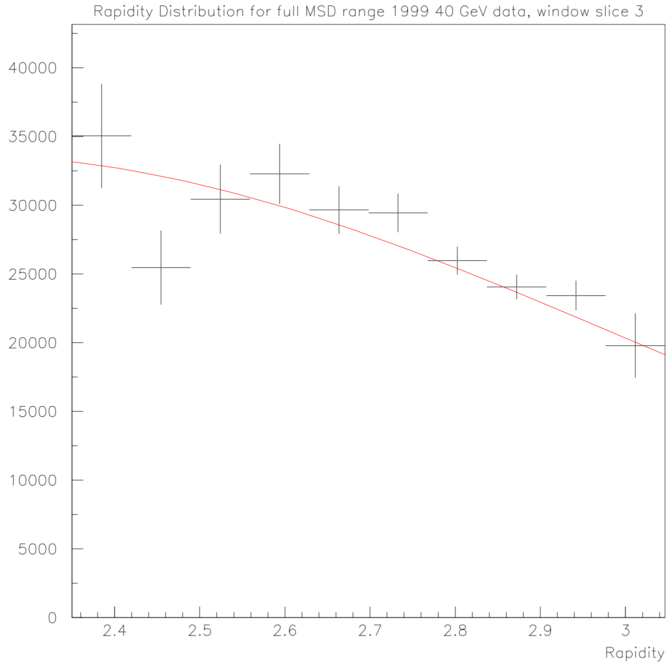

Figure 4.16: Rapidity distribution for the 3^{rd} slice of the acceptance window, as defined in Table 4.9

dence in the methods used and showing that the yields and slopes are stable within the window.

4.4 Final Inverse Slope and Yields

Now that all checks have been made and the all stages have been run, the final yields and inverse slopes for all MSD classes can be calculated. The various MSD classes define different degrees of centrality within the collision. Both the final yields and slopes, as well as the definition of the centrality classes, are given in Table 4.12. The quality of the fit for the inverse slope is shown in Figure 4.17

The centrality class definitions are used within the NA57 collaboration for several

Table 4.12: Final Inverse Slopes and Yields

MSD class	Centrality	number of events sampled	sigma of rapidity	Inverse Slope	Yield
full	full	8734	0.779 ± 0.005	186.3 ± 1.7	55.78 ± 0.64
0	42-56%	2975	0.746 ± 0.015	186.1 ± 5.7	18.97 ± 0.71
1	25-42%	2647	0.876 ± 0.014	185.1 ± 3.4	39.62 ± 0.94
2	12-25%	1742	0.759 ± 0.009	184.7 ± 3.0	77.55 ± 1.59
3	5-12%	908	0.735 ± 0.009	188.4 ± 3.4	116.44 ± 2.71
4	0-5%	462	0.782 ± 0.014	186.7 ± 4.4	130.74 ± 3.93

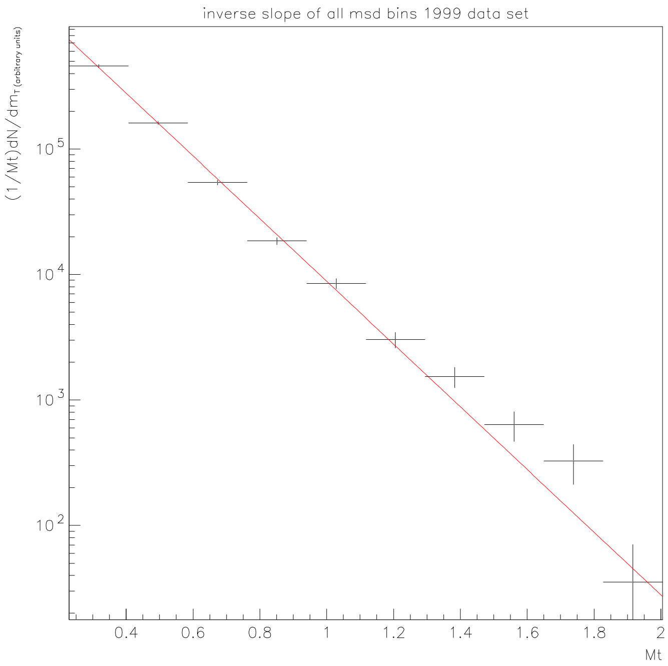

Figure 4.17: $ln\left(\frac{1}{m_T}\frac{dN}{dm_T}\right)$ versus m_T for the 1999 data set. The fitted line was obtained using a maximum likelihood fit.

other pieces of analysis and so were predefined before this analysis.

A look at how the slope and yield vary with multiplicity gives an idea of the effect of the centrality of the collision.

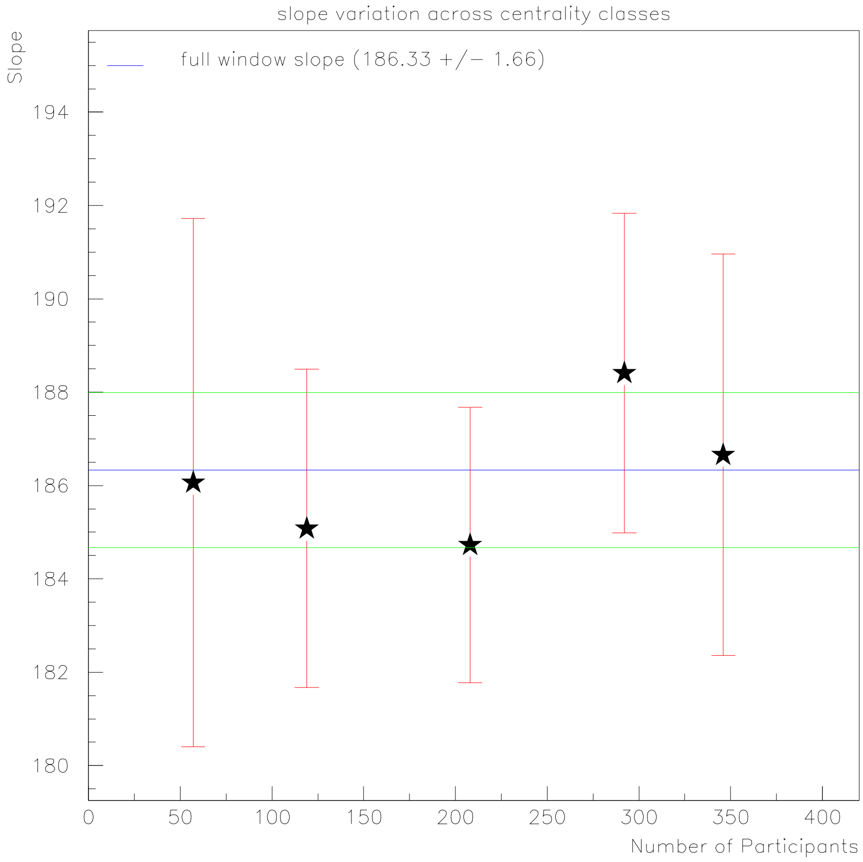

Figure 4.18: Variation in slope with different classes of centrality

Figure 4.18 show that the slope is fairly stable throughout different ranges of centrality. All the points vary around the average point with none going more than 1σ away from the overall value.

The variation of the final yield with number of Wounded nucleons is shown in the Figure 4.19.

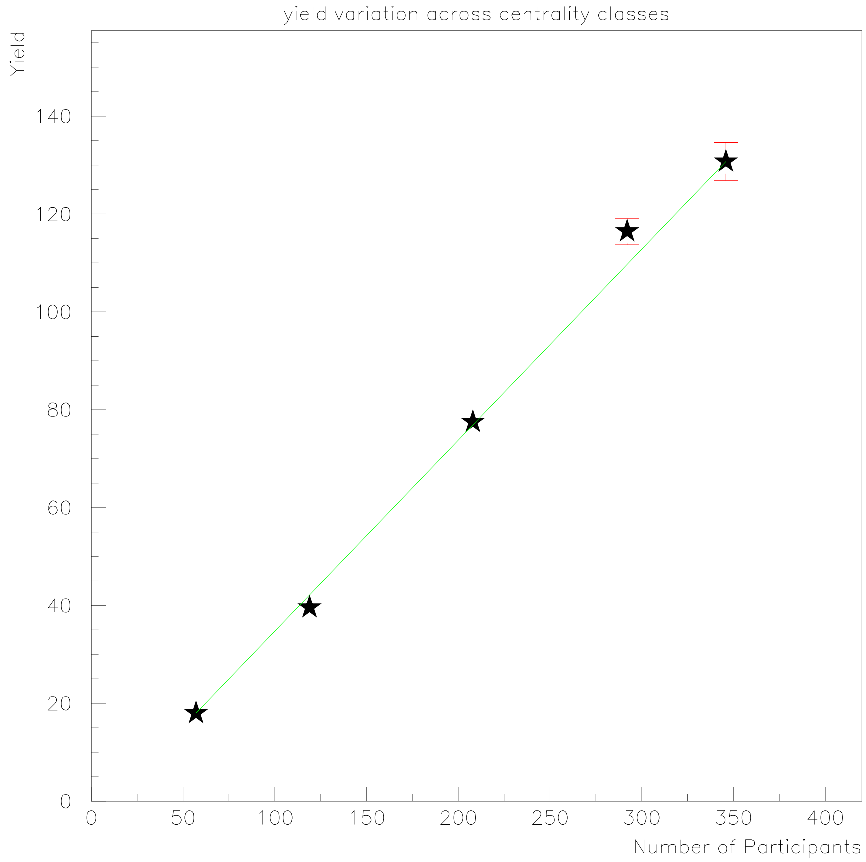

Figure 4.19: Variation in yield with different classes of centrality

The values of the yield appear to vary linearly with number of participants. This suggests that there is no phase change as you progress from one centrality class to another. The line has been fitted using a χ^2 method and has an intercept of 5.7 $\pm$1.0 and a gradient at 0.40 $\pm$0.008. The χ^2 of the fit is 3.8 with 3 degrees of freedom. For completeness Table 4.13 shows the ratio of final yield to number of wounded nucleons.

Table 4.13: Variation of Yield/Nwound over the MSD classes, number of participants taken from [41]

Class	Number of participants	Yield	Yield/Nwound
0	57 ± 5	18.0 ± 0.7	0.32 ± 0.03
1	119 ± 5	39.6 ± 0.9	0.33 ± 0.02
2	208 ± 5	77.6 ± 1.6	0.37 ± 0.01
3	292 ± 1	116.4 ± 2.7	0.40 ± 0.01
4	346 ± 1	130.7 ± 3.9	0.38 ± 0.01

4.5 R_{cp} and Cronin effect

R_{cp} is defined as the ratio of the P_T spectra of the most central and most peripheral collisions. It is introduced in more detail in section 1.5.6. and is defined by the equation:

$$R_{CP}(p_t) = \frac{< N_{\mathrm{collP}} >}{< N_{\mathrm{collC}} >} \times \frac{\mathrm{d}^2 N_{\mathrm{AA}}^{\mathrm{C}}/\mathrm{d}p_t\mathrm{d}y}{\mathrm{d}^2 N_{\mathrm{AA}}^{\mathrm{P}}/\mathrm{d}p_t\mathrm{d}y} \tag{4.1}$$

In performing the study on R_{cp} it is not necessary to use the weighted data sample as the weights are not dependent on centrality class. The evidence for this is shown in section 5.6 Figure 5.29 for the 158 GeV 2000 data set as more than one particle has been considered in this section. A plot of R_{cp}, using the most central 5% and the most peripheral classes, for all the tracks in the background tapes which fall within the cuts defined in Table 3.4 is shown in Figure 4.20. The low statistics at high P_T values makes it hard to draw any strong conclusions from Figure 4.20, Although there is a drop at high P_T there is not enough support to claim that we

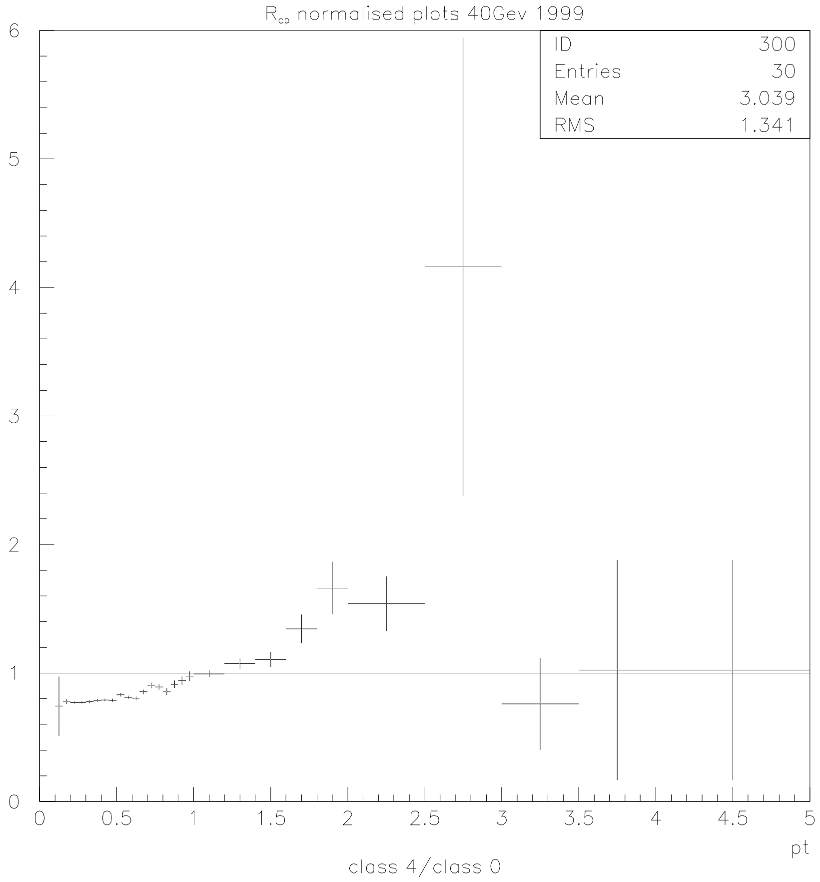

Figure 4.20: R_{cp} for 1999 background tapes data within defined cuts

see the suppression. A more detailed study will be done using the 158 GeV/c data set taken in 2000. This is discussed further in the next chapter.

4.5.1 Comparison With Other Experiments and Summary

NA57 is not the only experiment to consider the yields and slopes of negatively charged particles. The NA49 experiment[42], which was also run at the SPS at CERN, has measured yields and inverse slopes of π^- particles. The NA49 experiment is able to differentiate between different particles as it has particle identification. The particle identification is done using time projection chambers. It also measures the particles over a larger range in rapidity. The rapidity distribution found by the NA49 experiment for π^- particles is shown in Figure 4.21[43] for both 40GeV and 158GeV beam energies in central Pb-Pb collisions. In Figure 4.21 the x-axis is the variation of rapidity around central rapidity this allows a direct comparions of the distributions of the two beam energies, rather than having the two distributions offset at 2.22 and 2.91. The negative side of the plot is also a mirror of the positive side as the distribution in rapidity is expected to be symmetric around mid rapidity. The results found by the NA49 experiment in central collisions can be

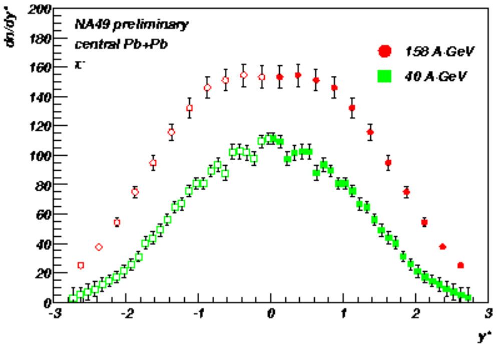

Figure 4.21: Rapidity spectra of π^- mesons produced in central Pb-Pb collisions at 40GeV and 158GeV from the NA49 experiment.

compared to those found by the analysis described in this thesis. However the results presented in this thesis are not just for π^- particles they are for all negative particles and so will have a contamination of kaons and $\overline{p}$. This will mean that the yields and slopes found by NA49 for π^- particles are expected to be lower than those found by the NA57 experiment for negatively charged particles. A summary of the results for π^- and K^- mesons and $\overline{p}$ from the NA49 experiment are given in Table 4.14[44][45].

The yields and slopes for the 40 GeV data set is higher for the NA57 negatives than for the NA49 π^- mesons. This, as stated previously, is expected due to the contamination of kaons and $\overline{p}$ particles. The yields for the NA49 data set are also done for the most central 7%, this means that weighting the inverse slopes with the values of the yields to see how well the combination of the three particle species

Table 4.14: NA49 yields and slopes for π^-, K^- and $\overline{p}$ for central (7%) Pb-Pb collisions at central rapidity and NA57 negative yields and slopes for central (5%) Pb-Pb collisions at 40GeV.

Particle	Inverse Slope	Yield
π^-	$169 \pm 2 \pm 10$	$106.1 \pm 0.4 \pm 6$
K^-	$226 \pm 3 \pm 6$	$7.58 \pm 0.12 \pm 1.4$
$\overline{p}$	246 ± 35	0.32 ± 0.03
NA57 negatives	186.7 ± 4.4	130.74 ± 3.93

compares with the NA57 result is not a fair comparison. A comparison for the 158 GeV data set is shown at the end of chapter 5.

Summary

The 1999 40 GeV Pb-Pb data set has been fully analysed using a weighting method to correct for efficiencies and phase space coverage. Cuts on the data to isolate negatively charged candidates originating from the target region were defined using both the real data and Monte Carlo generated data. An error calculation was performed on the BY impact parameter which took into account multiple scattering and a measurement error. The function which was defined using this calculation was also used to add further support to the definition of the BY impact parameter cut. The results of this analysis have been used to calculate final inverse slopes and yields for all centrality classes and R_{CP}. Although R_{CP} has been looked at the for the background tapes used in the analysis a lack of statistics at high P_T means that no satisfactory conclusions can be drawn for this data set. The final inverse slopes and yields which are summarised in Table 4.12 have been shown to be stable in both stability tests performed. A comparison with NA49 data shows that the inverse slopes and yields are higher than that of π^- mesons. This is due to the kaon and $\overline{p}$ contamination within the negative sample. However the values of the slopes and yields found is reasonable when this is taken into account and compared the results from NA49.

Chapter 5

Analysis of 158 A GeV/c Pb-Pb Data

5.1 Real Data and Monte Carlo Comparisons

The 158 GeV/c data was taken in two separate samples in two different years of running; 1998 and 2000. Although these two data sets used slightly different set ups for the experiment the results should be statistically compatible. Both data sets were sampled using the selection cuts defined in Table 3.5 and the number of tracks and events sampled are defined in Table 3.6. These tracks were then run through the weighting chain that was described in section 3.4. Of the tracks sampled none failed to complete the chain, however 23 tracks in the 2000 data sample and 49 in the 1998 data sample produced a weight of infinity. This is because none of the tracks generated at the GEANT stage were found within the cuts in the final output by WGTCAL. Although finding zero tracks should give a weight of infinity, the analysis programs used produce a value of zero. This is because zero is easier to process than infinity.

Figure 5.1 shows the position of the tracks which have a weight of zero. The scale of the plot is the same as that used to show the acceptance window later in this chapter, this allows an idea of where they lie in relation to the acceptance window to be gained. The green line is the minimum P_T value defined later in this chapter for the acceptance window.

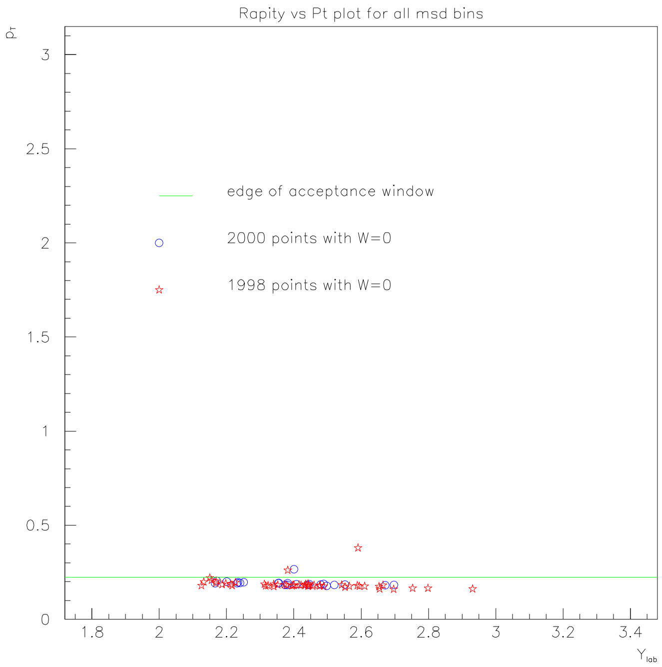

Figure 5.1: The P_T and rapidity values of tracks with a weight of zero for both the 1998 and 2000 data samples

As was done in the 40 GeV 1999 data analysis, the first thing to check is that generated *Monte Carlo* data matches the real data, from which the tracks were sampled, for both the BY and BZ impact parameters which are cut on. These comparisons are shown in Figures 5.2 and 5.3 for the 1998 data, BY and BZ respectively, and Figures 5.4 and 5.5 for the 2000 data set. The red histogram represents the *Monte Carlo* data and the black is the real data.

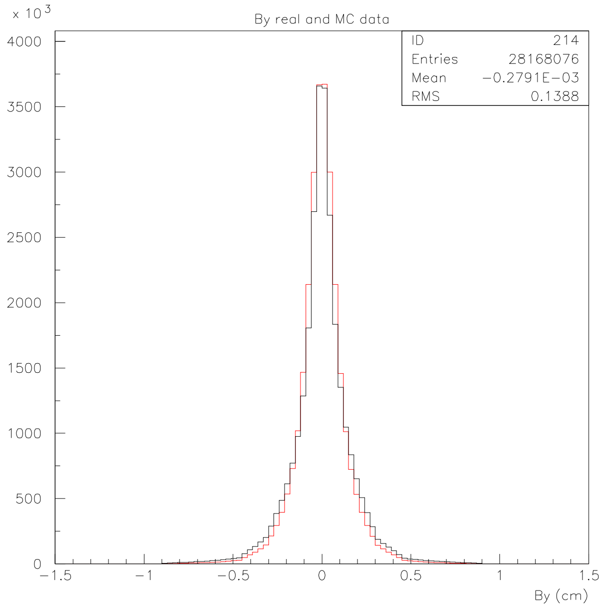

Figure 5.2: Monte Carlo generated data compared to real data from the 1998 data set and the BY impact parameter

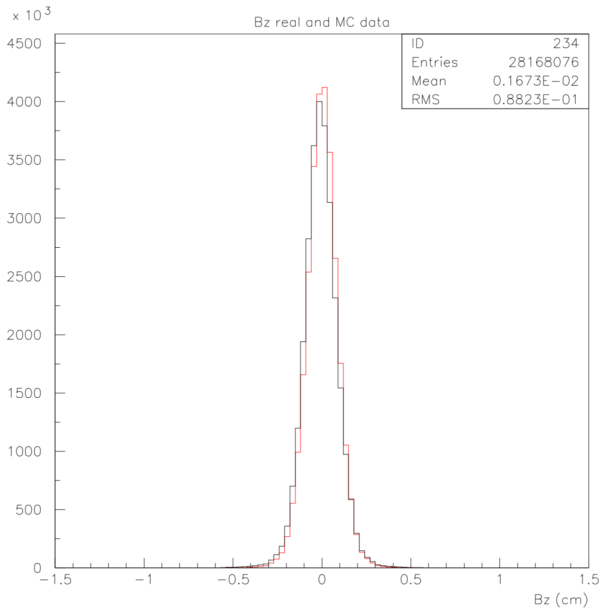

Figure 5.3: Monte Carlo generated data compared to real data from the 1998 data set and the BZ impact parameter

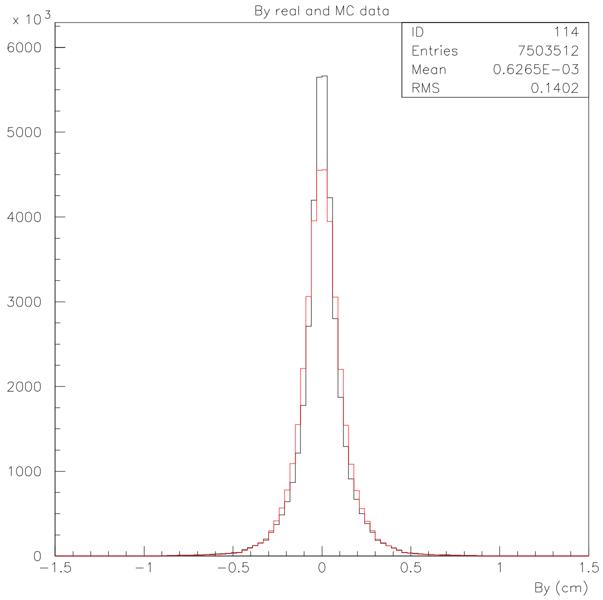

Figure 5.4: Monte Carlo generated data compared to real data from the 2000 data set and the BY impact parameter

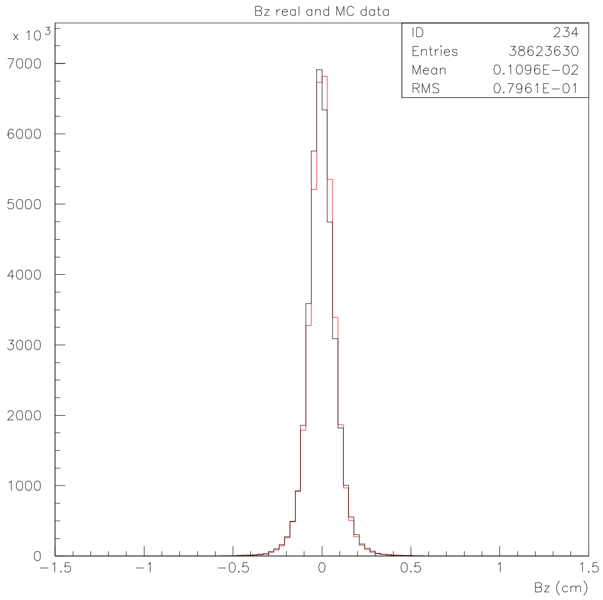

Figure 5.5: Monte Carlo generated data compared to real data from the 2000 data set and the BZ impact parameter

The comparisons of the real and generated data show a good agreement for both the BY and BZ impact parameters in both data sets. The only small difference is in the BY impact parameter for the 200 data which shows the Monte carlo with a slightly wider distribution, this is shown in Figure 5.4. However the difference is only small and so is not a cause for concern. Overall the good agreement between the real data and the generated date means that there is no need for the shift to be put into the generated data as was done for the 40 GeV/c data set.

5.2 Weighted Data Fitting

5.2.1 Rapidity distribution and acceptance window

The 1998 and 2000 data sets have very similar acceptance regions and so it is possible to use the same acceptance window definition for both data sets. This will also allow comparisons of the two data sets. Figure 5.6 shows the P_T vs rapidity plot for the 1998 weighted data.

The plot shows that the distribution is similar in shape to that of the 40 GeV data set, however the rapidity values are higher than those found in the 40 GeV data set. By looking at the distribution of *"high weights"* in Figure 5.6 a square acceptance region can be defined, from this the sides of the acceptance window can also be defined using the formula given in section 2.3.2 to give a final acceptance window for the data set. The square region is shown in Figure 5.7 and the final acceptance window for the 1998 data set is shown in Figure 5.8 with the parameters used defined in Table 5.1.

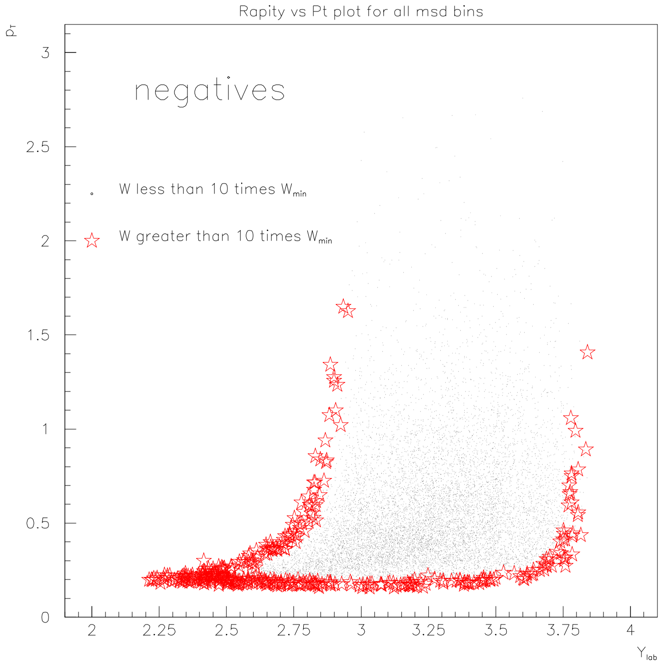

Figure 5.6: Rapidity versus P_T for the 1998 data set with *"high weights"* highlighted

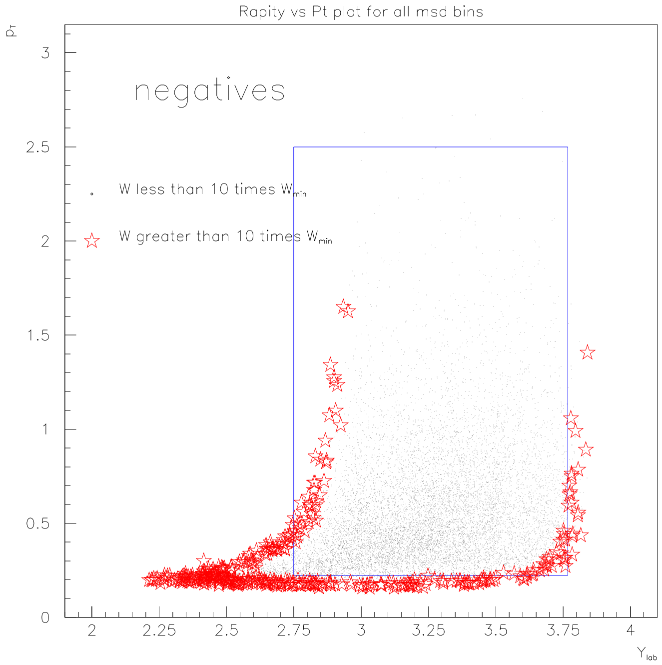

Figure 5.7: Rapidity versus P_T for the 1998 data set showing limits of acceptance

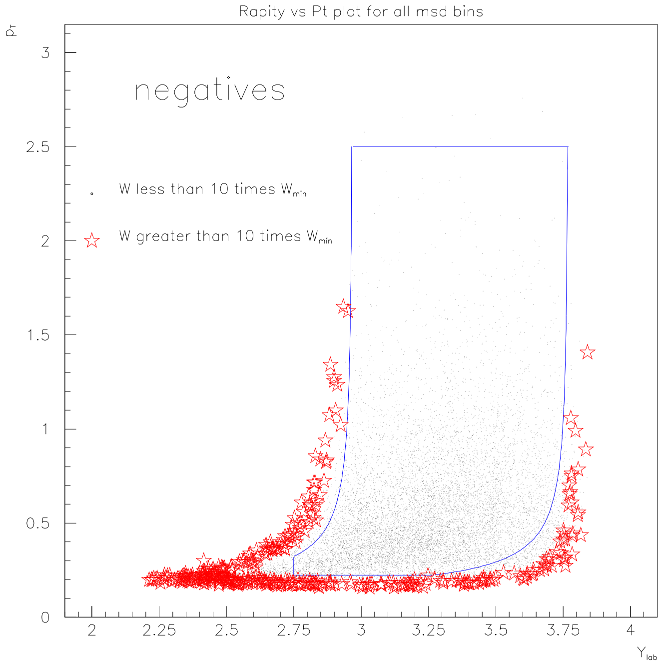

Figure 5.8: Rapidity versus P_T for the 1998 data set with acceptance window using parameters from Table 5.2 shown

Table 5.1: Acceptance window parameter definitions for 1998 and 2000 data sets

Parameter	value
P_t minimum	0.223
P_t maximum	2.5
Y_{lab} minimum	2.75
Y_{lab} maximum	3.768
θ	0.0461
ψ	0.103

As stated previously the 2000 data set will use the same window as the 1998 data set to allow direct comparisons of the results. The acceptance window is shown in Figure 5.9 for the 2000 data.

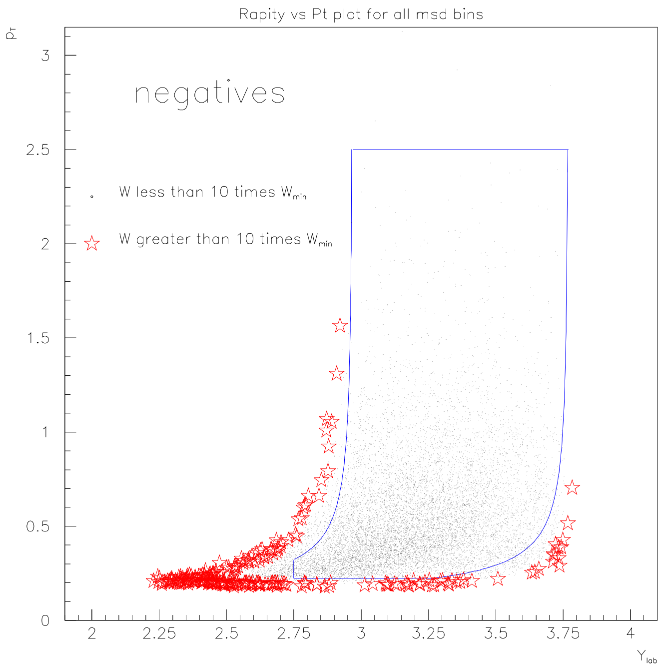

Figure 5.9: Rapidity versus P_T for the 2000 data set with acceptance window using parameters from Table 5.2 shown

Figure 5.10 does show that the 2000 data set has a slightly narrower rapidity distribution than for the 1998. The difference is probably because the 2000 data set is taken using a slightly longer telescope. This difference does not however affect the acceptance region being used for the two data sets.

The rapidity distribution for both data sets is shown in Figure 5.10 with the sigma values, of the fitted Gaussian, shown in Table 5.2

The centre of the Gaussian fit to the rapidity distribution shown in Figure 5.10 has its mean fixed to 2.91 as this is the centre of rapidity for the 158 GeV data.

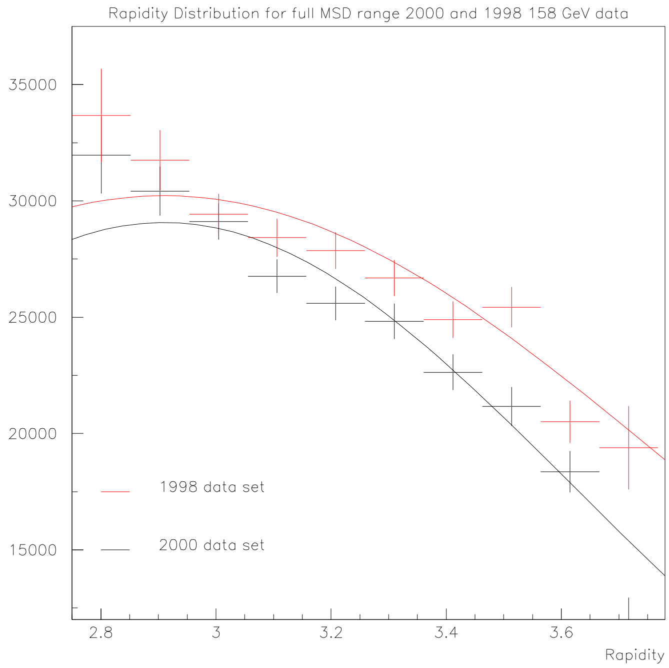

Figure 5.10: Rapidity distributions for 1998 and 2000 data sets within the acceptance window, with the gaussian fits shown

Table 5.2: σ values for the Gaussian fit of the rapidity distributions of 1998 and 2000 data sets

Sample (event sampled)	MSD range	σ
1998 (3278)	Full	0.896 ± 0.011
1998 (288)	5% most central	0.874 ± 0.023
2000 (3478)	Full	0.716 ± 0.006
2000 (279)	5% most central	0.735 ± 0.016

Although the values of sigma found for the two data sets are different the general trends of the two are very similar. Fitting these gaussians to the rapidity distributions gives the results shown in Table 5.3 for the extrapolation factor, uncorrected yields and inverse slopes in both the full MSD range and the 5% most central collisions. Table 5.3 also shows the uncorrected yields and inverse slopes for a Gaussian fit with a fixed σ of 0.8. This value is chosen as a compromise between the two data sets.

Table 5.3: Inverse slope, extrapolation factors and uncorrected yields of the 158 GeV/c data samples with free σ shown in Table 5.2

Sample	MSD range	Extrapolation Factor	Inverse slope	Uncorrected Yield
1998 free sigma	Full	1.78	214.0 ±1.8	85.2 ±1.0
1998 free sigma	5% most central	1.74	226.3 ±4.2	192.2 ±4.8
1998 fixed sigma	Full	1.79	215.1 ±1.7	86.0 ±1.0
1988 fixed sigma	5% most central	1.75	227.3 ±4.1	193.8 ±4.8
2000 free sigma	Full	1.86	203.1 ±1.6	75.8 ± 0.8
2000 free sigma	5% most central	1.87	206.6 ±3.9	171.8 ±4.4
2000 fixed sigma	Full	1.85	201.9 ±1.6	75.1 ±0.8
2000 fixed sigma	5% most central	1.83	205.8 ±3.7	170.5 ±4.3

5.2.2 Inverse Slope Fitting on Real Data

Table 5.3 shows that with a fixed σ value the uncorrected yields vary by about 10-15%. However, without background corrections no real conclusions can be drawn from these results. The inverse slope does, however, show a difference between the two data sets. With the fixed σ value the difference is just below 10%. To see if this is an error within the weighting procedure or the calculation of inverse slope the real data can be looked at. By considering the parameterisation

$$\frac{d^2N}{dm_T dy} = m_T\, f(y) e^{-\, m_T/T},$$

which was discussed in section 3.4.2 the inverse slopes of the real data can be seen. A plot of M_T against $ln\left(\frac{1}{M_T}\frac{d^2N}{dm_T dy}\right)$ is shown in Figure 5.11 with the inverse slope found shown. The inverse slope has been determined using the maximum likelihood fitting method which is used on the weighted data. Both data sets are also shown to highlight the difference between them. The fits have been done over the range of $0.75 < M_T < 2.75$ GeV

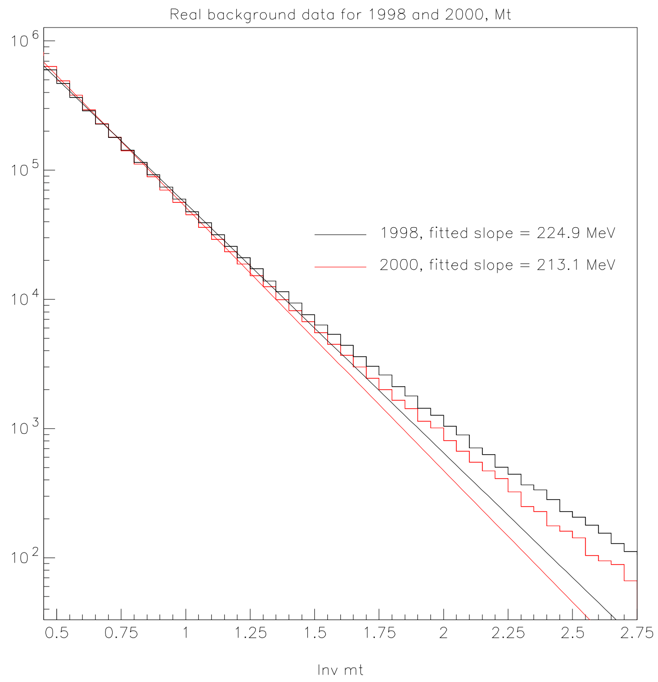

Figure 5.11: Real data inverse slope showing difference in slope between data samples.

As shown in Figure 5.11 the two 158 GeV data sets show a difference in slope. As with the weighted data this difference is <10%. Figure 5.11 has been plotted over a slightly different range than the weighted data as the real data has more tracks at higher M_T than the real data and to be sure that there is no bias from the slope due to the point at which M_T reaches its minimum value. Although this means that the slopes found are slightly higher than those from the weighted data the difference between data sets is still the same. This all shows that the difference in slopes is not due to the weighting chain or the calculation of slope. It is in fact a difference in slope that was present in the real data taken in the experimental runs.

A reason for this difference in the two data sets is currently still unknown. It will be discussed later in this chapter along with a discussion of systematic errors.

5.3 Corrections and Final Yields and Slopes

5.3.1 Background correction

As with the 40 GeV data sets the yields need to be corrected for background. This is done in the same way as the 1999 data sample with both the number of events sampled and the sum of weights being corrected. The values of the corrections in the full MSD range and the 5% most central range are given in Tables 5.4 and 5.5

Table 5.4: Background correction factors for all centrality classes for 158 GeV 1998 data set

Centrality class	Correction to sum of weights	Correction to Number of events sampled	Overall Correction Factor
Class 0	0.12%	12%	1.14
Class 1	0.0005%	0.5%	1.005
Class 2	0.0003%	0.005%	1.00005
Class 3	0%	0%	1.0
Class 4 (5% most central)	0%	0%	1.0
Full	0.03%	3.4%	1.04

Table 5.5: Background correction factors for all centrality classes and the full centrality range for 158 GeV 2000 data set

Centrality class	Correction to sum of weights	Correction to Number of events sampled	Overall Correction Factor
Class 0	0.6%	15%	1.17
Class 1	0.04%	0.7%	1.007
Class 2	0%	0.01%	1.0001
Class 3	0%	0%	1.0
Class 4 (5% most central)	0%	0%	1.0
Full	0.06%	4.4%	1.05

These background corrections can now be applied to the uncorrected yields in Table 5.3 to give a final yield for both 158 GeV data sets. The final yields for both a free sigma value and a fixed sigma of 0.8 are shown in Table 5.6.

The corrected yields are approximatley 10-12% higher for the 1998 data set than for the 2000 data set. This follows the same trend as the inverse slope which was also higher for the 1998 data set as shown in Table 5.3. Therefore, this introduces a systematic error into the 158 GeV data set, which is of the order of 10%.

5.4 Acceptance Window Stabilty

In order to test the stability of the acceptance window and confirm it is not the source of the systematic error the same two tests as were performed on the 40 GeV data set can be repeated. These tests involve using smaller windows on the two samples to test for any edge effects and splitting the acceptance window up into

Table 5.6: Corrected yields of the 158 GeV data samples with free σ shown in Table 5.2 and fixed σ of 0.8

Sample	MSD range	Corrected Yield
1998 free sigma	Full	88.2 $\pm$1.0
1998 free sigma	5% most central	192.2 $\pm$4.8
1998 fixed sigma	Full	89.0 $\pm$1.0
1988 fixed sigma	5% most central	193.8 $\pm$4.8
2000 free sigma	Full	79.3 $\pm$ 0.9
2000 free sigma	5% most central	171.8 $\pm$4.4
2000 fixed sigma	Full	78.5 $\pm$0.9
2000 fixed sigma	5% most central	170.5 $\pm$4.3

slices to test its stability across the rapidity range.

5.4.1 Window Size Test

As stated previously the use of a smaller window should give a similar inverse slope and yield as the larger window as the majority of the data is still present. However the test is still valid as it will show up any problems with high weights near the edge of the acceptance window. The two smaller windows which were tested are shown on the 2000 data set in Figure 5.12 and their parameters are shown in Table 5.7.

The background corrected yields and the inverse slopes of these 3 windows are shown in Table 5.8 for the 1998 data set and Table 5.9 for the 2000 data set. For all 3 windows the Gaussian fit to the rapidity has a fixed σ of 0.8

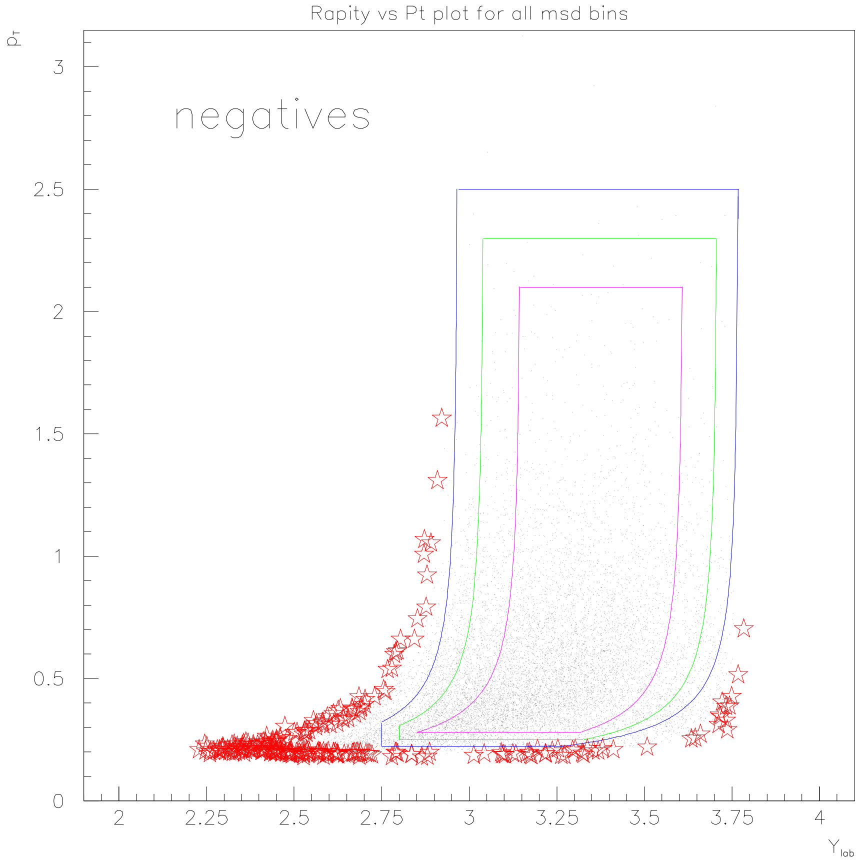

Figure 5.12: Acceptance windows used to test for any edge effects present in larger acceptance window, parameters for windows shown in Table 5.7

For both data sets the inverse slope increases slightly and the corrected yield decrease slightly as the acceptance window is reduced in size. For the 5% most central collisions this happens within the errors. However, for the full centrality range the variation is outside the range of the statistical errors. This may account for some of the 10% systematic error found previously. However, it does not account for it in full. The second test using slices of the acceptance window may explain this in further detail.

Table 5.7: Acceptance window parameter definitions for the two smaller windows as well as the original window used on 158 GeV data sets

Parameter	Original Window	Window 2	Window 3
P_T minimum	0.223	0.25	0.28
P_T maximum	2.5	2.3	2.1
Y_{lab} minimum	2.75	2.8	2.85
Y_{lab} maximum	3.768	3.68	3.6
θ	0.0461	0.049	0.054
ψ	0.103	0.0956	0.086

Table 5.8: Inverse slopes and corrected yields for the 3 acceptance windows defined using parameters in Table 5.7 for the 1998 data set.

Window	MSD range	slope	yield
Full Window	Full	215.1 ±1.7	89.0 ±1.0
Full Window	5% most central	227.3 ±4.1	193.8 ±4.8
Window 2	Full	218.0 ±1.9	87.1 ±1.0
Window 2	5% most central	227.5 ±4.5	192.1 ±5.1
Window 3	Full	219.3 ±2.3	86.1 ±1.2
Window 3	5% most central	230.0 ±5.4	188.2 ±5.7

5.4.2 Window Slices Test

By investigating the inverse slope and yield of various slices of the acceptance window any variation in these results due to the rapidity distibution will be highlighted. As with the 40 GeV data set the window can be split up into 4 slices. The parameters of these slices are shown in Table 5.10 and a plot of the acceptance window with the slices is shown in Figure 5.13.

Table 5.9: Inverse slopes and corrected yields for the 3 acceptance windows defined using parameters in Table 5.7 for the 2000 data set.

Window	MSD range	slope	yield
Full Window	Full	201.9 $\pm$1.6	78.5 $\pm$ 0.9
Full Window	5% most central	205.8 $\pm$3.7	170.5 $\pm$4.3
Window 2	Full	206.3 $\pm$1.8	77.0 $\pm$ 0.9
Window 2	5% most central	206.7 $\pm$4.1	169.9 $\pm$4.5
Window 3	Full	208.2 $\pm$2.1	75.2 $\pm$ 1.0
Window 3	5% most central	211.3 $\pm$5.0	166.4 $\pm$5.1

Table 5.10: Parameter definitions for various slices of the acceptance window for the 158 GeV data set.

Parameter	Original Window	slice 1	slice 2	slice 3	slice 4
P_t minimum	0.223	0.223	0.223	0.223	0.223
P_t maximum	2.5	2.5	2.5	2.5	2.5
Y_{lab} minimum	2.75	2.75	2.75	2.75	2.75
Y_{lab} maximum	3.768	3.123	3.2965	3.5064	3.768
θ	0.0461	0.103	0.088	0.074	0.06
ψ	0.103	0.088	0.074	0.06	0.0461

The Inverse slopes and yields of all the slices and the original window are shown in Table 5.11 for the 1998 data set and Table 5.12 for the 2000 data set. Once again, all results are calculated using a gaussian rapidity distribution with a fixed σ of 0.8.

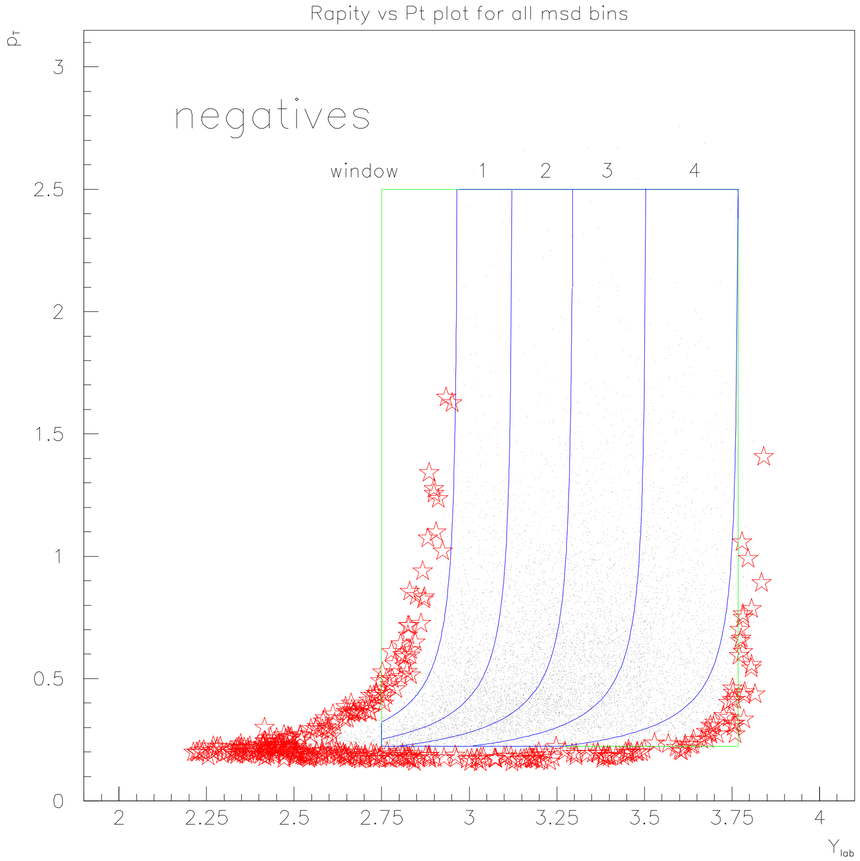

Figure 5.13: Different slices of the main acceptance window used on the 158 GeV data set, shown on the 1998 data sample.

The observed variation of the yields in the full multiplicity range is outside the statistical errors for both the samples. The same is true for the 1998 data set in the 5% most central MSD class. These variations are shown in Figures 5.14-5.17.

Table 5.11: Yield and Inverse slope results for slices of the acceptance window using the 1998 data set

Slice	MSD Class	Inverse Slope	Yield
Full Window	Full	215.1 ±1.7	89.0 ±1.0
Full Window	5% most central	227.3 ±4.1	193.8 ±4.8
1	Full	225.7 ±4.8	81.4 ± 2.3
1	5% most central	237.3 ±11.1	178.0 ±11.0
2	Full	207.8 ±3.4	88.0 ±1.9
2	5% most central	223.5 ±8.3	178.9 ±8.8
3	Full	215.5 ±3.1	89.2 ±1.7
3	5% most central	230.0 ±7.3	194.6 ±8.5
4	Full	222.3 ±3.5	94.4 ±2.0
4	5% most central	231.5 ±8.0	215.3 ±10.1

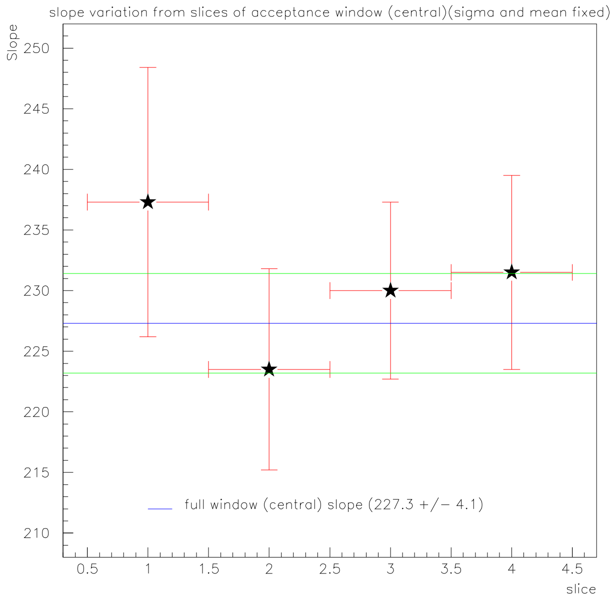

Figure 5.14: Variation of inverse slope across the slices, of the acceptance window, defined in Table 5.10 for the 1998 data set, Full MSD range.

Table 5.12: Yield and Inverse slope results for slices of the acceptance window using the 2000 data set

Slice	MSD Class	Inverse Slope	Yield
Full Window	Full	201.9 ±1.6	78.5 ± 0.9
Full Window	5% most central	205.8 ±3.7	170.5 ±4.3
1	Full	212.0 ±4.0	72.8 ±1.8
1	5% most central	202.9 ±8.6	179.8 ± 10.0
2	Full	199.9 ±2.9	82.3 ±1.8
2	5% most central	198.1 ±6.9	169.0 ±7.7
3	Full	205.4 ±2.8	80.8 ±1.5
3	5% most central	223.2 ±7.2	170.9 ±7.4
4	Full	200.2 ±3.6	76.2 ±1.9
4	5% most central	202.0 ±8.4	166.5 ±9.4

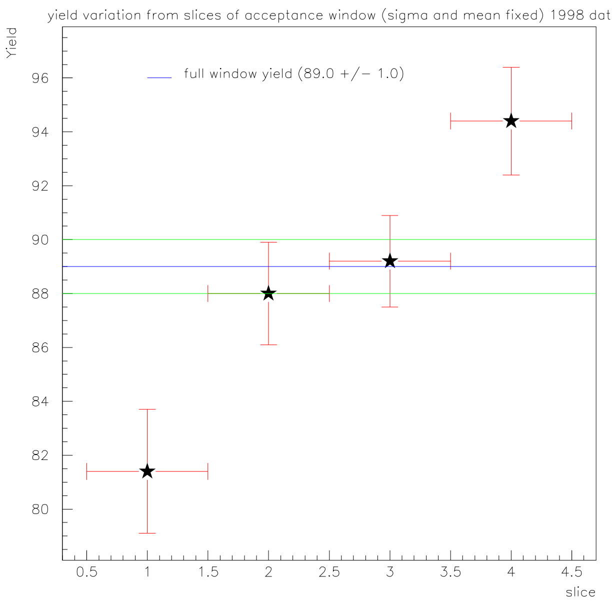

Figure 5.15: Variation of corrected yield across the slices, of the acceptance window, defined in Table 5.10 for the 1998 data set, Full MSD range.

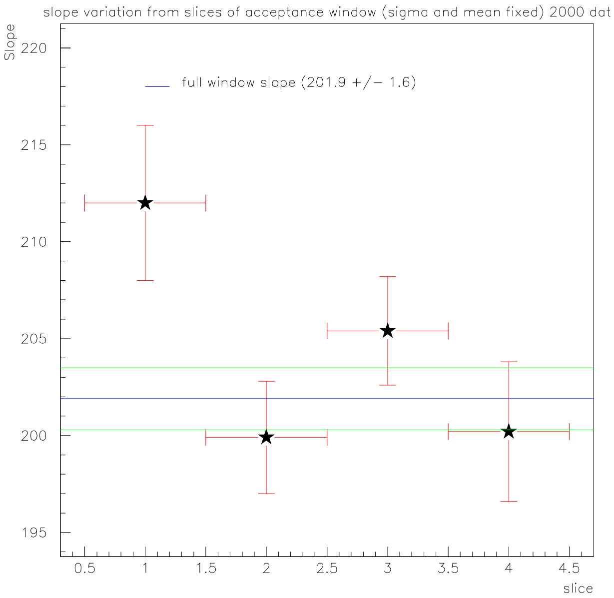

Figure 5.16: Variation of inverse slope across the slices, of the acceptance window, defined in Table 5.10 for the 2000 data set, Full MSD range.

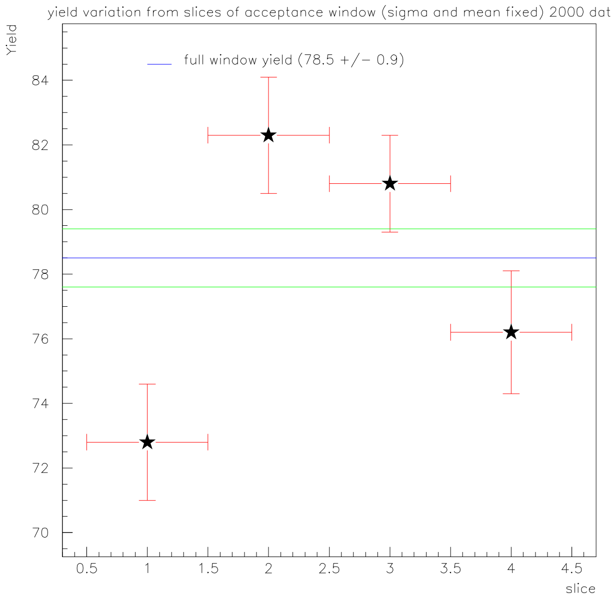

Figure 5.17: Variation of corrected yield across the slices, of the acceptance window, defined in Table 5.10 for the 2000 data set, Full MSD range.

This may be due to the modelling of the rapidity distribution as a Gaussian fit being too simple. Therefore a further test can be done where the acceptance window is divided up into slices of rapidity and no assumptions are made about the rapidity distribution. The rapidity distribution within these slices is defined as flat and the final yields are only extrapolated across the rapidity region used. The final yields can then be plotted as a function of rapidity and will have the same general distribution as the rapidity. The segmented up acceptance window is shown in Figure 5.18 with the new slice parameters shown in Table 5.13. The results for each slice are shown in Table 5.14 for the 1998 data set and Table 5.15 for the 2000 data set.

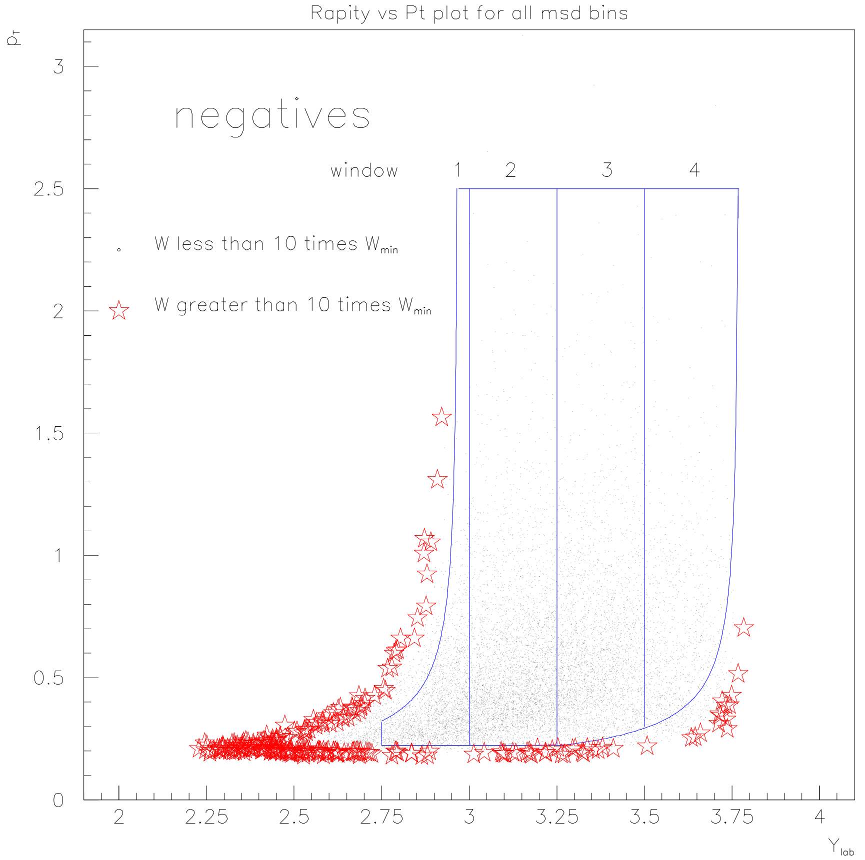

Figure 5.18: Different slices of the main acceptance window used on the 158 GeV data set for the second window slices test, shown on the 2000 data sample.

Table 5.13: Parameter definitions for various slices in rapidity of the acceptance window for the 158 GeV data set.

Parameter	Original Window	slice 1	slice 2	slice 3	slice 4
P_t minimum	0.223	0.223	0.223	0.223	0.223
P_t maximum	2.5	2.5	2.5	2.5	2.5
Y_{lab} minimum	2.75	2.75	3.0	3.25	3.5
Y_{lab} maximum	3.768	3.0	3.25	3.5	3.75
θ	0.0461	0.0461	0.0461	0.0461	0.0461
ψ	0.103	0.103	0.103	0.103	0.103

Table 5.14: Yield and Inverse slope results for rapidity slices of the acceptance window using the 1998 data set

Slice	MSD Class	Inverse Slope	Yield
Full Window	Full	215.1 $\pm$1.7	89.0 $\pm$1.0
1	Full	202.8 $\pm$ 5.4	26.8 $\pm$ 0.7
2	Full	215.6 $\pm$ 2.9	23.9 $\pm$ 0.4
3	Full	215.7 $\pm$ 3.0	22.3 $\pm$ 0.4
4	Full	230.4 $\pm$ 4.8	17.4 $\pm$ 0.5

As stated previously the variation of the yields with rapidity will follow the same general trend as the rapidity distribution. Figure 5.19 shows this distribution for the 1998 data set and Figure 5.20 shows it for the 2000 data set. Both show a decrease in yield as rapidity increases. This is the same general trend as the rapidity distribution which was shown in Figure 5.10. Overall this supports the use of

Table 5.15: Yield and Inverse slope results for rapidity slices of the acceptance window using the 2000 data set

Slice	MSD Class	Inverse Slope	Yield
Full Window	Full	201.9 $\pm$1.6	78.5 $\pm$ 0.9
1	Full	187.8 $\pm$ 4.5	24.9 $\pm$ 0.6
2	Full	208.0 $\pm$ 2.6	21.9 $\pm$ 0.4
3	Full	209.2 $\pm$ 3.0	19.3 $\pm$ 0.4
4	Full	204.5 $\pm$ 4.8	15.0 $\pm$ 0.5

a rapidity distribution, however it does not show conclusively if a gaussian fit is a good approximation.

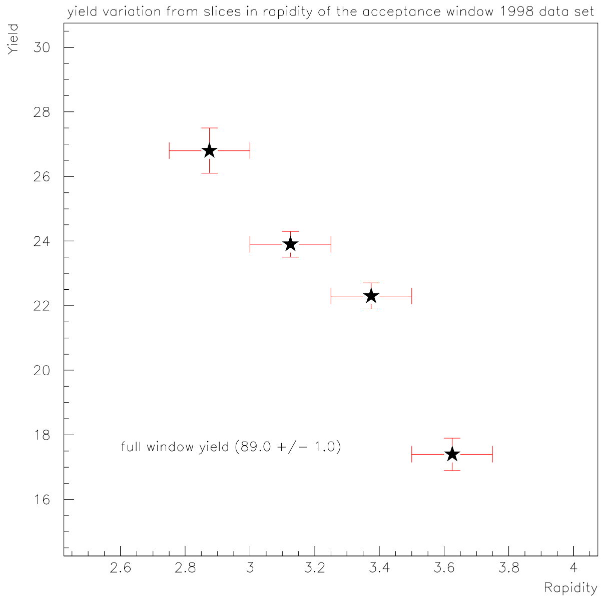

Figure 5.19: Variation of yield, extrapolated to $\frac{1}{4}$ unit of rapidity, with rapidity across the acceptance window for the 1998 data set

This method can also be used to calculate the overall yield. The final yield is

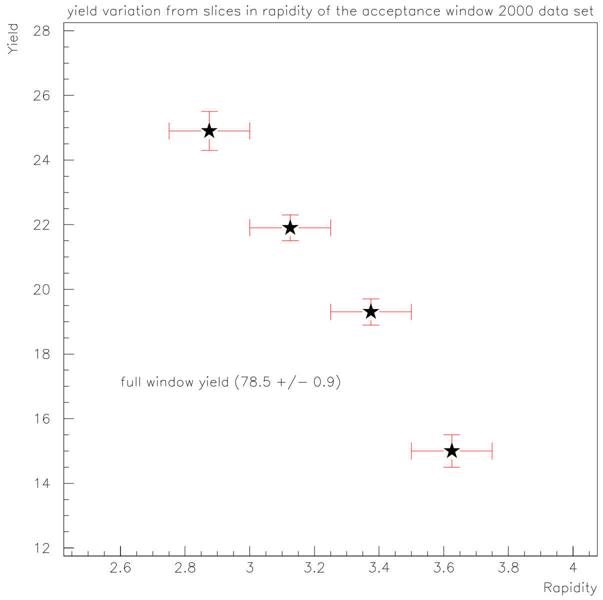

Figure 5.20: Variation of yield, extrapolated to $\frac{1}{4}$ unit of rapidity, with rapidity across the acceptance window for the 2000 data set

extrapolated to one unit in rapidity around central rapidity. To calculate this from the results shown in Tables 5.14 and 5.15 the weighted average of the first three windows is calculated, this is because these windows cover half the rapidity range of the extrapolation region, i.e from mid rapidity, 2.91 to 3.41. As these results have only been extrapolated over a $\frac{1}{4}$ unit of rapidity the result must then be multiplied by 4. Table 5.16 shows the weighted average of the yields from the first 3 slices in rapidity and the overall calculated yield for all centrality classes for the 1998 data. It also shows the final values as calculated by extrapolating the full window over one unit of rapidity around mid rapidity. Table 5.17 shows the same results but for the 2000 data set.

Table 5.16: Comparison of yield from rapidity slices to full window extrapolation for 1998 data set

Centrality Class	Weighted Average	Calculated Yield	Full Window Yield
Full	23.6 ± 0.3	94.4 ± 1.2	$78.5 \pm 0.9_{stat}$
0	6.1 ± 0.3	24.4 ± 1.2	$29.0 \pm 1.2_{stat}$
1	15.5 ± 0.4	62.0 ± 1.6	$64.8 \pm 1.5_{stat}$
2	26.4 ± 0.6	105.6 ± 2.4	$110.6 \pm 2.4_{stat}$
3	39.4 ± 1.0	157.6 ± 4.0	$161.3 \pm 3.7_{stat}$
4	47.6 ± 1.3	190.4 ± 5.2	$193.8 \pm 4.8_{stat}$

Table 5.17: Comparison of yield from rapidity slices to full window extrapolation for 2000 data set

Centrality Class	Weighted Average	Calculated Yield	Full Window Yield
Full	21.4 ± 0.3	85.6 ± 1.2	$89.0 \pm 1.0_{stat}$
0	5.3 ± 0.2	21.2 ± 0.8	$25.9 \pm 1.0_{stat}$
1	14.3 ± 0.3	57.2 ± 1.2	$57.2 \pm 1.3_{stat}$
2	25.1 ± 0.5	100.4 ± 2.0	$101.1 \pm 2.1_{stat}$
3	34.1 ± 0.8	136.4 ± 3.6	$140.8 \pm 3.3_{stat}$
4	41.0 ± 1.1	164.0 ± 4.4	$170.5 \pm 4.3_{stat}$

The two methods of calculating the yields show comparable results which further supports the fits used to the rapidity distribution and also demonstrates that the systematic error between the two data sets is probably within the data itself rather than due to the analysis method. Figure 5.21 for the 1998 data and 5.22 for the 2000 data show how the two calculated yields vary across centrality classes.

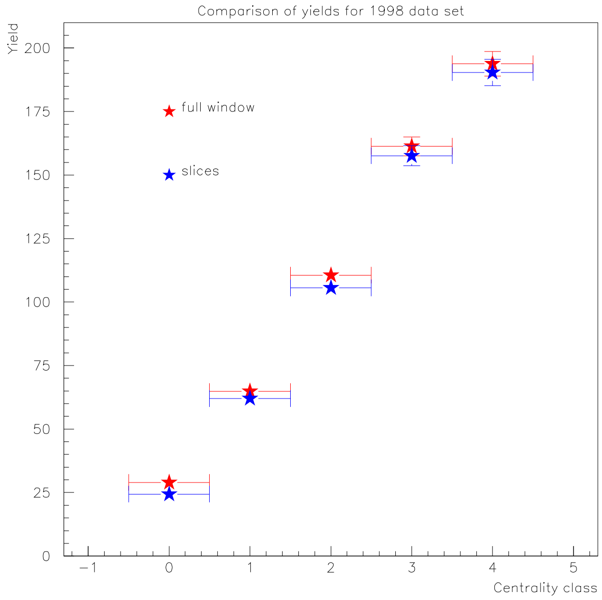

Figure 5.21: Comparison of final yield as a function of centrality for the 1998 data set. Red points indicate yield as calculated by extrapolating all data in window to one unit of rapidity, blue points represent yield as calculated by taking slices of rapidity and extrapolating over $\frac{1}{4}$ unit of rapidity then multiplying to full unit of rapidity.

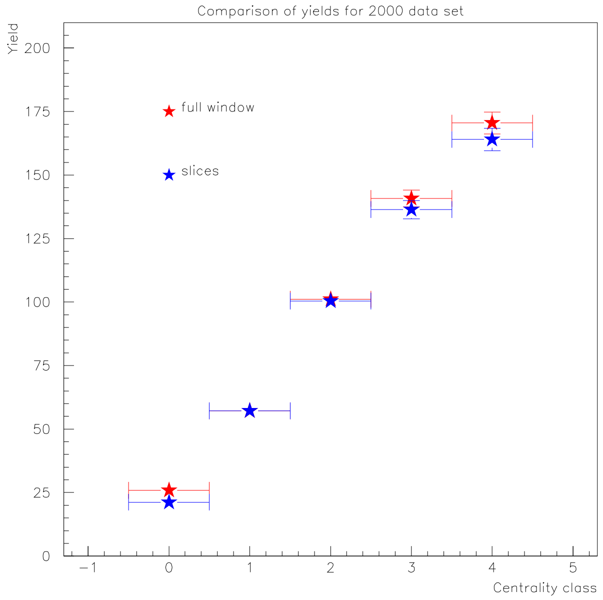

Figure 5.22: Comparison of final yield as a function of centrality for the 2000 data set. Red points indicate yield as calculated by extrapolating all data in window to one unit of rapidity, blue points represent yield as calculated by taking slices of rapidity and extrapolating over $\frac{1}{4}$ unit of rapidity, then scaling to a full unit of rapidity.

5.5 Systematic Errors and Final Inverse Slopes and Yields

The final yields and inverse slopes of all MSD classes are shown in Table 5.18 for the 1998 data set and Table 5.19 for the 2000 data set. Figure 5.23 shows the fit of the inverse slope for the 1998 data set. All of the yields are fully corrected for background and the rapidity distribution has also been fitted with a fixed sigma of 0.8 in order for two data sets to be compared and for consitency with the tests done on the acceptance window.

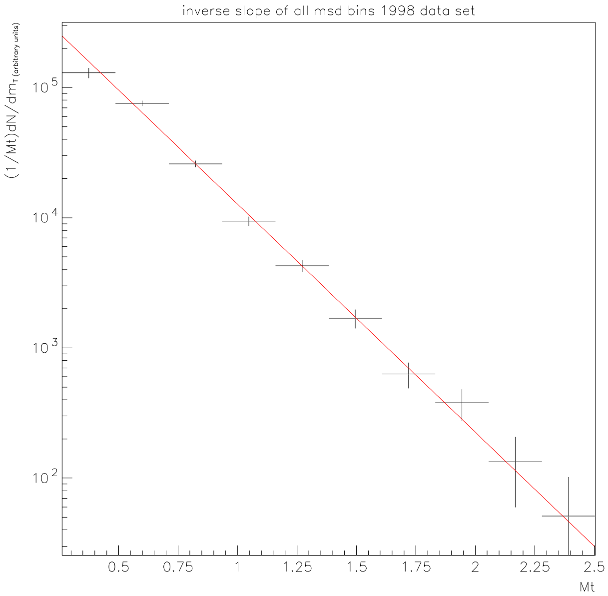

Figure 5.23: $ln\left(\frac{1}{m_T}\frac{dN}{dm_T}\right)$ versus m_T for the 1998 data set. The fitted line was obtained using a maximum likelihood fit.

Table 5.18: Final Inverse Slopes and Yields for the 1998 data set.

MSD class	Centrality	number of events sampled	Inverse Slope	Yield
full	full	3278	215.1 ±1.7	89.0 $\pm 1.0_{stat}$
0	42-56%	879	204.0 ±6.0	29.0 $\pm 1.2_{stat}$
1	25-42%	1037	206.4 ±3.5	64.8 $\pm 1.5_{stat}$
2	12-25%	680	214.8 ±3.3	110.6 $\pm 2.4_{stat}$
3	4.5-12%	394	217.1 ±3.6	161.3 $\pm 3.7_{stat}$
4	0-4.5%	288	227.3 ±4.1	193.8 $\pm 4.8_{stat}$

The 2000 data set shows a much more stable inverse slope across the centrality classes. The 1998 data set shows a consistent rise in the slope with the centrality of the collision. Figures 5.24 and 5.25 show the variation of inverse slope with centrality class for the 1998 and 2000 data sets respectivley.

Table 5.19: Final Inverse Slopes and Yields for the 2000 data set.

MSD class	Centrality	number of events sampled	Inverse Slope	Yield
full	full	3478	201.9 $\pm$1.6	78.5 $\pm 0.9_{stat}$
0	42-56%	960	198.1 $\pm$5.5	25.9 $\pm 1.0_{stat}$
1	25-42%	1094	197.4 $\pm$3.2	57.2 $\pm 1.3_{stat}$
2	12-25%	747	201.3 $\pm$2.9	101.1 $\pm 2.1_{stat}$
3	4.5-12%	398	206.5 $\pm$3.4	140.8 $\pm 3.3_{stat}$
4	0-4.5%	279	205.8 $\pm$3.4	170.5 $\pm 4.3_{stat}$

The variation of yield with number of wounded nucleons is shown for the 1998 and 2000 data sets in Figures 5.26 and 5.27 respectively. For the 1998 data the fit has an intercept of 5.9 $\pm$ 1.6, a gradient of 0.57 $\pm$ 0.01 and a χ^2 of 0.97 with 3 degrees of freedom. The 2000 data fit has an intercept of 5.1 $\pm$ 1.3, gradient of 0.5 $\pm$ 0.01 and a χ^2 of 0.3 with 3 degrees of freedom.

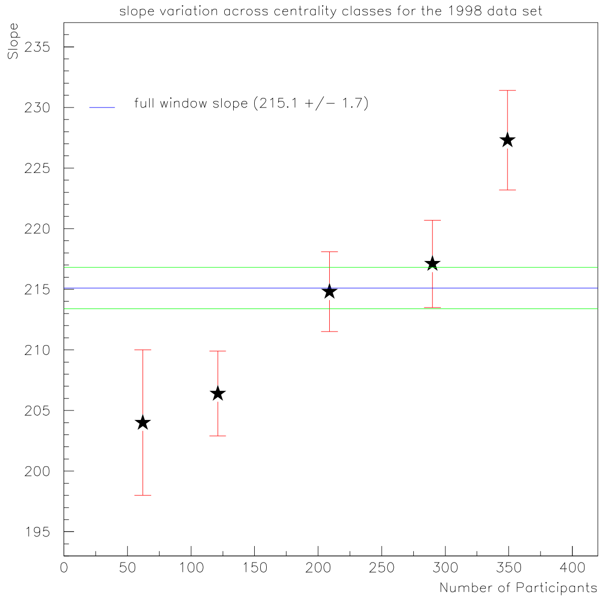

Figure 5.24: Variation in slope with different classes of centrality for the 1998 158 GeV/c data set.

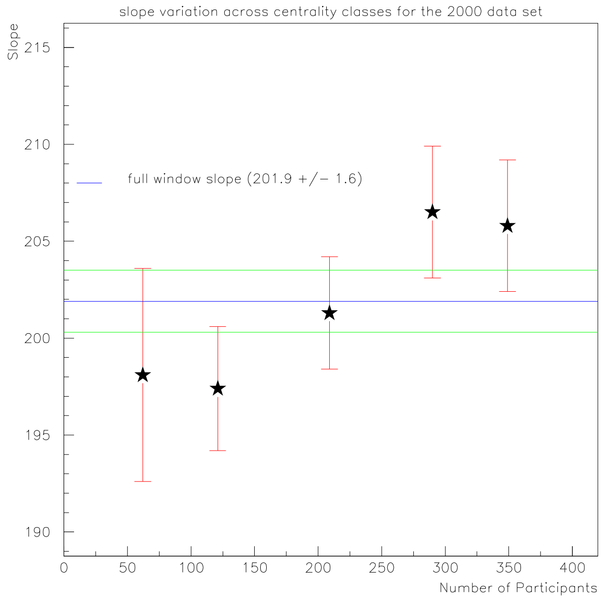

Figure 5.25: Variation in slope with different classes of centrality for the 2000 158 GeV/c data set.

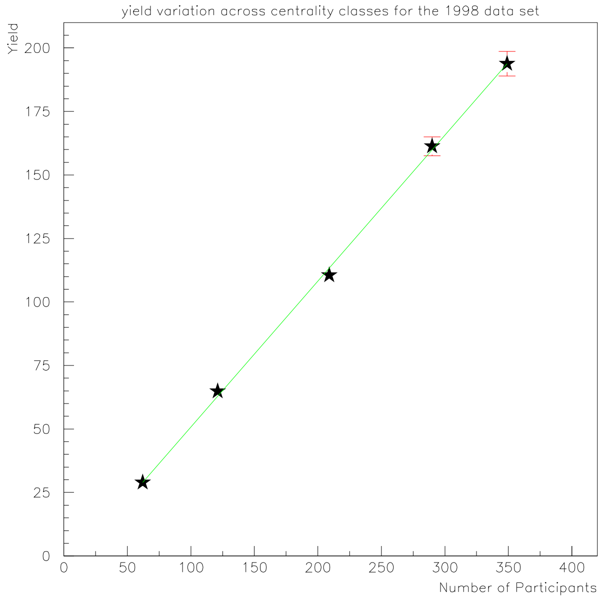

Figure 5.26: Variation in yield as a function of number of wounded nucleons for the 1998 158 GeV/c data set.

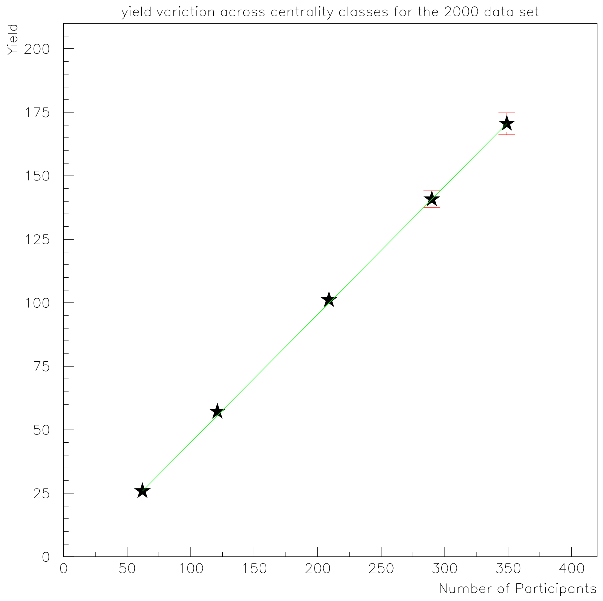

Figure 5.27: Variation in yield as a function of number of wounded nucleons for the 2000 158 GeV/c data set.

The stability tests performed on the data sets have shown nothing that can explain the systematic error between the two data sets. This leaves a few options as to what can be done in order to get a final result for the 158 GeV data. The first option is to simply place a systematic error with the statistical error on the two data sets to cover this difference. Although this leaves the data with a large error it allows both data sets to be used in any future analysis seperately. The second option is to take a weighted average of the two weighted data sets and therefore re-calculate the yield and inverse slope. This would also involve a systematic error.

As the difference between the yields and inverse slopes of the two data sets is of the order of 10% it is preferable to take a weighted average of the two data sets. This average can then be compared to results from other experiments.

5.5.1 Weighted Average

The weighted average of the two data sets is taken using the formula:

$$\mu = \frac{\sum \frac{\text{Yield}}{\sigma^2}}{\sum \frac{1}{\sigma^2}}$$

By doing this with each centrality class, results can be obtained for the weighted average of the two data sets.

These values can now be taken as the final results for inverse slopes and yields for the 158 GeV data. In the future studies maybe completed in which the systematic error between the two data sets can be explained. However until such studies can be completed by the NA57 collaboration a systematic error must be added in order to cover the individual errors of the two data sets. The final values for the inverse slopes and yields are shown in Table 5.20 and the variation of yield with number of Wounded Nucleons is shown in Figure 5.28. The value of the sytematic error used was defined in order to cover both the 1998 and 2000 data set results within it.

Table 5.20: Final Inverse Slopes and Yields for the weighted average of the two data sets..

MSD class	Centrality	Total number of events sampled	Inverse Slope	Yield
full	full	6756	$208.1 \pm 1.2_{stat} \pm 7_{sys}$	$83.2 \pm 0.7_{stat} \pm 7_{sys}$
0	42-56%	1839	$200.8 \pm 4.1_{stat} \pm 4_{sys}$	$27.2 \pm 0.8_{stat} \pm 2.5_{sys}$
1	25-42%	2131	$201.5 \pm 2.4_{stat} \pm 5_{sys}$	$60.5 \pm 0.9_{stat} \pm 5_{sys}$
2	12-25%	1427	$207.3 \pm 2.2_{stat} \pm 8_{sys}$	$105.2 \pm 1.6_{stat} \pm 6_{sys}$
3	4.5-12%	792	$211.5 \pm 2.5_{stat} \pm 6_{sys}$	$149.9 \pm 2.5_{stat} \pm 12_{sys}$
4	0-4.5%	567	$214.6 \pm 2.6_{stat} \pm 13_{sys}$	$180.9 \pm 3.2_{stat} \pm 14_{sys}$

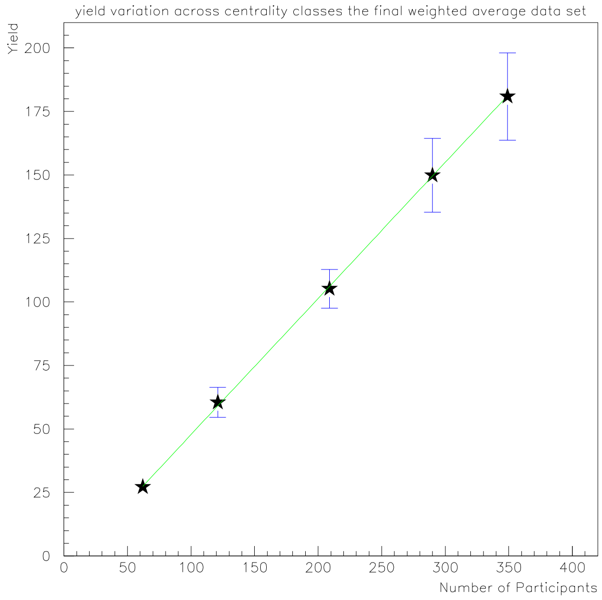

Figure 5.28: Variation in yield as a function of number of wounded nucleons for the weighted average yield of both data sets

5.6 Comparison With Other Experiments

The NA49 experiment has produced results at both energies of 40 GeV and 158 GeV for π^-, K$^-$ and $\overline{p}$, these results can be compared to the inverse slopes and yields determined in this thesis. The comparison for 40 GeV data has been done at the end of chapter 4.

Figure 4.21 shows the rapidity distribution around mid-rapidity for π^- particles. As with the 40 GeV data set the shape of this distribution supports the use of a gaussian function rather than a flat distribution for the rapidity. The results from NA49 at 158 GeV are shown in Table 5.21.

Table 5.21: NA49 yields and slopes for π^-, K^- and $\overline{p}$ for central (5%) Pb-Pb collisions at central rapidity and NA57 negative yields and slopes for central (5%) Pb-Pb collisions at 158 GeV.

Particle	Inverse Slope	Yield
π^-	$180 \pm 3 \pm 10$	$175.4 \pm 0.7 \pm 9$
K^-	$226 \pm 9 \pm 6$	$16.8 \pm 0.2 \pm 0.8$
$\overline{p}$	291 ± 315	1.66 ± 0.17
NA49 Negatives	n/a	$193.9 \pm 1.1 \pm 10$
NA57 negatives	$214.6 \pm 2.6_{stat} \pm 13_{sys}$	$180.9 \pm 3.2_{stat} \pm 14_{sys}$

As with the 1999 40 GeV data set the inverse slopes are higher than those found by NA49 for π^- particles. The final yield also sits above that found for π^- mesons, it also lies within the errors of the total yield for negatives from NA49.

5.7 R_{cp} and Cronin effect

For the 158 GeV/c higher statistics were used in an attempt to look at the effects at higher P_T. To do this the 10 times the background statistics were processed for the 2000 data set. The 2000 data set were used in preference to the 1998 data set as the work had already been done on other particles species for this data set. It was also decided that the centrality classes used to describe the data should be re-defined for the study of R_{cp} in order to make them simpler to follow and more evenly spread classes. The new definitions are shown in Table 5.22.

In Table 5.22 $< N_{\text{coll}} >$ is the average number of collisions in the corresponding centrality class and $< N_{\text{Wound}} >$ is the average number of participants, also referred

Table 5.22: Definitions of centrality classes used in study of R_{cp} for the 158 GeV 2000 data set.

Class (% $\sigma_{\mathrm{inel}}^{\mathrm{Pb-Pb}}$)	$< N_{\mathrm{Wound}} >$	$< N_{\mathrm{coll}} >$
0–5.0%	345.3 ± 1.7	779.2 ± 26.6
5.0–10.0%	293.0 ± 3.0	616.2 ± 26.3
10.0–20.0%	214.7 ± 5.8	421.7 ± 26.1
20.0–30.0%	143.0 ± 6.6	247.7 ± 21.5
30.0–40.0%	92.6 ± 6.4	140.5 ± 16.2
40.0–55.0%	49.5 ± 5.0	63.8 ± 9.8

to as the number of wounded nucleons. The definition of R_{cp}, which was given in section 4.5, is shown again below.

$$R_{CP}(p_t) = \frac{< N_{\mathrm{collP}} >}{< N_{\mathrm{collC}} >} \times \frac{\mathrm{d}^2 N_{\mathrm{AA}}^{\mathrm{C}}/\mathrm{d}p_t\mathrm{d}y}{\mathrm{d}^2 N_{\mathrm{AA}}^{\mathrm{P}}/\mathrm{d}p_t\mathrm{d}y} \tag{5.1}$$

As mentioned in section 4.5 the R_{cp} results are not obtained using weighted data as the weights are not centrality dependent. Figure 5.29 shows the ratio of average weight for the particle species K_s^0, Λ, $\overline{\Lambda}$ and negatively charged particles as a function of P_T[46].

Figure 5.30 shows the R_{cp} results for the negatively charged particles using the higher statistics data.

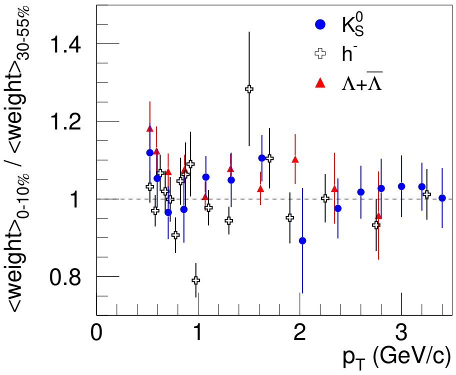

Figure 5.29: Ratio of average weights for central events to peripheral events as a function of P$_T$ for various particle species.

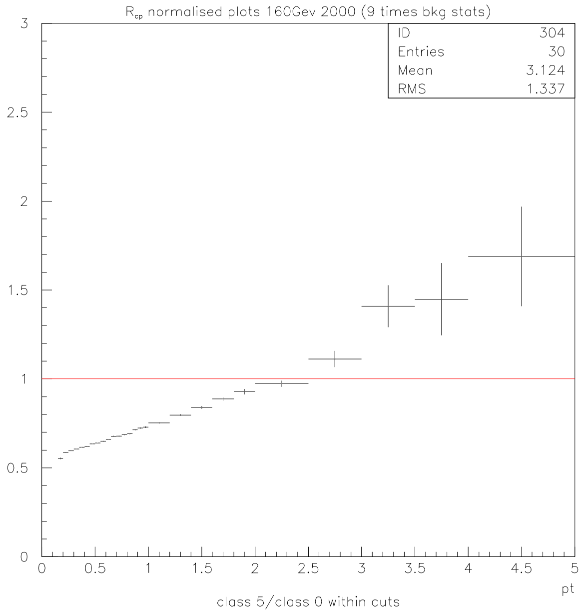

Figure 5.30: R$_{cp}$ of 10 times the background tapes statistics for the 2000 158 GeV/c data set.

The results in Figure 5.30 have been used along with results for other particle species as part of a paper written by the NA57 collaboration which presents their results on R$_{cp}$[46]. Although the negative tracks shown in Figure 5.30 do not show the Cronin effect or a high P$_T$ suppression (as described in section 1.5.6), other particle species do begin to show the effect. Figure 5.31 is taken from the NA57 R$_{CP}$ paper, mentioned previously, and shows the results for negatively charged particles, K_s^0, Λ and $\overline{\Lambda}$ particles.

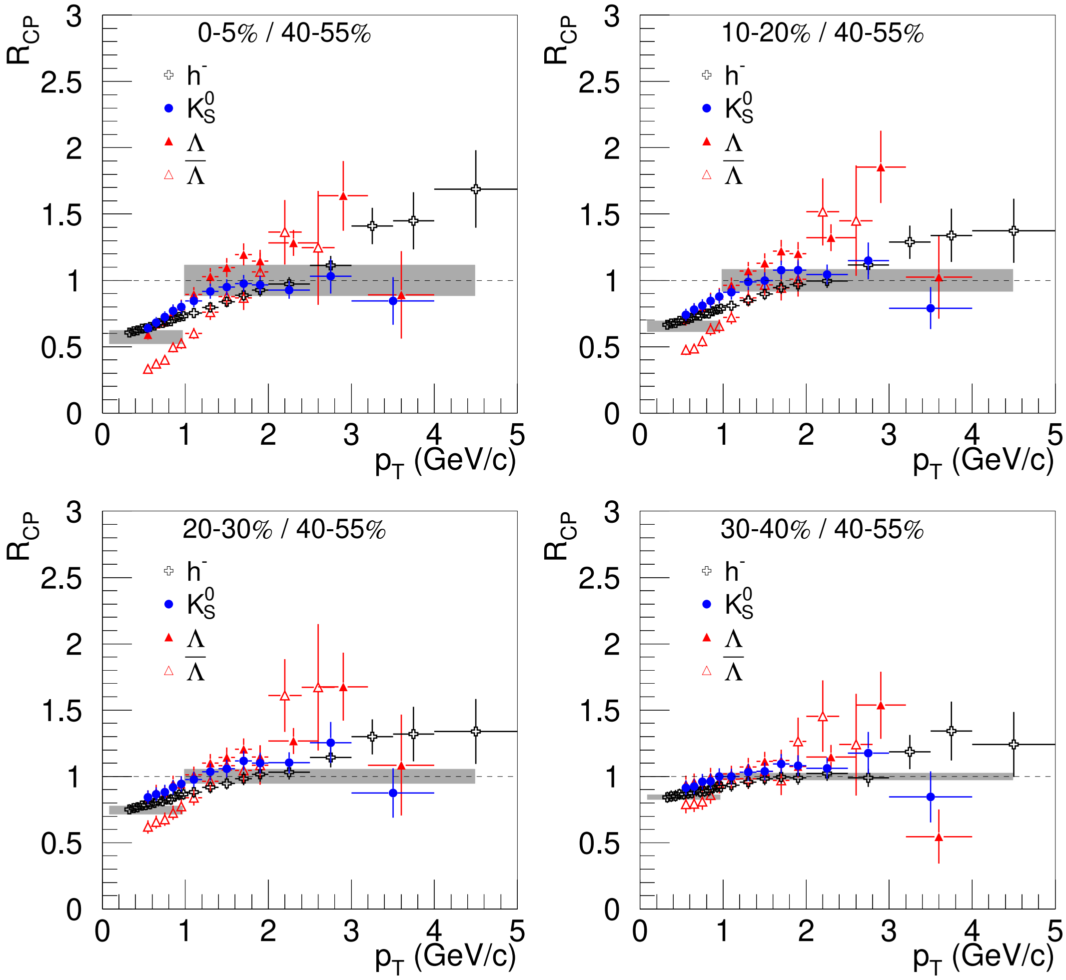

Figure 5.31: R_{cp} for negatively charged particles, K_s^0, Λ and $\overline{\Lambda}$ particles using the 2000 158 GeV/c data set.

The R_{CP} for h^- particles can be compared to π^0 results from the WA98 experiment[47]. These results are shown in Figure 5.32 and are compatible, within errors, up to P_T $\leq$ 1.5 GeV where the h^- sample is expected to be dominated by π^-. At higher P_T the two data sets do not agree as well, this is most likely due to the contamination of the h^- sample by K^- and $\overline{p}$.

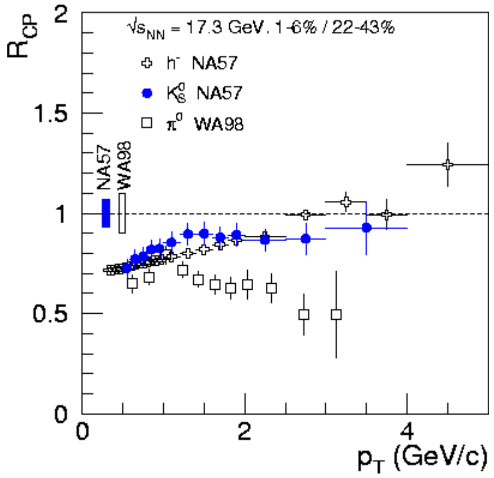

Figure 5.32: Comparison of R$_{CP}$ for h$^-$ sample with WA98 π^0 particles in the centrality ranges 1-6% / 22-43%.

Summary

The two 158 GeV data sets taken in 1998 and 2000 have been fully analysed in order to produce results for the inverse slopes and background corrected yields. As with the 40 GeV data set a weighting method has been used to correct for efficiencies and phase space coverage in order to produce these results. Cuts were defined using both Monte Carlo data and real data and it was shown that any effect produced by interactions with the end of the beam pipe are negligible. However the final results produced for the two data sets did not show good agreement within statistical errors. A safisfactory reason for this could not be found despite thorough investigations being performed on the data. It was therefore decided that a weighted average of the two data sets should be taken and a systematic error covering the range of the two data sets added. The weighted average result was then compared to results from the NA49 collaboration in order to add further support to values calculated. Further to the calculation of inverse slope and yields a study of R$_{CP}$ was performed. This was only done using the 2000 data set however higher statistics were used in order to gain a more conclusive result. Although no suppresion or evidence of the Cronin effect was found within the negative particles, other particle species did begin to show the Cronin effect at higher P_T. In order to investigate the effect in negative particles even higher statistics need to be used to look at a larger range of P_T.

Overall the results produced for negative particles require further investigation beyond the scope of this thesis in order to produce results which can be used to calculate enhancements. Analysis on strange particle yields and slopes may provide further information in order to solve the descrepency between the two data sets. However this analysis is yet to be completed by the NA57 collaboration.

Appendix A

Pixel Variance

Figure A.1 demonstrates that a track moving through the telescope can hit the pixel anywhere within its finite width, ε.

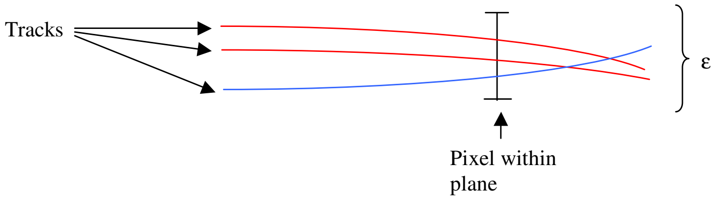

Figure A.1: Impacts of tracks on 1 pixel

The probability of finding a hit at position x on the pixel is $\rho(x)\mathrm{d}x$, assuming a uniform distribution. This allows us to define the probability density function as $\rho(x)=\frac{1}{\varepsilon}$. We can also define the average position on which tracks will hit the pixel. Intuitively this should be the middle of the pixel but it can be shown as follows.

$$\overline{x} = \int_0^\varepsilon \rho x dx = \frac{1}{\varepsilon}\int_0^\varepsilon x dx = [\frac{1}{\varepsilon}\frac{x^2}{2}]_0^\varepsilon = \frac{\varepsilon}{2}$$

Therefore, the average distribution about the mean is $\overline{(x-\overline{x})^2}$. The resolution of the pixel can then be calculated by integrating the probability density function times the average distribution about the mean over the full width of the pixel:

$$\int_0^{\varepsilon} \rho(x-\overline{x})^2 dx = \int_0^{\varepsilon} \rho(x-\frac{\varepsilon}{2})^2 dx = \frac{1}{\varepsilon}\int_0^{\varepsilon}(x-\frac{\varepsilon}{2})^2 dx$$

$$\frac{1}{\varepsilon}\int_0^{\varepsilon}(x^2-\frac{\varepsilon x}{2}+\frac{\varepsilon^2}{4})dx = \frac{1}{\varepsilon}[\frac{x^3}{3}-\frac{\varepsilon x^2}{2}-\frac{\varepsilon^2 x}{4}]_0^{\varepsilon} = \frac{1}{\varepsilon}(\frac{\varepsilon^3}{3}-\frac{\varepsilon^3}{2}+\frac{\varepsilon^3}{4}) = \frac{\varepsilon^2}{12}$$

So the resolution of the pixel is $\frac{\varepsilon}{\sqrt{12}}$. This means that the variance is $\frac{\varepsilon^2}{12}$

Appendix B

Multiple scattering error for 11-planes

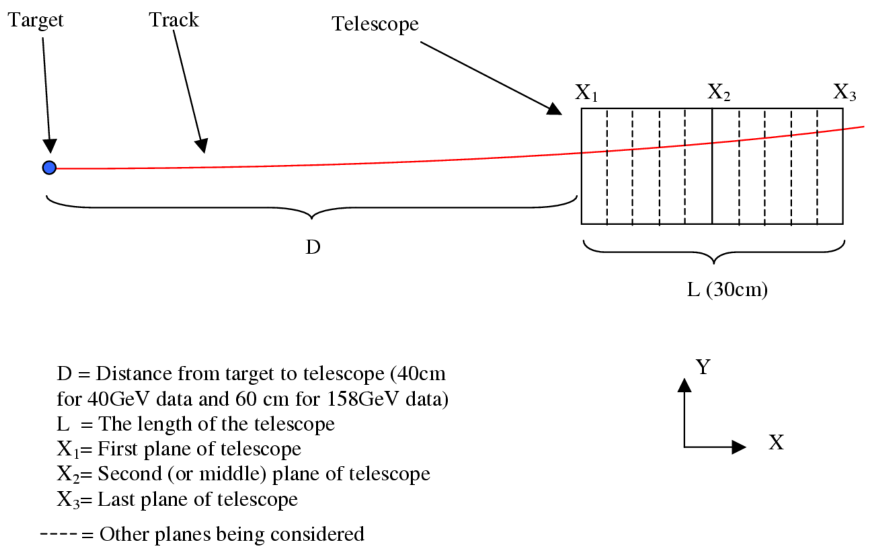

Figure B.1: Experimental set-up for calculating 11-plane error for multiple scattering

The error for multiple scattering with 11 planes is calculated in much the same way as for 3 planes. The main difference is that account must be taken of the other planes in the telescope by including the scattering angle due to them in y_1, y_2 and y_3. This set up is shown in figure B.1. To try and keep it slightly simpler the y impact positions on the first, middle and last planes can be referred to as y_1, y_6 and y_11 instead of y_1, y_2 and y_3, i.e. they will be numbered according to the plane number they represent.

$$y_1 = D\theta_T$$

$$y_6 = (D + \frac{L}{2})\theta_T + \frac{1}{2}L\theta_1 + \frac{2}{5}L\theta_2 + \frac{3}{10}L\theta_3 + \frac{1}{5}L\theta_4 + \frac{1}{10}L\theta_5$$

$$\begin{aligned} y_{11} =& (D + L)\theta_T + L\theta_1 + \frac{9}{10}L\theta_2 + \frac{4}{5}L\theta_3 + \frac{7}{10}L\theta_4 + \frac{3}{5}L\theta_5 + \frac{1}{2}L\theta_6 \\ &+ \frac{2}{5}L\theta_7 + \frac{3}{10}L\theta_8 + \frac{1}{5}L\theta_9 + \frac{1}{10}L\theta_{10} \end{aligned}$$

$$< y_1^2 >= D^2 < \theta_T^2 >$$

$$\begin{aligned} < y_7^2 >=& (D^2 + DL + \frac{L^2}{4}) < \theta_T^2 > +L^2(\frac{1}{4} < \theta_1^2 > +\frac{4}{25} < \theta_2^2 > \\ &+ \frac{9}{100} < \theta_3^2 > +\frac{1}{25} < \theta_4^2 > +\frac{1}{100} < \theta_5^2 >) \end{aligned}$$

$$\begin{aligned} < y_{11}^2 >=& (D^2 + 2DL + L^2) < \theta_T^2 > +L^2(< \theta_1^2 > +\frac{81}{100} < \theta_2^2 > +\frac{16}{25} < \theta_3^2 > +\frac{49}{100} < \theta_4^2 > \\ &+ \frac{9}{25} < \theta_5^2 > +\frac{1}{4} < \theta_6^2 > +\frac{4}{25} < \theta_7^2 > +\frac{9}{100} < \theta_8^2 > +\frac{1}{25} < \theta_9^2 > \\ &+ +\frac{1}{100} < \theta_{10}^2 > \end{aligned}$$

$$< y_1 y_6 >= (D^2 + \frac{DL}{2}) < \theta_T^2 >$$

$$< y_1 y_{11} >= (D^2 + DL) < \theta_T^2 >$$

$$\begin{aligned} < y_6 y_{11} >=& (D^2 + \frac{3DL}{2} + \frac{L^2}{2}) < \theta_T^2 > +L^2(\frac{1}{2} < \theta_1^2 > +\frac{36}{100} < \theta_2^2 > +\frac{24}{100} < \theta_3^2 > \\ &+ \frac{14}{100} < \theta_4^2 > +\frac{6}{100} < \theta_5^2 >) \end{aligned}$$

These can then be substituted into the main equation for $< C^2 >$:

$$\begin{aligned}< C^2 > =& 15^2 < y_1^2 > + 24^2 < y_6^2 > + 10^2 < y_{11}^2 > \\ & - 720 < y_1 y_6 > + 300 < y_1 y_{11} > - 480 < y_6 y_{11} >\end{aligned}$$

To get:

$$\begin{aligned}< C^2 > =& [225D^2 < \theta_T^2 >] + [576(D^2 + DL + \frac{L^2}{4}) < \theta_T^2 > + L^2(144 < \theta_1^2 > + 92.16 < \theta_2^2 > \\ & + 51.84 < \theta_3^2 > + 23.04 < \theta_4^2 > + 5.76 < \theta_5^2 >)] + [100(D^2 + 3DL + L^2) < \theta_T^2 > \\ & + L^2(100 < \theta_1^2 > + 81 < \theta_2^2 > + 64 < \theta_3^2 > + 49 < \theta_4^2 > \\ & + 36 < \theta_5^2 > + 25 < \theta_6^2 > + 16 < \theta_7^2 > + 9 < \theta_8^2 > + 4 < \theta_9^2 > \\ & + 1 < \theta_{10}^2 >)] - [720(D^2 + \frac{DL}{2}) < \theta_T^2 >] + [300(D^2 + DL) < \theta_T^2 >] \\ & - [480(D^2 + \frac{3DL}{2} + \frac{L^2}{2}) < \theta_T^2 > + L^2(240 < \theta_1^2 > \\ & + 172.8 < \theta_2^2 > + 115.2 < \theta_3^2 > + 67.2 < \theta_4^2 > + 28.8 < \theta_5^2 >)]\end{aligned}$$

Unlike the simplified version with 3 planes the θ_T^2 terms do not cancel immediately here. When added up they come to $D^2 - 4DL + 4L^2$ which cancels out when replacing D with 2L. Therefore with a little thought the target terms do cancel out. As before the θ terms can all be considered the same and so can all be grouped together.

This leaves a final value for $< C^2 >$ of:

$$< C^2 > = L^2 \frac{7780}{100} < \theta^2 >$$

Values of $< \theta^2 >$ and L^2 can then be put in to give a final answer of:

$$\begin{aligned}< C^2 > &= 900 \, \frac{7780}{100} \, \frac{0.016^2 0.017}{p^2} \\ &= \frac{0.304727}{p^2} \\ &= \frac{0.305}{p^2}\end{aligned}$$

Appendix C

Maximum Likelihood Method

In order to obtain the inverse slope, T, parameter the maximum likelihood method is used. In order to do this the transverse mass of each particle within the sample and the probability distribution function which describes m_T are needed. The probability distribution function is obtained from the function decribed in section 3.4.2, both are shown below:

$$\frac{d^2N}{dm_T dy} = m_T\, f(y) e^{-\, m_T/T}$$

$$f(m_{Ti}, T) = m_T\, A(T) e^{-\, m_T/T}$$

The above function assumes a flat rapidity distribution. To use the maximum likelihood method without a flat distribution a further term has to be introduced to describe the rapidity. This function is a simple Gaussian; however its introduction increases the number of free parameters. The overall probablity distribution function is shown below, but for the rest of this explanation a flat rapidity is assumed for simplicity.

$$f(m_{Ti}, T, y, \sigma) = m_T\, A(T, \sigma, \mu) e^{-\, m_T/T} e^{\frac{y-\mu^2}{2\sigma^2}}$$

The next step is to evaluate the constant $A(T)$ in terms of T. This is done by integrating the probability distribution function over the acceptance window, and normalising the result by setting this equal to 1, as seen shown below:

$$\int_{window} f(m_T, T)\, dm_T = 1$$

By considering individual tracks each with a different m_T it can be said that the probability of measuring m_{T1} is $f(m_{T1}, T)$, m_{T2} is $f(m_{T2}, T)$ and m_{TN} is $f(m_{TN}, T)$, so the probability of getting the results which were obtained is:

$$\mathcal{L} = f(m_{T1}, T) f(m_{T2}, T) \ldots f(m_{TN}, T) = \prod_{i=1}^{N} f(m_{Ti}, T)$$

where $\mathcal{L}$ is the *likelihood function.*

In order to correct for things such as reconstruction inefficiencies every particle is given a weight. This was discussed in more detail in section 3.4. To correct for the weight [48] the *likelihood function* becomes:

$$\mathcal{L} = f(m_{T1}, T)^{W_1} f(m_{T2}, T)^{W_2} \ldots f(m_{TN}, T)^{W_N} = \prod_{i=1}^{N} f(m_{Ti}, T)^{W_i}$$

where W_i is the weight assigned to the *ith* particle

In order to determine T the *likelihood function*, $\mathcal{L}$, needs to be maximised. This is done by considering the derivative of $\mathcal{L}$ as follows.

$$\frac{\partial L}{\partial T} = 0$$

In practice it is easier to maximise $ln\, \mathcal{L}$ rather than $\mathcal{L}$ as $\mathcal{L}$ is a product of exponentials. By doing this the product becomes a summation of logarithmic terms. The position of the maximum is the same in both cases. Using the log likelihood also has the effect of moving the weight from being a power. This is shown below.

$$ln\, \mathcal{L} = \sum_{i=1}^{N} ln\, f(m_{Ti}, T)^{W_i}$$

which becomes

$$ln\, \mathcal{L} = \sum_{i=1}^{N} W_i \, ln\, f(m_{Ti}, T)$$

and so the maximisation condition becomes:

$$\frac{\partial\, ln\, \mathcal{L}}{\partial T} = \sum_{i=1}^{N} W_i \, \frac{\partial}{\partial T} \, ln\, f(m_{Ti}, T) = 0$$

The maximum likelihood method is performed using a program called MINUIT[49], which is used to find the minimum (or maximum) value of a multi-parameter function and analyse the shape of the function about the minimum (or maximum). As stated previously the above example assumes a flat rapidity distribution. If a non-flat rapidity distribution is used then the maximisation condition involves finding the minimum of several variables and so becomes:

$$\frac{\partial\, ln\, \mathcal{L}}{\partial T} = \sum_{i=1}^{N} W_i \, \frac{\partial}{\partial T} \, ln\, f(m_{Ti}, T, y, \sigma) = 0$$

$$\frac{\partial\, ln\, \mathcal{L}}{\partial \sigma} = \sum_{i=1}^{N} W_i \, \frac{\partial}{\partial \sigma} \, ln\, f(m_{Ti}, T, y, \sigma) = 0$$

$$\frac{\partial\, ln\, \mathcal{L}}{\partial y} = \sum_{i=1}^{N} W_i \, \frac{\partial}{\partial y} \, ln\, f(m_{Ti}, T, y, \sigma) = 0$$

all assuming that the mean of the gaussian is fixed.

Bibliography

[1] D.H. Perkins, *"Introduction to High Energy Physics"*, Cambridge Unversity Press, 4th Edition (2000), Chapter 6

[2] D.H. Perkins, *"Introduction to High Energy Physics"*, Cambridge Unversity Press, 4th Edition (2000), Section 2.6

[3] F. Halzen and A. D. Martin, *"Quarks and Leptons: An Introductory Course in Modern Particle Physics"*, John Wiley & Sons (1984).

[4] D.H. Perkins, *"Introduction to High Energy Physics"*, Cambridge Unversity Press, 4th Edition (2000), Chapter 1

[5] Simon Hands 2001 *arXiv:physics/0105022 v1* SWAT/01/287

[6] S. Eidelman *et al.*, (Particle Data Group), *Phys. Lett.* B **592**, (2004), 1-1109.

[7] J Letessier and J. Rafelski, *"Hadrons and Quark-Gluon Plasma"*, Cambridge University Press, First Edition (2002).

[8] S. Hands, *Contemp. Phys.* **42**, (2001), 209-225.

[9] WA97 Proposal, *CERN/SPSLC/91-29 SPSLC/P263*, (May 1991).

[10] S. Margetis, K. Šafařík, O Villalobos Baillie, Annu. Rev. Nucl. Part. Sci, **50**, (2000), 299-342.

[11] NA57 Proposal, *CERN/SPSLC/96-40 SPSLC/P300*, (August 1996).

[12] L.McLerran and T.Toimela, Phys. Rev. D31 (1985) 545

[13] NA45/CERES Proposal, CERN/SPSC/88-25 SPSC/P237, (June 1988).

[14] B. Lenkeit *et al.*, (CERES Collaboration), *Nucl. Phys.* A 661, (1999), 23c-32c.

[15] RHIC (Relativistic Heavy Ion Collider), *www.bnl.gov/RHIC*.

[16] The LHC, *http://lhc-new-homepage.web.cern.ch/lhc-new-homepage*.

[17] The Alice Experiment, *http://aliceinfo.cern.ch*.

[18] J.W. Harris and B. Müller, *Annu. Rev. Nucl. Part. Sci.* **46**, (1996), 71-107.

[19] T. Matsui and H. Satz, *Phys. Lett.* B **178**, (1986), 416-422.

[20] NA50 Proposal, *CERN/SPSLC/91-55 SPSLC/P265*, (November 1991).

[21] M.C.Abreu *et al.*, (NA50 Collaboration), *Phys. Lett.*. B 477, (2000), 28-36

[22] David Evans PhD Thesis School of Physics, University of Birmingham 1992

[23] J. Adams *et al.* (STAR Collaboration), *Phys. Rev. Lett.* 91, (2003), 072304.

[24] J. Cronin *et al.*, Phys. Rev. D 11 (1975) 3105; D. Antreasyan *et al.*, Phys. Rev. D 19 (1979) 764.

[25] J. Adams *et al.*, (STAR Collaboration), Evidence from d+Au measurements for final-state suppression of high p_T hadrons in Au+Au collisions at RHIC, *nucl-ex/0306024*, (August 2003).

[26] Aggarwal, M. M. and others, WA98 collaboration Eur. Phys. J. C23 (2002) 225-236

[27] J. Adams *et al.*, (STAR Collaboration), Phys. Rev. Lett. 92 (2004) 052302

[28] M Gazdzicki nucl-th/9706036 v1 1997

[29] http://academia.hixie.ch/bath/accelerator/page1.html

[30] http://www.cerncourier.com/main/article/41/6/17

[31] Rory Clarke PhD Thesis School of Physics, University of Birmingham 2004

[32] R.J. Glauber and G. Matthiae, Nucl. Phys. B 21 (1970) 135; A. Bialas, M. Bleszyński and W. Czyz, Nucl. Phys. B 111 (1976) 461.

[33] F Antinori *et al.*2000 *Eur. Phys. J. C* 18, 57-63

[34] D Di Bari *et al.* 1997 *Nucl Phys A 395* 391-397

[35] Home page of the NA57 experiment http://wa97.web.cern.ch/WA97/

[36] Physics Analysis Workstation, *An Introductory Tutorial*, CERN Program Library, Long Writeup Q121, (1995).

[37] R L Gluckstern 1963 *Nuclear Instruments and Methods* 381-389

[38] WA97 Internal note

[39] GEANT, *Detector Description and Simulation Tool*, CERN Program Library, Long Writeup W5013, (1993).

[40] R. Brun et al., FFREAD Manual (1986), CERN Computer Centre

[41] F. Antinori *et al.* [NA57 Collaboration],

[42] S. Afanasiev *et al.*, (NA49 Collaboration), *Nu cl. Instr. and Meth. in Phys. Res.* A **430**, (1999), 210-244.

[43] NA49 contribution to "International workshop on the physics of the QGP", Palaiseau, France, Sep 4-7, 2001." http://na49info.cern.ch/cgi-bin/wwwd-util/NA49/NOTE?270

[44] Afanasiev, *S. V. and others*, The NA49 collaboration, "Energy dependence of pion and kaon production in central Pb + Pb collisions, *Phys. Rev. C66* 2002, 054902, nucl-ex/0205002,

[45] http://na49info.cern.ch/na49/Archives/Data/

[46] Antinori, F. et al., NA57, "Central-to-peripheral nuclear modification factors in Pb Pb collisions at s(NN)**(1/2) = 17.3-GeV", *Phys. Lett.* B **623**, (2005), 17-25.

[47] M.M. Aggarwal *et al.*, WA98 Coll., Eur. Phys. J. C 23 (2002) 225.

[48] W.T. Eadie *et al.*, *Statistical Methods in Experimental Physics*, Elsevier Science Publishers, Third Reprint, (1988).

[49] F.James, MINUIT, *Reference Manual*, CERN Program Library, Long Writeup D506, (1994).